

A STATISTICAL FRAMEWORK FOR THE ANALYSIS OF DIRECTED INTERACTIONS IN
STEREOTACTIC EEG DATA

A Thesis submitted to
the Division of Applied Mathematics
at Brown University

In Partial Fulfillment
of the Requirements for
Honors in Applied Mathematics-Biology

by
DANIEL ALBER
Supervised by
Dr. Wilson Truccolo
MAY 2022

The undersigned have examined the thesis entitled

A STATISTICAL FRAMEWORK FOR THE ANALYSIS OF DIRECTED INTERACTIONS IN
STEREOTACTIC EEG DATA

presented by Daniel Alber,

a candidate for Undergraduate Concentration Honors in Applied Mathematics-Biology,
and hereby certify that, in their opinion, it is worthy of acceptance.

Professor Wilson Truccolo

Thesis Advisor, Department of Neuroscience

Professor Matthew T. Harrison

Second Reader, Division of Applied Mathematics

DEDICATION

This thesis is dedicated to all of my supporters over the years. This includes my family, who always told me I could achieve what I set out to do. My brother, Jacob, who spent hours and hours discussing every idea known to man with me. My grandparents, who practically raised me on a diet of mathematics and science. Thank you.

To my teammates on Brown's Swim and Dive team — my closest friends, roommates, and allies throughout my time here. You've helped me for four years, and I hope we share many more together. Thank you.

To my coaches, throughout life, who've made me who I am. To my mentors in and out of medicine. And to everyone else who taught me something, made me laugh, and kept me whole.

I couldn't have done it without you all.

ACKNOWLEDGEMENTS

I would like to thank the multitude of people without whom this thesis would have been impossible.

First, Professor Wilson Truccolo, who welcomed me into his lab in the middle of the pandemic, and directed this thesis from start to finish. Thank you for everything.

Next, Dr. Ammar Shaikhouni, who introduced me to this data and mentored me during my time in Ohio. Thank you.

A special thanks to Dr. Kristen Arredondo for helping me understand the clinical components of this work, introducing me to the NCH SEEG workflow, and providing invaluable support during this thesis, including all patient descriptions, delays between seizures, and other information about the patients and dataset.

To everyone at Nationwide Children's and in the Truccolo Lab, thank you for the support throughout this project and during the past two years.

Thank you to Professor Matthew Harrison for reviewing this thesis as my second reader.

And a final thanks to the patients who participated and gave their time and data towards this project.

I was able to pursue this work during Summer 2021 thanks to a Karen T. Romer Undergraduate Teaching and Research (UTRA) award granted by Brown University. Further financial support was provided by the Ohio State University during my time in Ohio.

The research data analyzed in this thesis were collected under an IRB approved protocol at Nationwide Children's Hospital. A data sharing agreement between Nationwide Children's Hospital (Shaikhouni Lab) and Brown University (Truccolo Lab) supports the research in this thesis and related ongoing research in the Truccolo Lab.

TABLE OF CONTENTS

| | |
|--|------|
| ACKNOWLEDGEMENTS | ii |
| LIST OF FIGURES | viii |
| LIST OF TABLES | ix |
| ABSTRACT | x |
| 1 INTRODUCTION | 1 |
| 1.1 Motivation | 1 |
| 1.2 Structure | 3 |
| 2 SEEG DATA AND CLINICAL CONTEXT | 5 |
| 2.1 Pediatric Focal Epilepsy | 5 |
| 2.2 The Centromedian Thalamic Nucleus | 7 |
| 2.3 SEEG Monitoring and Recording | 8 |
| 2.3.1 Patient Descriptions | 10 |
| 2.4 Clinical Results | 16 |
| 2.5 Shortcomings of Current Methods | 20 |
| 3 MATHEMATICAL METHODS | 22 |
| 3.1 Overview | 22 |
| 3.1.1 Sample Size Issues | 22 |
| 3.1.2 Interictal Epileptiform Events | 23 |
| 3.1.3 Procedure | 23 |
| 3.2 Time-Frequency Decomposition | 24 |
| 3.2.1 Wavelet Transform | 24 |
| 3.2.2 Super-Resolution Wavelet Transform | 28 |

| | | |
|----------|---|-----------|
| 3.3 | Modeling of Neural Data | 33 |
| 3.3.1 | Stochastic Processes | 33 |
| 3.3.2 | Linear Autoregressive Models | 34 |
| 3.3.3 | Vector Autoregressive Models | 35 |
| 3.3.4 | Impulse Response and Transfer Function | 36 |
| 3.4 | Connectivity Analysis | 37 |
| 3.4.1 | Covariance Functions and Power Spectra | 37 |
| 3.4.2 | Undirected Spectral Connectivity Estimates | 39 |
| 3.5 | Directed Interactions | 40 |
| 3.5.1 | Granger Causality | 41 |
| 3.5.2 | Parametric Approach | 43 |
| 3.5.3 | G-Causality based on Spline AR(p) | 45 |
| 3.5.4 | Parametric and Non-Parametric Approaches Based on Spectral Matrix Factorization | 47 |
| 3.5.5 | Comparison of Approaches | 51 |
| 3.5.6 | Summary and Implementation Notes | 55 |
| 4 | RESULTS | 57 |
| 4.1 | Analysis of Interictal Activity | 57 |
| 4.2 | Subject Selection and Data Pre-Processing | 58 |
| 4.2.1 | Subject 1 | 58 |
| 4.2.2 | Subject 7 | 59 |
| 4.2.3 | Electrode Selection | 61 |
| 4.2.4 | Referencing Scheme | 62 |
| 4.2.5 | Other Data Considerations | 63 |
| 4.3 | Segmentation Process | 64 |
| 4.4 | Network Analysis | 66 |
| 5 | DISCUSSION | 71 |
| 5.1 | Significance | 71 |
| 5.2 | Limitations | 72 |
| 5.2.1 | Electrode Implantation | 72 |
| 5.2.2 | Depth Electrode Referencing | 72 |
| 5.2.3 | Electrode Selection | 73 |
| 5.2.4 | Segmentation | 73 |

| | | |
|-------|---------------------------------|----|
| 5.2.5 | Model Order Selection | 73 |
| 5.2.6 | Sampling Rate | 74 |
| 5.2.7 | Statistical Analysis | 74 |
| 5.3 | Continuation | 75 |

BIBLIOGRAPHY

75

LIST OF FIGURES

| | | |
|-----|---|----|
| 2.1 | Plot of CMN trajectories (yellow) and bilateral CMN (blue) on MNI average brain for 7 of the studied patients. The black rings on the electrodes correspond to individual recording contacts. | 9 |
| 2.2 | Visualized SEEG trajectories (top) and CMN electrode with MRI (bottom) for subject 1. Red indicates the location of the deepest CMN electrode contacts. | 14 |
| 2.3 | Visualized SEEG trajectories (top) and CMN electrode with MRI (bottom) for subject 7. Red indicates the location of the deepest CMN electrode contacts. | 15 |
| 2.4 | Plot of Delays to CMN Involvement Based on Neurologist Classification | 16 |
| 2.5 | Example EEG traces from seizure of subject 1, showing CMN-involvement near-synchronously with seizure onset in right cortical electrode contact (right anterior insula trajectory). Red lines mark seizure start and end. A global view of seizure evolution is shown in the top plot, while a detailed view of the first 10 seconds after onset is shown in the bottom. The bilateral CMN contacts show almost immediate oscillatory activity deviating from baseline. | 18 |
| 2.6 | Example EEG traces from seizure of subject 7, showing a seizure with no CMN involvement following onset in left medial frontal gyrus electrode contact. Red lines mark seizure start and end. A global view of seizure evolution is shown in the top plot, while a detailed view of the first 10 seconds after onset is shown in the bottom. The bilateral CMN contacts do not deviate from baseline amplitude or activity pattern during the seizure. | 19 |
| 3.1 | Morlet-based spectra of seizure recording sections (20s each) for subject 6. The signal is bipolar montage of Right Anterior Insula trajectory contact 8. The Morlet transformation results in noticeable “banding” corresponding to poor frequency resolution at higher frequencies of the spectrogram. | 26 |
| 3.2 | Example stationary AR(6) process realization (top) with detail (center) and theoretical power spectrum derived from the AR coefficients (bottom). This order-6 AR process has coefficients 3.9515, -7.8885, 9.7340, -7.7435, 3.8078, -0.9472 for time lags $\tau = 1, \dots, 6$, respectively. | 27 |

| | | |
|------|---|----|
| 3.3 | Morlet-based spectra of the AR(6) process realization in (figure 3.2). Note the insufficient frequency resolution between 150 and 175hz. | 28 |
| 3.4 | Superlet-based spectra of seizure recording sections (20s each) for subject 6. The signal is bipolar montage of Right Anterior Insula trajectory contact 8. | 29 |
| 3.5 | Adaptive superlet transform (top = order 1, bottom = order 20) of a single AR(6) process realization (figure 3.2). | 31 |
| 3.6 | Superlet spectrum of a single AR(6) process realization (figure 3.2, t = 300 to 500) for increasing orders of the adaptive superlet transform. | 32 |
| 3.7 | True connectivity of example trivariate process(left) and predicted connectivity from partial coherence (right). Note the lack of directionality, as well as the spurious connection from the indirect effect from $X_t \rightarrow Z_t$ | 41 |
| 3.8 | Possible interictal epileptiform network derived from conditional G-causality metrics. In this imaginary example, the CMN serves as a “hub” that spreads seizure activity from onset zones to cortical areas, which themselves have interacting dynamics. Note that there may be more than one seizure onset zone, and the CMN not-necessarily connect to <i>all</i> cortical regions. | 42 |
| 3.9 | Realization of AR(30) process (left; arbitrary units for amplitudes; time in seconds) and true connectivity (right; black indicates a directed connection). | 51 |
| 3.10 | Estimated of 9-node network connectivity via the parametric (top left), spline VAR(p) (top right), and non-parametric (bottom) implementations. The parametric and spline AR(p) GC grids show statistically significant G-Causality values (via F-test at $\alpha = 0.05$). Black indicates a directed connection. The non-parametric grid shows the absolute values of integrated spectral-domain causality → time-domain G-causality. (In the non-parametric case, darker color indicates stronger GC; statistical assessment is done via random permutation approaches; not shown.) | 52 |
| 3.11 | A realization from Stokes and Purdon’s 3-node AR(3) dynamical system (left; amplitudes in arbitrary units) and the corresponding true node connectivity (right; black indicates a directed connection). | 53 |
| 3.12 | Estimated network connectivity from Stokes and Purdon’s 3-node AR(3) example, via the parametric (top left), spline VAR(p) (top right), and non-parametric (bottom) implementations. The parametric and spline VAR(p) Granger networks show statistically significant G-Causality values ($\alpha = 0.05$ based on F-tests, corrected for multiple testing). The non-parametric grid shows integrated spectral-domain causality → time-domain G-causality. Statistical assessment for the non-parametric case requires bootstrapping via random permutations and is not shown. | 54 |

| | | |
|------|---|----|
| 3.13 | Estimated spectral domain G-causality from Stokes and Purdon's 3-node AR(3) example, using parametric (left) and non-parametric (right) implementations. The diagonal values in the non-parametric plot are auto-power values within each channel. | 55 |
| 4.1 | Annotation GUI showing (Subject 7) EEG data from a bipolar montage of a selected electrode contact (LTPL2-1). Data is displayed in both time (top) and frequency (bottom) domains. The vertical red line indicates current cursor position, while the green lines denote the start and end of the most recent annotation. The x-scale is time relative to EDF file start in seconds, with 10 seconds shown per window. The y-scales are in μ V and Hz for the time and frequency domain signals, respectively. The buttons allow addition, removal, and saving of annotations. The next and previous buttons shift the time window by 5 seconds forward or backward. This was chosen in anticipation of some events of interest becoming split between 10 second signal increments. | 65 |
| 4.2 | Example 5-10Hz oscillatory transient events segmented from subject 1 and 7 in time (top) and frequency (bottom) domains. The segmented event is between 0 and 1000ms (1 second), zero-padded by 250ms before and after for clarity. The spectrum is generated using an order-15 multiplicative superlet with identical parameters to the annotation process. | 66 |
| 4.3 | Outline of procedure for identification and analysis of interictal epileptiform events. Future work should expand to clinical correlation and treatment recommendation as appropriate. | 67 |
| 4.4 | Results of parametric G-causality analysis for subject 1 (left) and subject 7 (right) using AIC/BIC selected order-5 AR(p) model. The top plots show computed values of G-causality (darker means higher causality). In the bottom plots, black indicates statistically significant directed interactions (F-tests, $\alpha = 0.05$; corrected for multiple testing). Red and blue bars denote CMN electrode contacts and “segmentation electrode” contact, respectively. | 68 |
| 4.5 | Results of parametric G-causality analysis for subject 1 (left) and subject 7 (right) using VAR(p) models, order $p = 30$. The top plots show computed values of G-causality (darker means higher causality). In the bottom plots, black indicates statistically significant directed interactions (F-tests, $\alpha = 0.05$; corrected for multiple testing). Red and blue bars denote CMN electrode contacts and “segmentation electrode” contact, respectively. | 69 |
| 4.6 | Time-domain G-causality obtained via the integration on non-parametric spectral G-causality for subject 1 (left) and subject 7 (right). Red and blue bars denote CMN electrode contacts and “segmentation electrode” contact, respectively. | 70 |

LIST OF TABLES

| | | |
|-----|---|----|
| 2.1 | Patient Characteristics | 13 |
| 2.2 | Treatment Decisions | 17 |
| 4.1 | Selected Electrodes for Subject 1 | 62 |
| 4.2 | Selected Electrodes for Subject 7 | 63 |

A STATISTICAL FRAMEWORK FOR THE ANALYSIS OF DIRECTED INTERACTIONS IN
STEREOTACTIC EEG DATA

Daniel Alber

Dr. Wilson Truccolo, Thesis Supervisor

ABSTRACT

Many pediatric epilepsy cases involve focal seizures that start in specific brain areas but may spread to the entire brain. Almost one-third of pediatric focal epilepsy patients suffer from drug-resistant seizures, requiring invasive treatment such as surgery and neuromodulation. In these difficult cases, detailed monitoring, such as with Stereoelectroencephalography (SEEG), is used to inform treatment decisions.

SEEG involves surgical implantation of depth electrodes and allows simultaneous recording from a multitude of cortical and subcortical regions of interest. At Nationwide Children's Hospital, 10 drug-resistant epilepsy patients underwent SEEG monitoring between 2020 and 2021 to determine if their seizures involved the Centromedian Thalamic Nucleus (CMN), a promising neuromodulation target. Treatments were chosen based on observed seizures. However, not all patients suffered seizures during monitoring, and no objective criteria to determine CMN involvement exist.

This thesis presents a framework for rigorous analysis of brain regions involved in epilepsy networks. Interictal events, abnormal bursts of neural activity implicated in seizure dynamics, are used to estimate directed interactions between SEEG targets. Their identification, segmentation, and subsequent analysis are discussed using mathematical methods including time-frequency decomposition, autoregressive modeling, and Granger causality. Estimated time-causal networks for 5-10 Hz interictal transients in two subjects (one with CMN involvement and one without) are shown. Statistically significant directed interactions are observed and the CMN-involved subject's connectivity matrix appears denser. Although preliminary, these results demonstrate the proposed analytic framework using real-world data and provide insight for the continued investigation of interictal events and seizures.

Chapter 1

INTRODUCTION

1.1 Motivation

This project is the result of a ongoing collaboration between the Truccolo Lab at Brown University and the Shaikhouni Lab at Ohio State University and Nationwide Children’s Hospital (NCH). Dr. Ammar Shaikhouni, neurosurgeon, and other neurologists and neurosurgeons at NCH often face cases of difficult-to-treat refractory (drug-resistant) pediatric epilepsy. As part of their diagnostic workflow, some patients are subjected to stereoelectroencephalography (SEEG): surgical implantation of stereotactic depth electrodes to record intracranial EEG signals. These SEEG studies are comprehensive, multi-day recordings of epilepsy patients featuring a variety of brain states including rest, sleep, and seizures. Neurologists and epilepsy unit staff monitor the implanted patients throughout the recordings, observing and annotating epileptiform (seizure-like; abnormal) activity during and between seizures. The primary goal of these intracranial studies is to improve treatment recommendation, in combination with prior monitoring and imaging data. The primary dataset for this thesis consists of 10 such patients who underwent SEEG monitoring.

The Truccolo Lab has more than a decade of experience in the computational and statistical analysis of collective neural dynamics in neurological disorders such as epilepsy. Prior work has involved tracking and prediction of seizure activity in epilepsy patients, to improve programming of statistical algorithms for closed-loop neuro-stimulation devices. The Lab has previously worked with a variety of neural data including single-neuron recordings and electrocorticography of epilepsy patients, to derive conclusions about the nature and evolution of seizure dynamics.

SEEG data presents unique opportunities compared to other flavors of neural data. It allows for precise identification of brain structures being sampled, as implantation proceeds using a robot pre-programmed with electrode trajectories visualized using patient-specific MRI and CT scans. Over 100 depth electrode contacts record in real time at a high sampling rate of 1000 Hz, providing granular neural data involving

distinct and neurologically significant sub-cortical and cortical brain areas. The continuous multi-day SEEG recording period captures transitions between brain states and is likely to contain clinically relevant neural dynamics and possible biomarkers of epilepsy activity. For these reasons, the SEEG recordings compiled by the Shaikhouni Lab were of special interest to the Truccolo Lab.

I spent the month of July 2021 in Columbus at Nationwide Children's Hospital. I attended epilepsy conferences for diagnostic and clinical decision-making and observed SEEG electrode implantation and recording. An ongoing investigation at NCH aimed to determine Centromedian Thalamic Nucleus (CMN) involvement in refractory epilepsy patients using SEEG data. To foster the collaboration between both labs, I catalogued and organized a SEEG dataset consisting of patients with suspected CMN involvement. I also began exploratory data analysis of the SEEG data, for preparation of a clinical manuscript describing the clinical use of SEEG data at Nationwide Children's.

The neurologists at Nationwide Children's Hospital observed patient seizures recorded during SEEG monitoring to aid clinical decision making, specifically with regard to deep-brain or responsive neurostimulation targeting and surgical planning. If neurologists noted a patient suffering from seizures with onset or rapid spread through the CMN, they referred that patient to CMN-targeted intervention. Although preliminary results suggested that seizure observation may be able to guide treatment planning, there were several shortcomings to the current clinical approach. Most critically, the approach relied on subjective interpretation of SEEG data and was dependent on (relatively rare) observation of seizures to provide treatment recommendations.

To overcome the sample size issues arising from seizure scarcity, I suggest using interictal (between-seizure) epileptiform events as the primary data for epileptogenic (seizure-generation) network analysis. Interictal epileptiform events are bursts of abnormal seizure-like activity sharing characteristics of seizures. However, they themselves do not typically present with any clinical symptoms. Previous work has connected interictal epileptiform events with seizure onset zones and seizure dynamics (see section 3.1 for more details). I hypothesized that network dynamics during these epileptiform events are closely related to network dynamics during seizures. Interictal epileptiform events are much more common than seizures allowing for more statistically meaningful conclusions from their investigation.

This thesis represents the continuation of the research partnership between both labs. I aim to provide an statistically rigorous framework for the analysis of SEEG data, specifically of interictal epileptiform events, and subsequent determination of patient-specific seizure dynamics to aid treatment planning. The brain region of interest for network involvement in the presented SEEG dataset is the CMN, but in the future this framework may be extended to similar investigations of other brain regions possibly involved in epilepsy networks. The mathematical methods (described in chapter 3) used to compile this framework are the work

of others, and proper attribution and citations are given where necessary. However, to my knowledge, no complete framework for the identification, segmentation, and analysis of epileptiform event networks has been previously proposed, nor has the relationship between interictal epileptiform events and CMN-involved epilepsy been studied.

The following section contains a summary of the remaining chapters, including clinical motivation, mathematical methods, and preliminary results from application of these methods for two subjects in the Nationwide Children’s SEEG dataset. Although the results in chapter 4 are only preliminary, they demonstrate the viability of my proposed framework for real-world neural data and present several observations of ictal network structure that may inspire continued analysis.

1.2 Structure

This thesis is organized into three main chapters, concerning clinical motivation, mathematical methods, and preliminary findings. A discussion and commentary about continuing work and future possibilities follows.

Chapter 2 concerns the neuroscientific background and clinical motivation for this thesis. First, I provide a review of pediatric epilepsy focusing on drug-resistant focal epilepsy, where seizure originate from specific brain regions or seizure onset zones. Treatment options for drug-resistant epilepsy are discussed, including epilepsy surgery, deep brain stimulation, responsive neurostimulation, and vagus nerve stimulation. Next, I describe the rationale for invasive SEEG monitoring in the context of difficult-to treat epilepsy, covering Nationwide Children’s Hospital’s patient selection process and electrode implantation procedure. The 10-patient cohort is introduced and neurologist-provided descriptions given for each patient, with relevant clinical history and findings from prior non-invasive imaging and monitoring. Preliminary clinical results are summarized, along with neurologist classification of patients into CMN-involved and non-involved subgroups. I wrap up the chapter by explaining several shortcomings of the current approach, and prepare to describe a potential solution in the following chapters: the use of interictal epileptiform events in place of seizures to determine ictal (seizure) connectivity and CMN involvement.

Chapter 3 formally states my research hypothesis and introduces the mathematical methods used for my analysis of SEEG data. My proposed framework, from segmentation of interictal epileptiform events to directed network analysis, is explained in detail. Examples using simulated data are provided to illustrate each algorithm and remark on concerns or potential issues with its implementation. Segmentation of epileptiform events proceeds with time-frequency decomposition of neural time-series data. The Morlet continuous wavelet transform is used, augmented with a super-resolution (superlet) method to improve localization of high-frequency oscillatory transients. Modeling of neural data is discussed, where I derive the linear autoregressive

modeling approach (used in the remainder of the thesis) from a generic representation of nonlinear neural dynamics. To determine network relationships between segmented epileptiform events, I first introduce undirected measures of spectral connectivity, then directed connectivity methods, focusing on Geweke-Granger causality (G-Causality) as a metric for directed interactions in neural circuits. Various implementations of G-Causality are compared and contrasted in the context of known statistical issues and dataset-specific concerns.

In Chapter 4 I apply the proposed analytic framework to real neural data from two subjects in the SEEG cohort, one with neurologist-determined CMN involvement during seizures and the other without. The patients are described in greater detail. Pre-processing of SEEG data, such as electrode inclusion criteria, referencing schemes, and segmentation workflow, is explained. Preliminary findings of directed interactions are visualized and presented, along with several notable differences between the CMN-involved and non-involved subjects' network analyses.

A discussion of the framework, results, and concerns is provided in chapter 5. The hypothesis is examined in the context of CMN-involved epilepsy and other potential applications of the framework. Future directions of work, including ongoing investigations by the Truccolo Lab, and a commentary on the progression of this specific project, are remarked upon.

Chapter 2

SEEG DATA AND CLINICAL CONTEXT

2.1 Pediatric Focal Epilepsy

Epilepsy is the most commonly diagnosed neurological disorder in children, affecting half a million pediatric patients in the United States [1, 2]. Its sufferers experience chronic, recurrent seizures, which are periods of hypersynchronous neural activity with symptoms ranging from temporary lack of awareness to spontaneous loss of consciousness. Developing brains are particularly sensitive to electrical imbalances, resulting in increased seizure vulnerability for the pediatric population [3].

The preferred treatment for most epilepsy syndromes involves anti-epileptic (also known as anti-convulsant) drugs. Neurologists may trial several drugs at a time for each patient, adjusting dosages and regimes to try and achieve seizure control. However, not all epilepsy can be managed using drugs, and patients who fail to achieve seizure freedom following trials of two relevant medications are considered to have drug resistant (DRE) or refractory epilepsy [4]. Up to 25% of pediatric epilepsy patients suffer from refractory epilepsy and persistent seizures that affect quality of life, and they have less than a 5% chance of benefiting from additional drug trials [5].

Treatment options for DRE include surgical approaches and neuromodulation. Surgical approaches are invasive, irreversible, and fail to achieve seizure control in 25% of cases [6]. They may involve resection of brain areas suspected of being involved in seizure initiation, resection of entire brain hemispheres (in extreme cases), or corpus callosotomies (transection of corpus callosum fibers). Neuromodulation using DBS (deep brain stimulation — commonly "open-loop") or RNS (responsive neurostimulation — "closed-loop") is a promising avenue for treatment [7]. DBS involves insertion of electrodes into target areas to be continuously stimulated by a pre-programmed electrical device, implanted beneath the skull [8]. Stimulation parameters are tuned during clinical sessions to maximize clinical benefit and minimize side effects. Neurologists and technicians program DBS implants to stimulate at specific voltages and frequencies, adjusting parameters

until desired therapeutic effects are reached. RNS uses a similar scheme, where an adaptive neural implant is set up to detect epileptiform activity and stimulate a target brain area before a seizure begins, to terminate and prevent its spread [9]. Although DBS cannot dynamically alter stimulation in response to seizures, it is a less invasive option than RNS and easier to tune. RNS setup requires patients or their caretakers to note when a seizure occurs and upload the relevant data to the cloud for neurologists to monitor the patient remotely. Furthermore, RNS devices can target at most one or two focal regions, while DBS leads may be able to successfully treat multifocal epilepsy. The two types of devices have shown comparable efficacy in seizure prevention and improvement in quality of life [10]. Although neuromodulation is a promising option with growing use over time, results remain inconsistent, especially across different manifestations of epilepsy.

Another treatment option for refractory epilepsy is Vagus Nerve Stimulation (VNS) [11]. A device is implanted in the patient's chest cavity along with electrical leads connected to the Vagus nerve (VN). The device is programmed to stimulate the VN at regular intervals, and is well-tolerated by most patients with minimal side effects following adjustment of stimulation parameters. The therapeutic action of VNS is hypothesized to function by altering vagal afferent activities including the reticular activating system (a group of brainstem neurons that project to thalamic regions) [12]. More recently, responsive versions of VNS systems have been used to treat patients by adjusting stimulation parameters in a closed-loop setup [13]. VNS is a non-targeted treatment appears to alleviate seizure activity in drug-resistant focal seizures, but does not allow patient-specific intervention and stimulation of seizure foci or other seizure network nodes. It is often recommended when neuromodulation targets cannot be conclusively identified. Although VNS shows positive results and good tolerance in pediatric focal epilepsy patients, it is less precise than DBS and RNS. It should largely be superseded by the latter two methods if patient-specific neuromodulation targets can be identified.

Epilepsy syndromes, or related diagnoses of epilepsy based on seizure pattern, provocation, genetics, or other factors, are classified into three categories by the International League Against Epilepsy: primary generalized epilepsies, focal epilepsies, and epileptic spasms [14]. Primary generalized seizure originate bilaterally from both brain hemispheres. Focal seizures originate from brain regions in a single hemisphere, but may generalize and spread throughout the whole brain as they evolve (secondary generalization). Epileptic spasms are poorly understood groupings of seizure activity with mostly motor-related symptoms.

Focal epilepsy is the most commonly observed epilepsy subtype [15]. Its treatment is complicated by varied seizure morphology. Focal epilepsies regularly present with more than one seizure onset zone (SOZ), featuring multifocal seizures that simultaneously evolve from two or more SOZs [14, 16]. Furthermore, seizures may originate in eloquent (functionally critical) brain areas such as language and motor centers. SOZs may also change over time in the same patient. As a result, identifying and treating one or more seizure onset

zones may not be enough to adequately manage focal epilepsy.

Approaching epilepsy as a network disorder, one that involves seizure (ictal) networks consisting of distinct 'nodes' of seizure onset and propagation may improve understanding of seizure dynamics and lead to more effective treatment planning [17]. Although seizures that originate from a specific focal brain area or SOZ may begin with relatively minor symptoms, their possible spread (generalization) is of great concern as it often leads to loss of consciousness. A particular area of interest is the identification of brain structures that participate in seizure generalization. By targeting such structures, treatment plans may be able to prevent loss of consciousness by arresting a seizure before it generalizes [18, 19].

Neuromodulation is a promising treatment option that offers untapped potential for precise disruption of ictal networks, leading to measurable improvement in patient quality of life with reversible, less invasive intervention than surgery. The most significant challenge in realizing that potential is posed by the difficulty of patient selection and identification of stimulation targets. Monitoring of neural activity in both cortical and sub-cortical areas is necessary to trial candidate brain regions for DBS or RNS. In-depth investigation of patient-specific seizure semiology and neural dynamics using intracranial monitoring can help neurologists devise an optimal treatment plan that leads to the greatest chance for seizure-freedom and desired improvement in quality of life.

2.2 The Centromedian Thalamic Nucleus

Currently, one of the most promising regions for prevention of seizure spread by neuromodulation is the Centromedian Nucleus of the Thalamus (CMN). The CMN is a sub-cortical structure implicated in regulating attention and arousal states [20]. It projects diffusely to neo-cortical areas while receiving reciprocal inputs from the same areas. It is also connected to the basal ganglia. Thus, the CMN is well-positioned to route electrical activity between deep brain structures and the bilateral cortex.

Theories of epilepsy origin from as early as the 19th century have implicated hierarchically organized brain structures in seizure generation [21], after John Hughlings Jackson's seminal work lay the foundation for studies of consciousness and interaction between levels of brain organization. Advances in monitoring and imaging including various EEG methods as well as MRI and PET scans allowed neuroscientists and physicians to look inside patient's brains to observe differences between normal and abnormal neural dynamics [22].

These methods have been successful to some degree in the identification and study of individual brain structures and their roles in consciousness. As previously mentioned, focal seizures that generalize are much more likely to cause loss of consciousness — the most disruptive epilepsy symptom. For successful treatment of advanced focal epilepsy, it is important to understand the role of various brain regions, such as the CMN,

in seizure spread and generalization. Leading theories propose that consciousness originates from integration of higher brain functions by sub-cortical structures including the bilateral thalami [21]. Loss of consciousness may then propagate from deep brain structures, such as the CMN, to higher-level cortical areas.

Early experiments discovered the sensitivity of basal (deep brain) structures to disruption [23]. For example, physical or electrical stimulation of the brain stem causes near-immediate loss of consciousness. Direct study of the CMN has provided evidence for its significant role in seizure genesis and propagation. It has been shown that patients with certain epilepsy sub-types have a higher likelihood of CMN involvement in seizures: for example, patients with drug-resistant medial temporal epilepsy have increased connectivity and involvement of the CMN in generalized seizures[24], and the CMN has been observed to participate in ictal networks of Lennox-Gastaut patients [25, 26]. Furthermore, some studies have observed CMN participation in the generation of epileptiform activity including spikes and spike-wave discharges [27], and another study concluded that increased CMN-cortex connectivity is likely to intensify epileptogenesis [28]. Altered thalamic activity may also serve as a biomarker for generalization of initially focal seizures [29].

The CMN has been clinically investigated as a potent surgical and neuromodulation target. Surgery on deep brain structures is dangerous and carries a high likelihood of severe side effects, so DBS and RNS appear to be the most promising treatment options for CMN-involved seizures. Most notably, the Velasco group at the General Hospital of Mexico has been investigating DBS treatment of the CMN for over 30 years [30], studying more than 50 patients. They initially proposed the region as a candidate for DBS due to relative ease of CMN electrode implantation and the high connectivity between the CMN and bilateral cortex [23]. Stimulation using high frequency (60hz) DBS has successfully decreased or completely alleviated seizures. High frequency stimulation was discovered to decrease blood flow and increase GABA concentration in the targeted region, suggesting the mechanism of action for DBS-related seizure prevention may be GABA-related inhibition of neural hyperactivity [23]. RNS studies have also shown potential for closed-loop treatment of CMN-involved seizures, and RNS devices are capable of reliably detecting epileptiform events in CMN leads [31]. Both DBS and RNS of the CMN appears to be well-tolerated by patients and may lead to substantial seizure reduction, improved quality of life, and reduced need for future surgery [32, 33].

2.3 SEEG Monitoring and Recording

Although neuromodulation of the CMN is a promising option for treating focal seizures that generalize, a rigorous method for patient selection has not been established. Thorough monitoring and analysis is required to identify patients for more detailed investigation of CMN-seizure dynamics.

A variety of monitoring techniques and imaging studies are used to better understand a patient's seizures

and devise treatment plans. Monitoring methods range from surface electrode patches to surgically implanted electrodes, each with benefits and drawbacks: the former is quick and non-invasive, with little chance of complications, while the latter offers a precise view of electrical activity across a range of precisely-localized brain regions and structures, albeit much more invasively [34]. EEG recordings are supplemented with diagnostic imaging: MRI sequences reveal structural changes and PET scans reveal metabolic changes in patient's brains, which can be correlated to EEG data and clinical presentation of epilepsy [22].

At the Nationwide Children's Hospital, a comprehensive pediatric epilepsy center, neurologists and neurosurgeons employ a combination of non-invasive and invasive monitoring techniques to best inform the treatment of difficult epilepsy cases. Routine neurological examination is followed by MRI and PET studies as well as scalp EEG recordings using patch electrodes. Social determinants of health are also considered. At epilepsy management conferences, patients with focal findings and seizure semiology suggestive of possible cortico-thalamic dynamics receive the clinical recommendation to undergo further monitoring via invasive Stereoelectroencephalography (SEEG). Other cohorts besides the CMN candidates may undergo SEEG as well, but are not discussed in this thesis.

Motivation to proceed with SEEG monitoring is directly related to the difficulty of treating drug-resistant seizures, and the neurologist-identified potential of CMN involvement following surface EEG results. The high complication rate of treating severe refractory epilepsy provides the rationale for invasive monitoring approaches. For example, surgical failure is associated with more complex epilepsy cases in which multiple epileptogenic zones participate in seizure generation [35]. Additionally, patients with thalamic involvement in epilepsy are less likely to gain seizure freedom from surgery [28]. As treatment via surgery and neuromodulation is much more invasive than trialling different epilepsy drugs, patients with drug-resistant seizures require greater evidence for final treatment decisions. For the monitored CMN involvement candidates, inclusion of CMN electrodes in the SEEG protocol allowed for observation of seizure propagation through the CMN (or lack thereof) and confirmation of electrode trajectory in the case of permanent DBS or RNS lead placement.

Patients undergoing SEEG monitoring are implanted with numerous depth electrodes targeting both

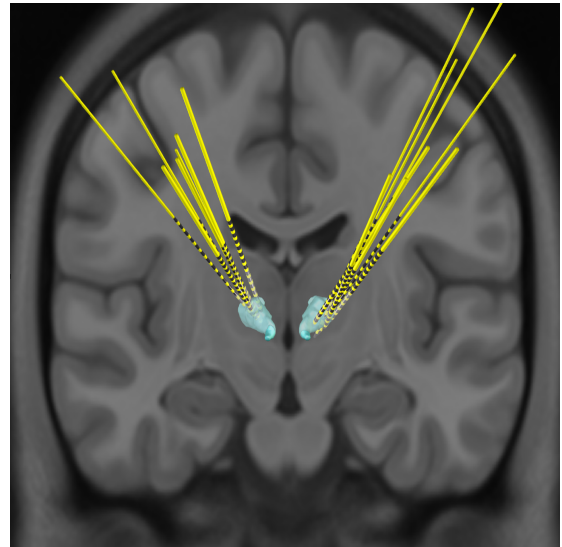


Figure 2.1: Plot of CMN trajectories (yellow) and bilateral CMN (blue) on MNI average brain for 7 of the studied patients. The black rings on the electrodes correspond to individual recording contacts.

cortical and sub-cortical brain regions. The ROSA® surgical robot platform is used for trajectory planning and frameless stereotactic electrode implantation. Standard DIXI intracranial multi-contact depth electrodes with diameter of 0.8mm, contact length of 2mm, and inter-contact distance of 3.5mm are used. Patients are implanted under general anaesthesia and postoperative imaging is used to confirm approximate electrode placement and ensure no intracranial hemorrhage or other post-operative complications. Patients are transferred to an Epilepsy Monitoring Unit or ICU, depending on case-specific considerations (e.g. age, patient disposition, comorbid conditions), for evaluation and observation throughout monitoring, lasting a period of days or weeks. Any prescribed anti-seizure medications are withdrawn to precipitate seizure occurrence.

Ten pediatric focal epilepsy patients with intractable epilepsy were selected for SEEG monitoring at Nationwide Children's Hospital due to possible CMN involved seizures. As stated earlier, the corresponding research data was collected under a research protocol approved by the Institutional Review Board of Nationwide Children's Hospital. A data-use agreement between Nationwide Children's Hospital and Brown University supports the research in this thesis and related ongoing projects in the Truccolo Lab. The patients underwent depth electrode implantation and SEEG monitoring during 2020 and 2021 as part of evaluation for potential neuromodulation or epilepsy surgery. Thalamic electrodes were included in the monitoring protocol based upon underlying seizure features and prior monitoring results suggesting the presence of a thalamic ictal network. Both CMN (Fig. 2.1) and Anterior Thalamic Nucleus (ANT) targets were included to direct potential neuromodulation targets. Hippocampal electrodes were included in three patients with suspected limbic networks. The CMN was monitored to study its relationship to sampled targets in the lateral frontal neo-cortex, frontal operculum, cingulate, insula, and hippocampi, during ictal and interictal periods. Examples of SEEG electrode locations for two patients are shown in Figure 2.2 and Figure 2.3. Descriptions of each patient, including prior monitoring results, are included below, provided by Dr. Kristen H. Arredondo of Nationwide Children's Hospital.

2.3.1 Patient Descriptions

Subject 1

Subject is a 19 year-old male with ADHD and intractable epilepsy of unknown etiology. His seizures began when he were 14 years old. They manifest as focal seizures with unresponsiveness, gaze deviation and head turn to the left, right facial clonic activity, figure-of-4 posturing with left arm extension, and bilateral tonic-clonic (BTC) activity. Surface EEG monitoring demonstrated bilateral frontal seizure onset, and several seizures had early left frontotemporal evolution with bilateral spread. Initial MRI showed cytotoxic changes

in the splenium of the corpus callosum attributed to seizure activity, and other findings were non-lesional. Positron emission tomography (PET) showed mild symmetric hypometabolism of bilateral frontal lobes, lateral temporal lobes, and hippocampi.

Subject 2

Subject 2 is a 20 year-old male with intractable epilepsy of unknown etiology. His seizures began at age 12 and attempted treatments have included multiple anti-seizure medications, VNS, and complete corpus callosotomy. The primary observed seizure type is generalized tonic clonic (GTC) seizures, which were alleviated entirely for several years following corpus callosotomy. After callosotomy, he developed focal motor seizures characterized by right facial twitching, by right hemibody clonic, and then bilateral tonic-clonic activity. He also suffers from myoclonic seizures. Surface EEG monitoring during habitual focal motor seizures demonstrated independent left and right frontal seizure onset with rapid bilateral spread. Initial MRI was non-lesional. Post-callosotomy MRI showed right medial frontal encephalomalacia at the prior craniotomy site. PET showed subtle left frontal hypometabolism.

Subject 3

Subject 3 is an 18 year-old right-handed male with intractable epilepsy of unknown etiology. He began having seizures at the age of 12. He had rare convulsive seizures exclusively out of sleep for several years and then began having seizures from wakefulness with associated versive head and gaze deviation to one side followed by bilateral tonic-clonic activity. Seizure frequency was once every few months at the time of SEEG monitoring. MRI revealed a nonspecific T2 hyperintensity in the right frontal subcortical white matter favored to represent a dilated perivascular space. PET was non-focal.

Subject 4

Subject 4 is a 14 year-old male with ADHD and intractable epilepsy of unknown etiology. His seizures began at age 9 and he suffers from several types of seizures, including: focal non-motor seizures characterized by staring, unresponsiveness, and manual automatisms, focal motor seizures with versive head and gaze deviation to either the right or left side followed by BTC activity, and bilateral myoclonic seizures. Surface EEG monitoring captured seizures of either diffuse bilateral onset with right hemispheric predominant evolution or independent left fronto-temporal onset with left temporal evolution prior to bilateral spread. Initial MRI of the brain was non-lesional aside from T2 hyperintensity in the splenium of the corpus callosum attributed to seizure activity. PET was notable for abnormal uptake in the splenium of the corpus callosum and nonspecific symmetric hypometabolism in bilateral thalamus and the anterior and mesial temporal structures.

Subject 5

Subject 5 is a 10 year-old male suffering from hypoxic ischemic encephalopathy with resultant spastic diplegia, intractable epilepsy, electrographic status epilepticus of sleep (ESES), and moderate intellectual

disability with developmental regression. His seizure semiology was primarily focal motor with right facial clonic activity, rapid blinking, and evolution to BTC with post-ictal hemiparesis. Surface EEG monitoring demonstrated nearly continuous interictal spike wave activity affecting the left hemisphere greater than the right. Onset of habitual seizures was most notable in the left frontocentral region and midline. MRI showed moderate bilateral thalamic atrophy which was more prominent on the left side, bilateral hippocampal atrophy, and gliosis of the bilateral caudate, putamen, and subcortical perirolandic white matter. PET showed abnormal hypometabolism of bilateral thalamus and caudate nuclei.

Subject 6

Subject 6 is a 17-year-old male with intractable epilepsy of unknown etiology. His seizures began at age 7 and attempted treatments include medications, dietary therapy, VNS, and complete corpus callosotomy. He experiences focal sensorimotor seizures characterized by subtle loss of tone, nonversive head turn to the left side, grabbing his eyes, and subtle upper extremity myoclonus. Seizures may progress to bilateral tonic-clonic activity. Seizure patterns did not change following corpus callosotomy. Surface EEG monitoring pre-callosotomy showed generalized seizure correlate activity and post-callosotomy showed independent right and left parasagittal seizure onset. Initial MRI was non-lesional and PET showed diffuse bilateral hypometabolism.

Subject 7

Subject 7 is a 7 year-old left-handed female with a pathogenic KCNT1 mutation and focal epilepsy best classified as autosomal dominant sleep-related hypermotor epilepsy. She has comorbid ADHD, anxiety, and cognitive impairment. Seizures began at 15 months of age, the first of which was a prolonged tonic seizure. Seizures occur most commonly out of sleep and are characterized by bilateral jerky arm movements, distal stereotypies, and oromotor automatisms with impaired awareness. Clusters of hypermotor seizures may be followed by bilateral tonic-clonic seizures. She suffers from multiple daily seizures. Her initial MRI was interpreted as normal, and a follow up MRI showed subtle left hemispheric volume loss. PET showed slight hypometabolism in the left hemisphere, best appreciated in the left temporal lobe.

Subject 8

Subject 8 is an 8 year-old right-handed male with a pathogenic DLG4 mutation and combined focal and generalized epilepsy. He has a developmental epileptic encephalopathy with continuous spike-and-wave activity during sleep, severe intellectual disability, and autism. Clinical seizures were first observed at 4 years of age. Most seizures occur out of sleep and are characterized by right facial hemiclonic movements and clonic neck flexion with progression to bilateral tonic-clonic activity. He also has staring spells with activity arrest and decreased responsiveness of an uncertain nature. Seizures were intractable to medical and dietary therapy, and prior treatment included a VNS placed at age 6. The VNS led to mild decrease in seizure duration with

minimal effect on seizure frequency. MRI of the brain showed subtle FLAIR hyperintensity in the bilateral periventricular white matter of the posterior cerebral hemispheres, without any cortical abnormality. PET scan showed mildly asymmetric hypometabolism in the right frontoparietal region.

Subject 9

Subject 9 is a 13 year-old left-handed female with mosaic Trisomy 21, bilateral hearing loss, sleep apnea, and intractable epilepsy of unknown etiology. She began having seizures at the age of 11. Her family described brief nocturnal seizures referred to as “scared episodes,” marked by sudden arousal from sleep, subtle body stiffening, fearful expression, reaching movements using both arms, and forced head turn to the right side. These occurred in clusters several times per week at the time of SEEG. She had a history of convulsive seizures at the time of initial epilepsy diagnosis. MRI revealed left mesial temporal sclerosis. PET showed hypometabolism of bilateral frontal lobes which was more apparent in the left parasagittal region.

Subject 10

Subject 10 is a 21 year-old right-handed female with intractable epilepsy of unknown etiology and intellectual disability. She began having seizures at age 5, characterized by brief behavioral arrest with eye roll likely consistent with absence seizures. She no longer experiences seizures of this type. She later developed focal tonic seizures characterized by change in facial expression, choking vocalization, bilateral arm stiffening, and facial pulling to either the right or left side, that may progress to bilateral tonic-clonic activity. MRI was non-lesional. PET showed mild symmetric hypometabolism in the bilateral paracentral regions.

Table 2.1: Patient Characteristics

| Patient | Age | Suspected Etiology | MRI Findings | PET Hypometabolism | Surface EEG Ictal |
|---------|-----|--------------------|--|----------------------------------|---------------------------|
| 1 | 19 | Unknown | Nonlesional | Bilateral frontotemporal | Bilateral frontal |
| 2 | 20 | Unknown | R medial frontal encephalomalacia | L Frontal | Bilateral frontal |
| 3 | 18 | Unknown | R medial frontal T2 hyperintensity | Nonfocal | Bilateral |
| 4 | 14 | Unknown | Nonlesional | Bilateral temporal, thalamic | L temporal and R frontal |
| 5 | 10 | Unknown | Bilateral thalamic and hippocampal atrophy | Bilateral caudate, thalamic | Midline |
| 6 | 17 | Unknown | Nonlesional | Diffuse | Bilateral parasagittal |
| 7 | 7 | Channel Mutation | Nonlesional | L hemispheric | L frontotemporal |
| 8 | 8 | Channel Mutation | Nonlesional | R posterior quadrant | R frontal |
| 9 | 13 | Unknown | L MTS, R Frontal Hyperintensity | L frontal | Bifrontal and generalized |
| 10 | 21 | Unknown | Nonlesional | Bilateral paracentral, L frontal | Bilateral frontal |

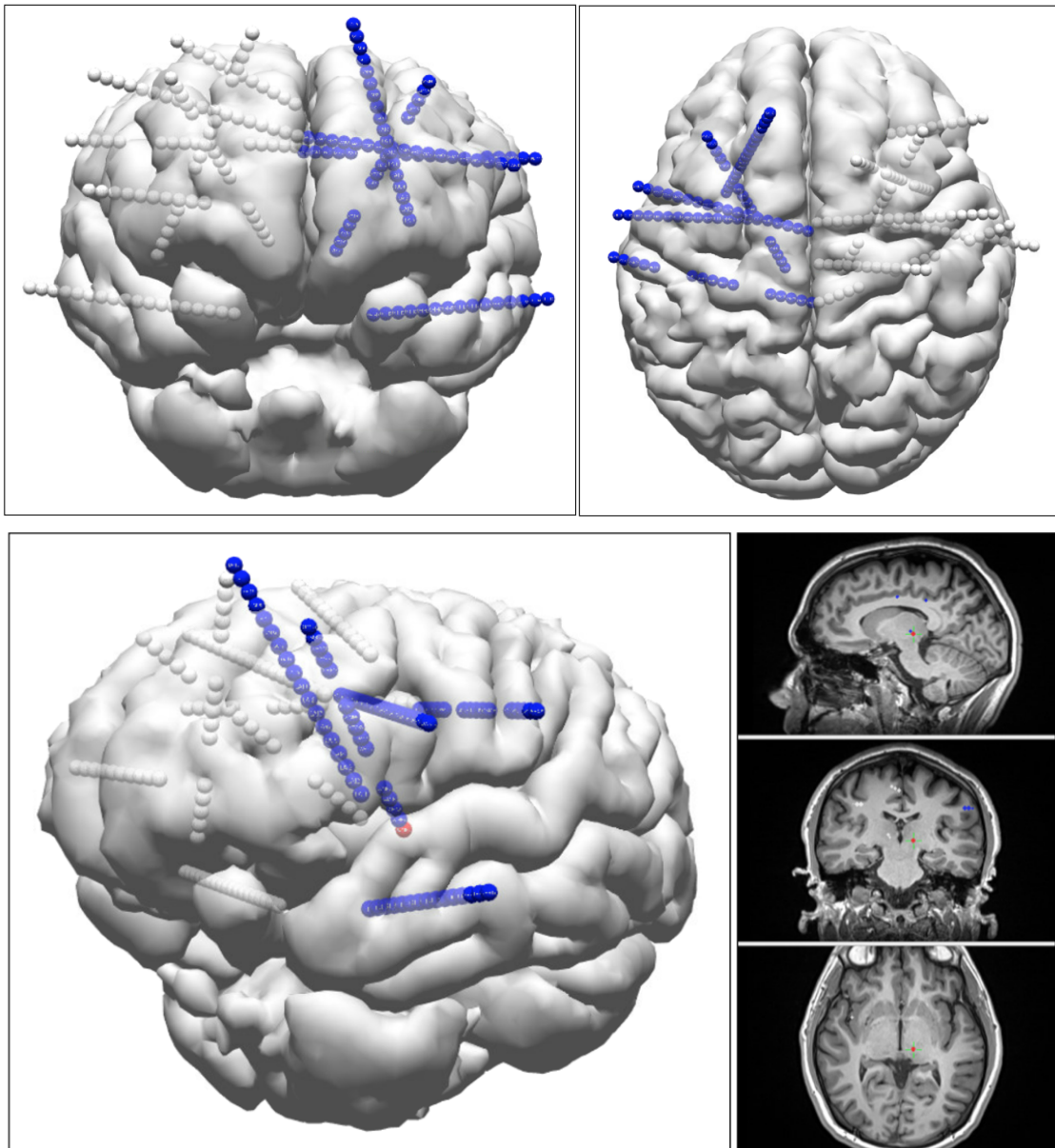


Figure 2.2: Visualized SEEG trajectories (top) and CMN electrode with MRI (bottom) for subject 1. Red indicates the location of the deepest CMN electrode contacts.

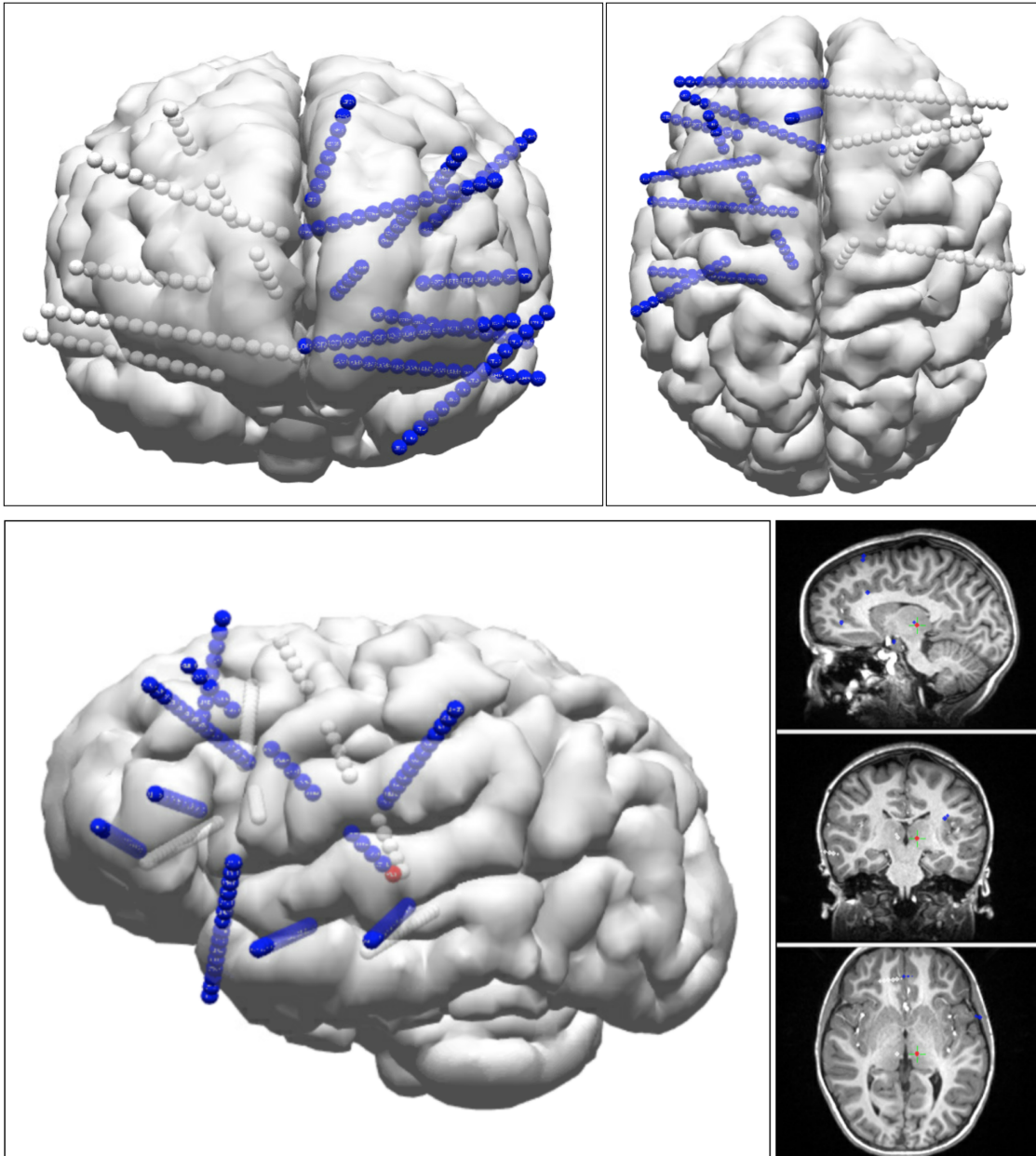
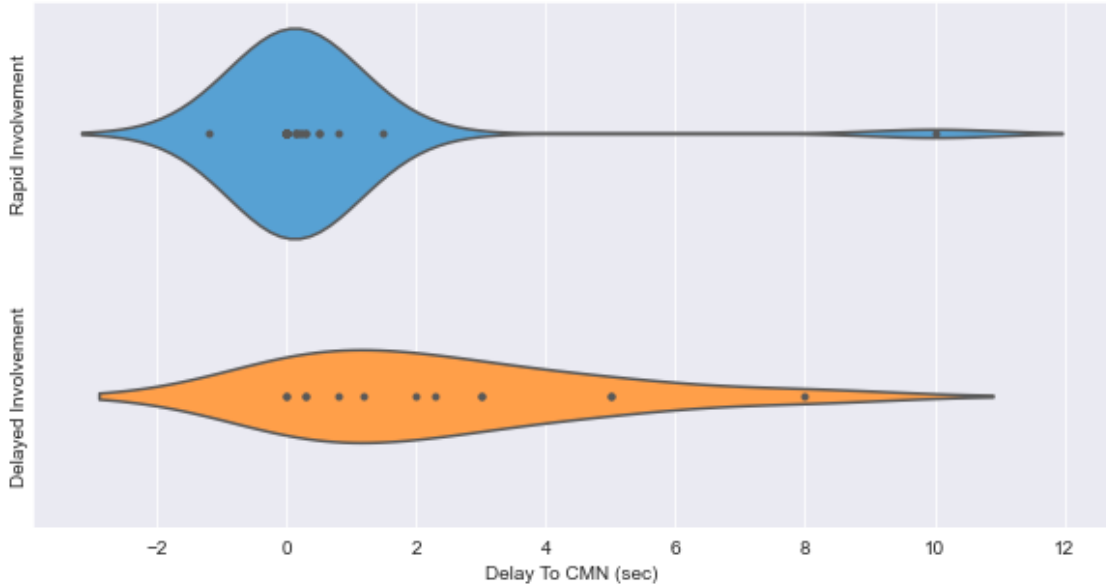


Figure 2.3: Visualized SEEG trajectories (top) and CMN electrode with MRI (bottom) for subject 7. Red indicates the location of the deepest CMN electrode contacts.

2.4 Clinical Results

The CMN-candidate patients were monitored for a duration of at least one week following electrode implantation. Neurologists and epilepsy unit staff observed patient behavior and physical symptoms through video and audio streams and recordings. The primary aim of the SEEG study was to analyze any seizures that occurred during monitoring. However, clinical staff also recorded and annotated various interictal and epileptiform activity that appeared between seizures in the SEEG traces, including sleep spindles, spike wave complexes, and other EEG abnormalities. I address different kinds of interictal epileptiform activity in the following chapters. Some patients underwent electrical stimulation to induce seizures and elucidate basic connectivity between pairs of depth electrode contacts.

Figure 2.4: Plot of Delays to CMN Involvement Based on Neurologist Classification



All but one patient experienced at least one seizure (habitual or stimulated) during the monitoring protocol. The other nine patients were sorted into two clinical groups based on their observed seizure activity, by categorizing the onset of abnormal ictal EEG signal in one or both CMNs: rapid CMN involvement and delayed/rare CMN involvement. Figures 2.5 and 2.6 show examples of related SEEG recorded seizure activity. 6 patients with rapid CMN involvement (either bilateral or unilateral) experienced seizures that arose synchronously in the CMN and onset zones. One patient experienced seizures with rare and delayed involvement of the CMN. Another patient experienced seizures with no CMN involvement. The last patient's seizures appeared inconsistent between rapid and delayed involvement of the CMN. Table 2.2 shows each patient's categorization and treatment choice.

The six patients in the rapid/synchronous group were deemed promising candidates for neuromodulation of the CMN. Three patients underwent DBS of the CMN, two patients underwent RNS (both with CMN targets, one with an additional neocortex target), and the last patient was considered a candidate for both DBS and corpus callosotomy (due to unilateral CMN involvement prior to generalization) and ultimately chose corpus callosotomy.

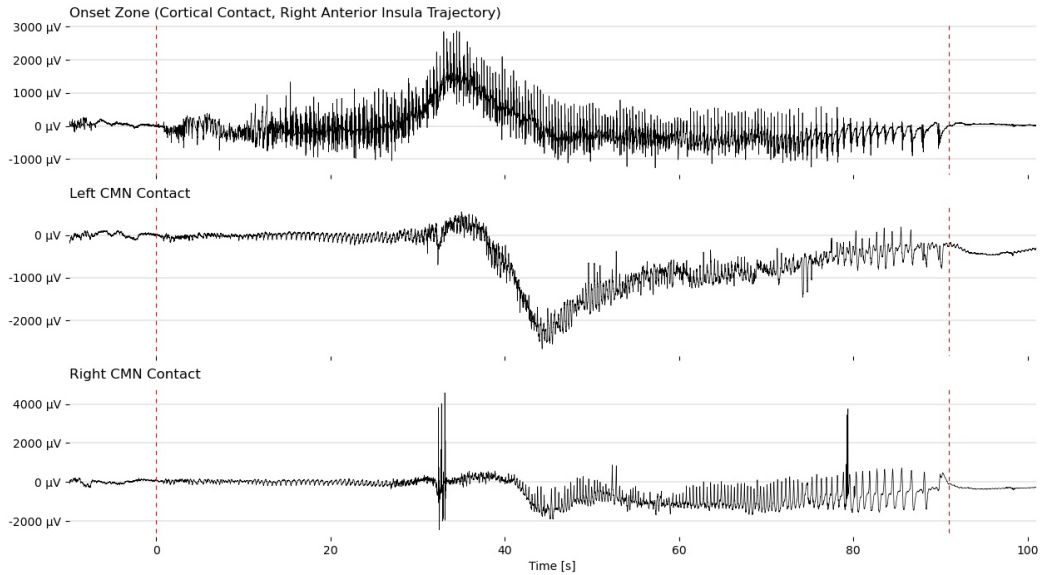
The patient with rare and delayed CMN involvement was implanted with a vagus nerve stimulator (VNS), with the possibility of re-examination for DBS of the CMN depending on their VNS treatment outcome. Patient number 10 was also offered a vagus nerve stimulator with the potential for DBS of the CMN down the line, but as of the time of writing had not yet been implanted with a device. The patient without CMN involvement was treated using DBS to target the anterior thalamic nucleus, which was observed to participate in seizures during SEEG monitoring.

Figure 2.4 compares the delay in seizure onset between the rapid/synchronous and delayed CMN involvement groups. Since SEEG monitoring was performed recently, long-term outcomes data for each subject's treatment chosen as a result of the monitoring protocol is not yet available.

Table 2.2: Treatment Decisions

| Subject | CMN Ictal Classification | Treatment Decision |
|---------|----------------------------|-------------------------------------|
| 1 | Rapid involvement | RNS-CMN (DBS denied by insurance) |
| 2 | Rapid involvement | DBS-CMN |
| 3 | No seizures observed | None |
| 4 | No involvement | DBS-Anterior thalamus |
| 5 | Rapid involvement | DBS-CMN |
| 6 | Right CMN involvement | RNS-CMN and right lateral neocortex |
| 7 | Rare involvement | VNS |
| 8 | Left CMN involvement | DBS-CMN |
| 9 | Rapid involvement | Corpus callosotomy |
| 10 | Unclear (rapid or delayed) | VNS (offered) |

Global View of Subject 1 Seizure: CMN Involved with Onset in Right Cortex



First 10 Seconds (detail) of Subject 1 Seizure

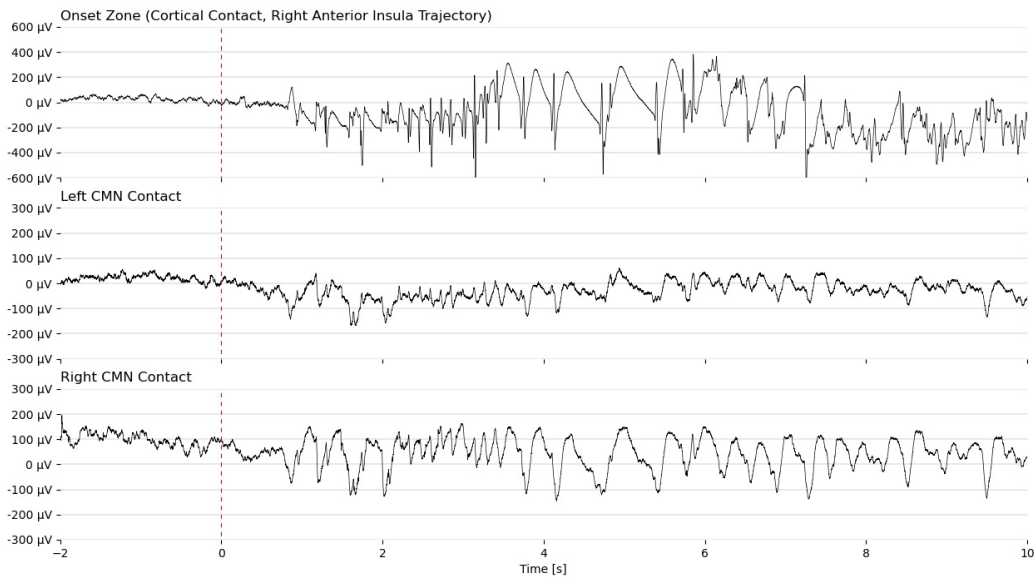
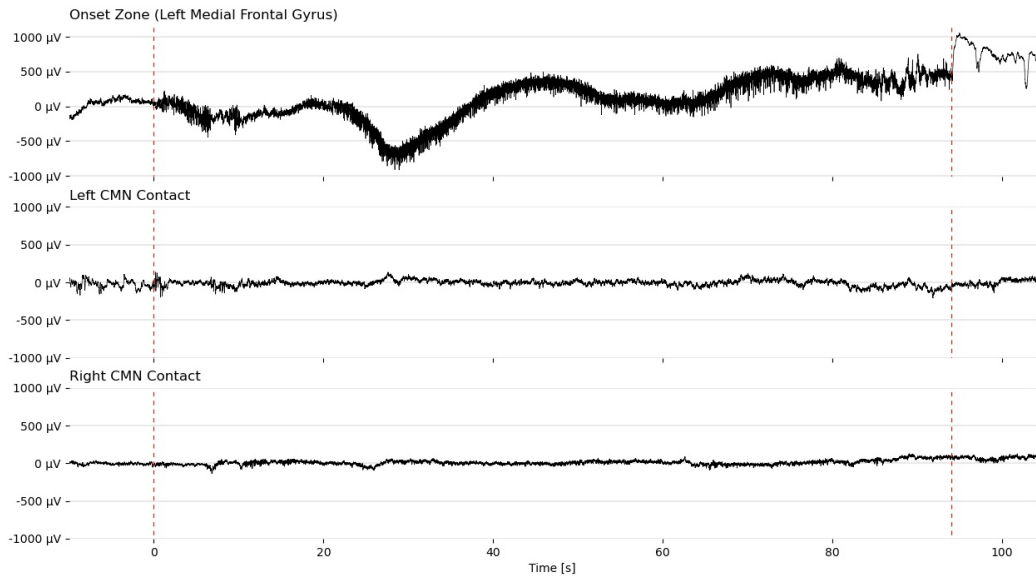


Figure 2.5: Example EEG traces from seizure of subject 1, showing CMN-involvement near-synchronously with seizure onset in right cortical electrode contact (right anterior insula trajectory). Red lines mark seizure start and end. A global view of seizure evolution is shown in the top plot, while a detailed view of the first 10 seconds after onset is shown in the bottom. The bilateral CMN contacts show almost immediate oscillatory activity deviating from baseline.

Global View of Subject 7 Seizure: CMN Not Involved with Onset in Left Medial Frontal Gyrus



First 10 Seconds (detail) of Subject 7 Seizure

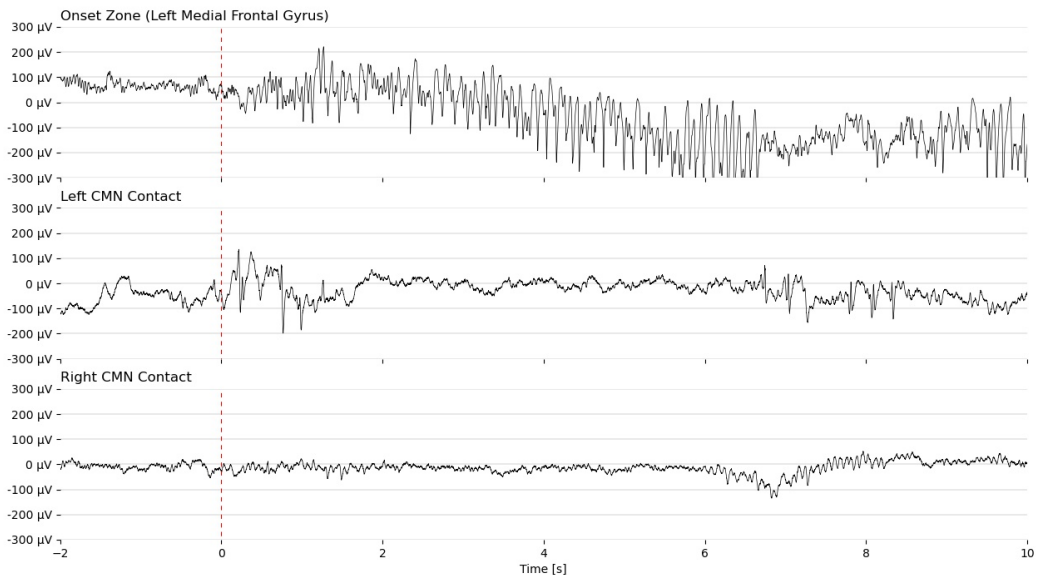


Figure 2.6: Example EEG traces from seizure of subject 7, showing a seizure with no CMN involvement following onset in left medial frontal gyrus electrode contact. Red lines mark seizure start and end. A global view of seizure evolution is shown in the top plot, while a detailed view of the first 10 seconds after onset is shown in the bottom. The bilateral CMN contacts do not deviate from baseline amplitude or activity pattern during the seizure.

2.5 Shortcomings of Current Methods

Intracranial monitoring of drug-resistant epilepsy patients generates tremendous amounts of data with the potential to improve understanding of epilepsy dynamics and direct clinical decisions. SEEG electrodes allow simultaneous recording of hundreds of brain areas at once. The SEEG monitoring protocol allows neurologists and epilepsy unit staff to observe patients' brain activity in real time while maintaining control over many environmental factors. Patients may also be instructed to perform tasks or exercises designed to provoke seizure activity, or undergo stimulation trials as previously mentioned.

However, SEEG monitoring is not without its drawbacks. Depth electrode implantation is a neurosurgical procedure performed under general anaesthesia; although surgical time is short and complications are rare and minor, the rationale for subjecting patients to intracranial monitoring must be carefully considered by a panel of physicians ahead of time. Patients with implanted electrodes must remain in the hospital under constant observation for the duration of a SEEG study, significantly (but temporarily) limiting their mobility and quality of life. Removal of the electrodes requires another operation. Still, in cases of difficult-to-treat epilepsy, the benefits of such an in-depth view of a patient's brain activity may significantly outweigh the drawbacks: clinicians may use SEEG data to better inform treatment planning, resulting in fewer failed treatment trials and improved quality of life.

To further contextualize the motivation for this thesis, it is important to note the shortcomings of the current clinical methodology for treatment planning as a result of SEEG recording. There exist two primary issues: sample size limitations of observed seizures, and lack of objective metrics for involvement of brain areas in seizure activity, an essential requirement for treatment planning.

In this particular study of CMN involvement, Neurologists relied on observed seizures to classify patients' CMN involvement and direct treatment, by analyzing seizure onset times, spread, and termination in SEEG recordings alongside prior non-invasive monitoring and imaging results. However, limited-time SEEG recordings may not always provide enough data to make significant clinical decisions. Five patients of the Nationwide CMN candidate group experienced 3 or fewer seizures during intracranial monitoring, and one of those patients experienced no seizures, and subsequently could not be offered new treatment options.

The current paradigm for clinical recommendation is based on subjective observation of seizure activity during SEEG monitoring. If a patient's seizures involve the CMN during initiation or generalization, it should be a viable treatment target. Although experienced neurologists may be effective in directing neuromodulation and treatment of drug-resistant seizures, it is critical to develop more objective criteria for determination of CMN involvement. Objective metrics would allow more widespread use and interpretation of SEEG

recordings, and may result in improved understanding of seizure dynamics for CMN patients. The goal of this thesis was to develop a framework that solves both issues described above. I address my proposed solutions in more detail in the following chapters.

Chapter 3

MATHEMATICAL METHODS

3.1 Overview

3.1.1 Sample Size Issues

Rigorous mathematical approaches may be used to overcome shortcomings of the current clinical approach to the analysis of SEEG data. Initial results from SEEG monitoring are promising, with patients responding well to SEEG-based treatment recommendations. However, developing statistically robust methods for determination of CMN involvement would reduce subjectivity of treatment decisions, ensure patients obtain maximal benefit from SEEG monitoring, and allow more widespread adoption of the monitoring paradigm. Sample size issues arising from dependence on observed seizures prevent the adoption of objective criteria for the definitive involvement of brain areas (in this cohort, specifically the CMN) in seizures. A possible solution involves using non-seizure data in place of seizures in the analysis.

Seizures are relatively rare events, making up a small fraction of SEEG recordings. The remaining data, totaling several days or weeks of recordings, remains largely unused. To derive maximal benefit from SEEG monitoring and address the sample-size issues of seizure frequency, I propose the use of interictal epileptiform events as potential biomarkers of CMN-involvement in patient-specific seizure networks. Interictal epileptiform events are short periods of epileptiform activity below the threshold of a seizure. They occur between seizures and manifest as abnormal EEG traces with insignificant clinical presence. Such epileptiform events are far more common than seizures, with each patient in the SEEG dataset experiencing hundreds or thousands of such events during each day of monitoring.

3.1.2 Interictal Epileptiform Events

Interictal events events are ubiquitous in epilepsy cases and are categorized into distinctive patterns including, but not limited to, interictal spikes, spindles, and spike-wave complexes. [36, 37]. Interictal spikes are sharp bursts of higher-than-background amplitude activity. They precede seizures and become more frequent approaching seizure genesis. Spindles are segments of narrow-band oscillatory activity, sometimes with varying amplitude. Spike-wave complexes, also known as spiking wave discharges or interictal epileptiform discharges, combine an initial sharp spike and oscillating wave component, similar to an interictal spike followed by spindle activity. Other epileptiform events may manifest as different combinations of spikes and waves, across multiple frequency bands.

These events posses similar characteristics to seizure activity. The working hypothesis, to be evaluated within this thesis and extensive further studies, is that if interictal epileptiform events are generated through similar processes as seizures, they may also share connectivity profiles with seizures. Specifically, the directed functional interactions between brain regions during interictal events may be similar to interactions during seizures.

In previous studies, events such as interictal spikes have been used as clinical markers preceding seizures[36] and interictal discharges have been shown to correlate with seizure activity and spread [38]. Additionally, some studies have examined the relationship between interictal activity and seizure onset zones [39] and attempted to use pre-ictal network structure to guide surgical treatment of epilepsy [40]. However, interictal events as a whole are not well studied and to my knowledge, no direct analysis of interictal connectivity regarding connections in thalamic nuclei has been done. Furthermore, few if any studies have attempted to provide a framework for the clinical use of SEEG data, which offers a superior amount of information compared to surface EEG and other non-invasive monitoring techniques. In this thesis, I introduce such a framework, for the use of interictal events as biomarkers of seizure activity in functional and connectivity analyses. I aim to provide a statistically robust approach to determination of CMN involvement in seizures, in a way that may be extended to more general involvement of epilepsy-significant brain regions in the future.

3.1.3 Procedure

First, interictal events must be detected and segmented. After a dataset of comparable interictal events is compiled, connectivity analysis is performed to identify directed interactions including the CMN. Finally, the results are compared to clinician determined CMN involvement from the current methodology.

In the following section, I present a review of the mathematical methods employed in the analysis of interictal events. Section 3.2 concerns time-frequency decomposition using wavelet transformations, enabling

identification and segmentation of interictal events by their distinctive spectro-temporal properties. In section 3.3, I establish models for neural dynamics of identified epileptiform events using linear autoregressive processes and related non-parametric approaches. Finally, sections 3.4 and 3.5 describe approaches to functional and directed connectivity analysis, starting from pairwise-coherence and extending to Granger causality for estimation of directed interactions.

3.2 Time-Frequency Decomposition

The spectral properties of SEEG signals are of significant interest to neuroscientific investigation. Neural activity has long been divided into frequency bands relating to brain states [41]. Seizures and other transient epileptiform events possess distinct frequency components and have been used as clinical markers in epilepsy monitoring and diagnosis.

The significance of various frequency components in neural signals make spectral analysis a useful tool for the detection and analysis of abnormal neural activity. Interictal spikes, spindles, and spike-wave discharges all possess distinct spectral characteristics, so time-frequency decomposition was employed to aid in their detection and segmentation.

Wavelet approaches were used due to their ease of implementation, simplicity of tuning, and useful property of sliding-scale time-frequency resolution. The wavelet chosen for this thesis was the Morlet wavelet, augmented using super-resolution techniques to improve time-frequency resolution of higher-frequency transients. Segmentation and annotation of interictal epileptiform events was carried out visually using a graphical user interface that combined time- and frequency-domain data. If necessary, more elaborate semi-automated approaches can be implemented for the detection and segmentation of abnormal EEG events using dimensionality reduction, clustering, and other computational techniques (such as those currently being developed by the Truccolo lab [42]).

3.2.1 Wavelet Transform

Multiple techniques exist for time-frequency decomposition, the most commonly used of which is the Fourier transform [43]. The Short-Time Fourier Transform (STFT) uses a fixed-length sliding window to construct a time-evolving power spectrum for a given time-domain signal. A power spectrum displays the power present in a signal as a function of frequency, typically for a range of desired frequencies (e.g. 1-100hz). Joining power spectra from multiple time windows across a segment of signal produces a spectrogram that illustrates the temporal evolution of signal power in various frequencies. Visual inspection of both time- and frequency-domain signals together can yield additional info for the detection of repeated patterns of neural

activity.

An important trade off in all spectral decomposition techniques is the balance between time and frequency resolutions. By the Heisenberg-Gabor uncertainty principle, it is impossible to localize a signal precisely in both time and frequency, and more precision in one domain results in a decrease in the other. For example, shortening the time window used in a STFT allows construction of spectrograms with more granular time steps. However, frequency resolution suffers as a result, and nearby frequencies become more difficult to distinguish.

Improved temporal resolution is important to properly identify and track a signal's evolution in time, while improved spectral resolution allows better discrimination between power in nearby frequencies. The STFT approach uses a constant time window resulting in unchanging time-frequency resolution. However, when dealing with some cases of neural data, it may be desirable to use a dynamic or sliding-scale time-frequency resolution. For example, a difference in frequency of 1 Hz is (in some situations) more significant in lower frequency bands than in higher ones, where shorter, high-frequency transients may be more easily noticed using smaller time steps.

Wavelet approaches such as the continuous wavelet transform (CWT) offer a convenient way to generate spectrograms using longer windows for lower frequencies and shorter windows for higher frequencies. This allows for the preservation of high resolution in frequency for slower bands and improved temporal discrimination in faster bands. The wavelet approach to time-frequency decomposition involves the convolution of time-domain signal with families of 'wavelets' or filter kernels corresponding to each frequency of interest. A description of the Morlet wavelet [44] and some of its properties is provided below, closely following the expositions of Bruns and Moca et al [43, 45].

The Morlet wavelet is constructed by multiplying a Gaussian envelope by a complex oscillation (plane wave). For a central frequency f and number of cycles c the corresponding Morlet wavelet $\Psi_{f,c}$ is defined as

$$\Psi_{f,c}(t) = \frac{1}{B_c \sqrt{2\pi}} e^{\frac{-t^2}{2B_c^2}} e^{i2\pi ft}, \quad (3.1)$$

with time-spread parameter

$$B_c = \frac{c}{k_{sd} f}, \quad (3.2)$$

set so the plane wave fills c cycles in k_{sd} standard deviations of the Gaussian. The time-spread parameter controls the time variance of the wavelet. Increasing it improves frequency resolution at the expense of time resolution and vice versa. The frequency scaling in B_c results in the desired sliding-scale time-frequency resolution of the CWT. Setting a constant k_{sd} is a design choice that sets the *relative* time-frequency resolution

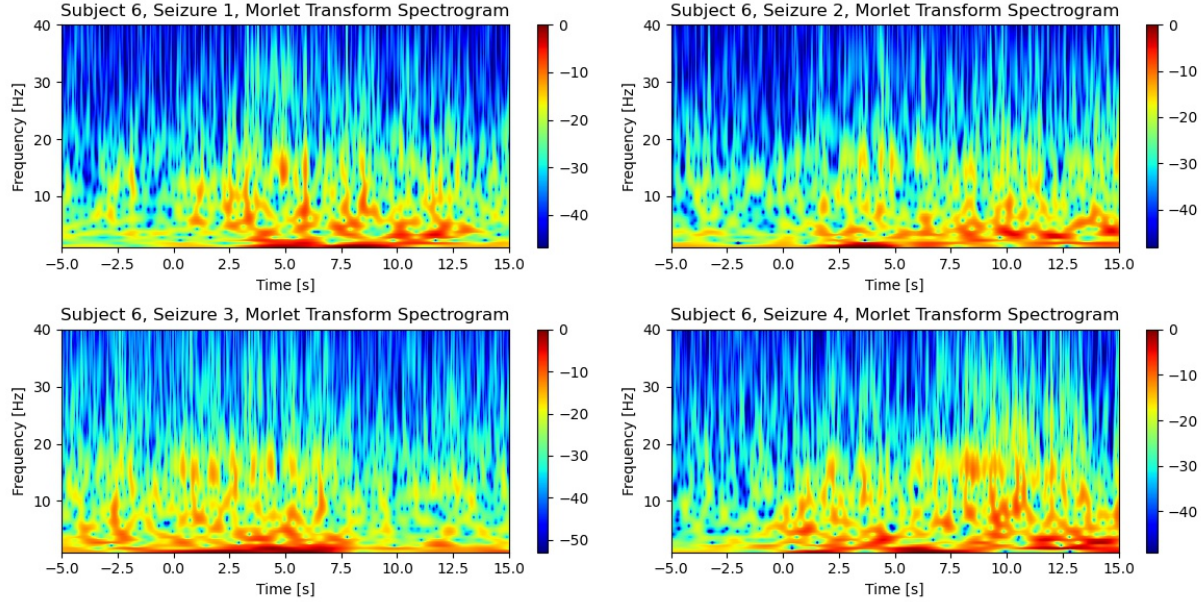


Figure 3.1: Morlet-based spectra of seizure recording sections (20s each) for subject 6. The signal is bipolar montage of Right Anterior Insula trajectory contact 8. The Morlet transformation results in noticeable “banding” corresponding to poor frequency resolution at higher frequencies of the spectrogram.

for a spectrogram, the CWT time-evolving graph corresponding to a Fourier-generated spectrogram. Wavelets are usually normalized to have unit energy ($\|\Psi_{f,c}(t)\| = 1$).

Convolution of a signal $s(t)$ with the wavelet $\Psi_{f,c}(t)$ at each frequency of interest $f \in F$ produces a complex signal

$$S^\Psi(f, t) = s(t) * \Psi_{f,c}(t). \quad (3.3)$$

This analytic signal is functionally equivalent to that produced by the Fourier transformation approach, and the parameters of each approach can be tuned to produce the same results [43]. As an analytic signal recovers only half of the power of the real signal, the response of a signal to each wavelet is given by

$$R[\Psi_{f,c}] = \sqrt{2} \times s(t) * \Psi_{f,c}(t), \quad (3.4)$$

for each frequency f of interest.

The Morlet transformation was implemented in Python, using zero-padding and multiplication in the Fourier domain in place of time-domain convolution. Wavelet width was set to $c = 7$ cycles and each wavelet was normalized so the squared magnitudes of the wavelet coefficients summed to 1. The Morlet transform requires fewer parameters than the STFT, making it simpler to tune than the alternative. Additionally, the

wavelet structure already includes a window function (Gaussian) and does not require window selection or a multitaper estimator. Example Morlet spectra of seizure recordings are shown in figure 3.1.

The sliding-scale time-frequency resolution offers superior localization of transients and oscillation packets in time. However, it may fail to differentiate between neighboring frequencies in higher-frequency regions of a spectrogram. A realization of a stationary autoregressive (*AR*) process with two neighboring high-frequency peaks — 155 Hz and 180 Hz — in the theoretical power spectrum (figure 3.2) is used to illustrate the problem. An introduction to *AR* processes and their theoretical power spectra is provided in sections 3.3 and 3.5.

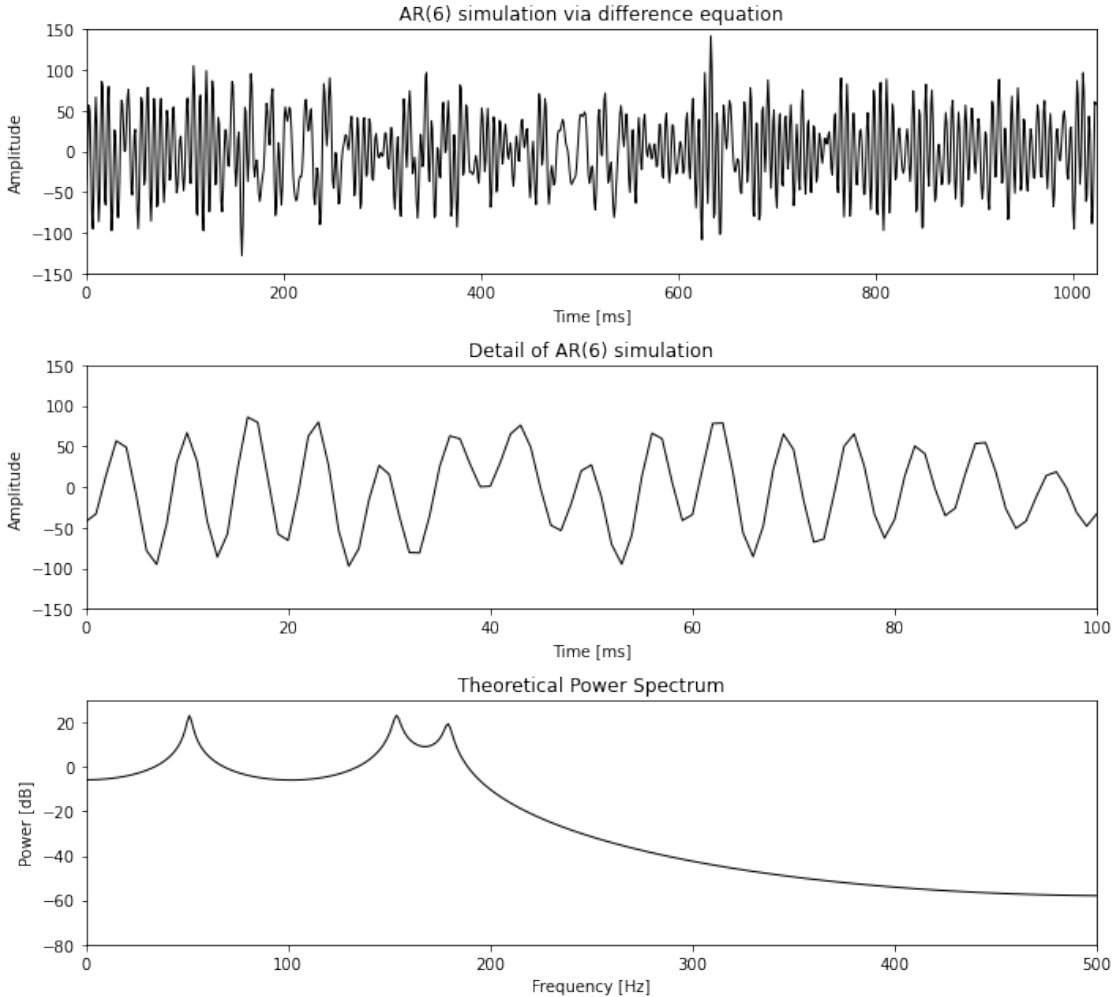


Figure 3.2: Example stationary AR(6) process realization (top) with detail (center) and theoretical power spectrum derived from the AR coefficients (bottom). This order-6 AR process has coefficients 3.9515, -7.8885, 9.7340, -7.7435, 3.8078, -0.9472 for time lags $\tau = 1, \dots, 6$, respectively.

The Morlet transform spectrum (figure 3.3) fails to differentiate between the high frequency oscillations at 155 Hz and 180 Hz, instead displaying power in a wide frequency band spanning between the two transient frequencies. (Incidentally, I also note that the observation of time-transient events on the wavelet time-

frequency decomposition does not imply that the underlying process is nonstationary. The chosen AR(6) here is stationary by construction. In fact, the oscillatory transients related to only one of the peaks in the theoretical power spectrum can also be directly observed in the time series itself.)

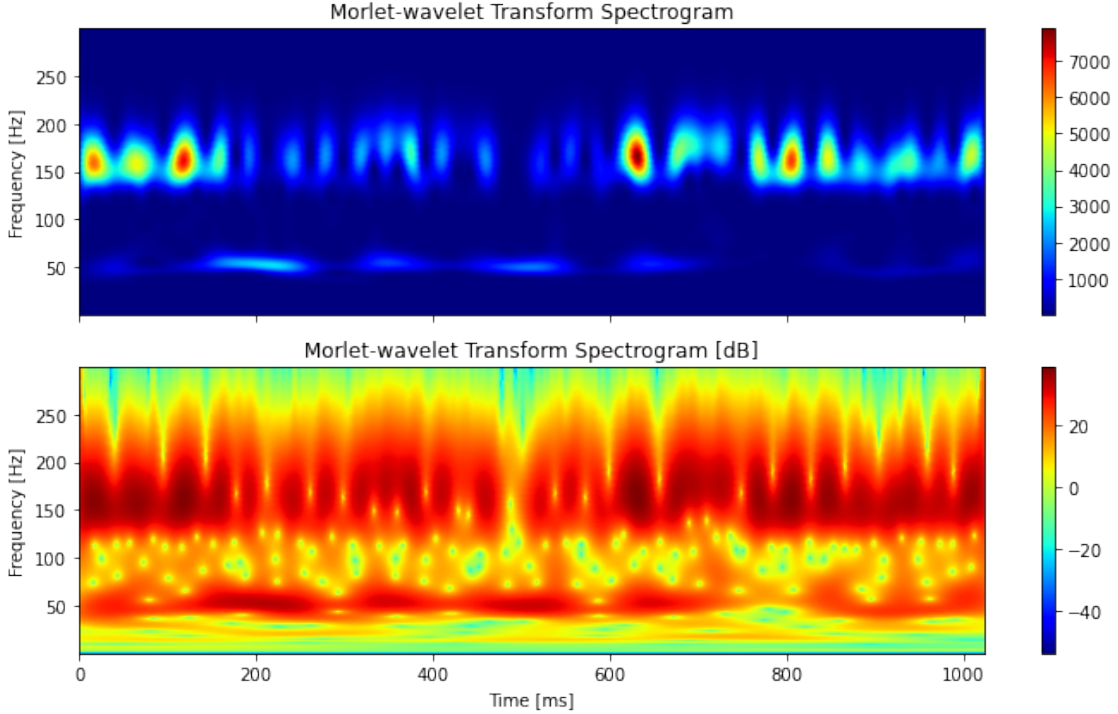


Figure 3.3: Morlet-based spectra of the AR(6) process realization in (figure 3.2). Note the insufficient frequency resolution between 150 and 175hz.

3.2.2 Super-Resolution Wavelet Transform

When needed, an alternative approach, the super-resolution wavelet (superlet) transform [45] can be used to remedy the time-frequency resolution issue. The superlet transform (SLT) is a super-resolution technique that aims to improve the time-frequency resolution of a wavelet spectral estimator by using an ensemble of multiple wavelets with different time-spread parameters. Although superlets are not restricted to a specific wavelet, Morlet wavelets are used for both the example and further analysis. The SLT method is analogous to similar super-resolution techniques as applied to Spectrograms (i.e. ensembles of different window sizes). In essence, the SLT of order o uses a superlet $SL_{f,o}$, a set of o Morlet wavelets, for each frequency f

$$SL_{f,o} = \{\Psi_{f,c} | c = c_1, c_2, \dots, c_o\}, \quad (3.5)$$

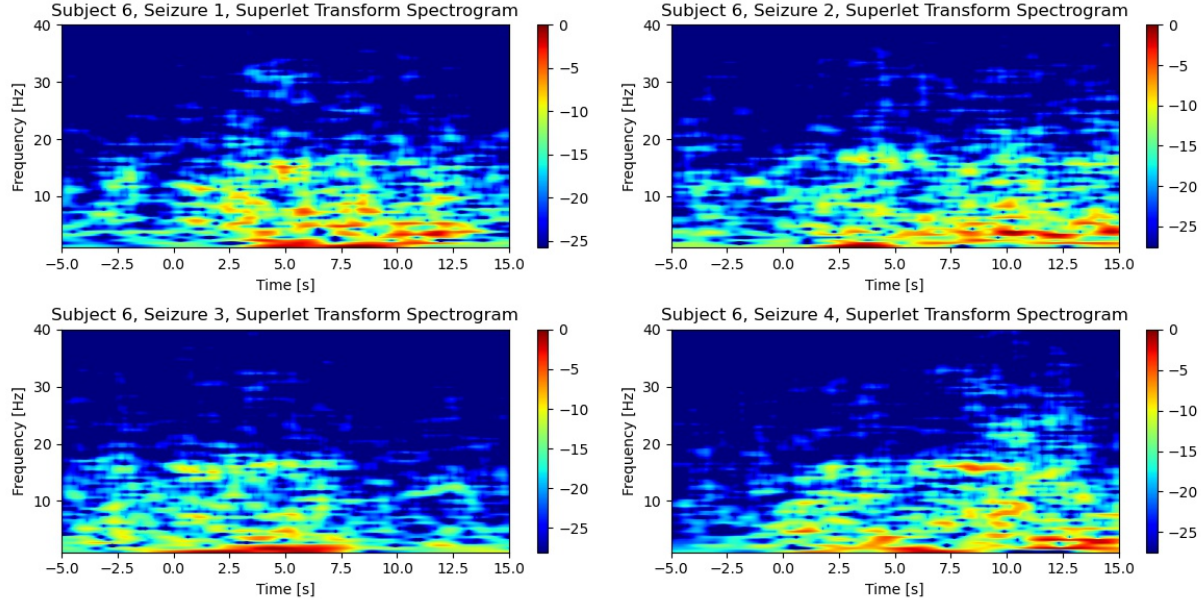


Figure 3.4: Superlet-based spectra of seizure recording sections (20s each) for subject 6. The signal is bipolar montage of Right Anterior Insula trajectory contact 8.

where c_i is the number of cycles in the i -th wavelet of the superlet, increasing either additively ($i = i + c_1 - 1, i = 2, \dots, o$) or multiplicatively ($i = i * c_1, i = 2, \dots, o$). Consequently, an order-1 superlet is just a regular Morlet wavelet with $c = 1$ cycles.

The response of the signal to a superlet is computed as the geometric mean of the individual wavelet responses (equation 3.4)

$$R[SL_{f,o}] = \sqrt[\circ]{\prod_{i=1}^o R[\Psi_{f,c_i}]} \quad (3.6)$$

An SLT is computed analogously to a CWT. Using an order-1 superlet results in an SLT identical to the CWT. By increasing the order, more wavelets with greater cycle parameter c_i are included in the computation. A greater number c_i increases the value of the time-spread parameter B_c , resulting in increased time-variance and frequency resolution. As a result, the additional wavelets included in the superlet serve to better localize the signal in frequency. The improved resolution comes at increased computational cost, as construction and convolution of $n(F) * o$ wavelets with the signal is required to construct an SLT spectrum compared to $n(F)$ of each operation otherwise.

To somewhat remedy the increased computational cost, Moca et al. proposed an 'adaptive' superlet transform (ASLT). As the issue with CWT time-frequency resolution emerges at higher frequencies, the relative benefit of higher-order superlets increases with frequency as well. For lower central frequencies, it is

sufficient to use lower order (starting with $o = 1$) estimators. The ASLT scales the order parameter linearly with frequency. It requires an additional two parameters o_{\min}, o_{\max} that define the minimum and maximum order for superlet construction, respectively. The order of each superlet is then

$$o(f) = \text{ceil} \left(o_{\min} + \left[(o_{\max} - o_{\min}) \cdot \frac{f - f_{\min}}{f_{\max} - f_{\min}} \right] \right), \quad (3.7)$$

and the spectrum is estimated similarly to the SLT. Figure 3.4 shows spectra of the same seizure data as in 3.1, using the superlet transform to improve frequency resolution and reduce banding.

For a more intuitive example, the ASLT of the AR(6) process from figure 3.2 for orders 1 and 20 are shown in figure 3.5. The order-1 superlet is nearly identical to the Morlet wavelet spectrum, with minor differences due to implementation differences and normalization (the superlet normalization is to the integral of the modulus of the energy, not to squared energy magnitude). While the Morlet and order-1 spectra cannot discriminate between the two transients in the AR spectrum, the order-20 superlet transform allows for two bands to be visible, although with reduced time resolution. Figure 3.6 examines a section of the AR(6) realization where the Morlet and order-1 superlet spectra fail to resolve the two high-frequency transients. As the order parameter increases, the gradual trade-off from time to frequency resolution is illustrated.

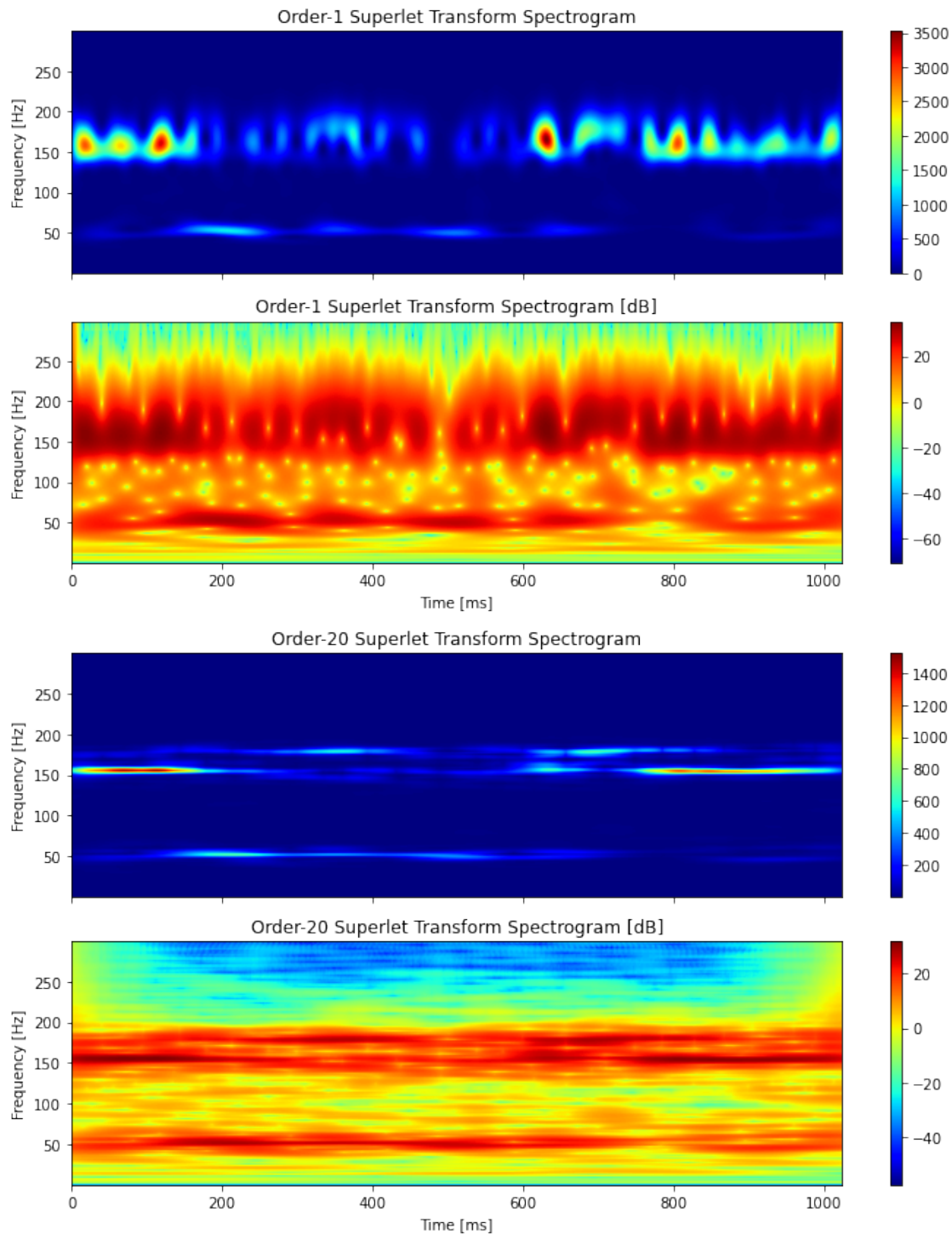


Figure 3.5: Adaptive superlet transform (top = order 1, bottom = order 20) of a single AR(6) process realization (figure 3.2).

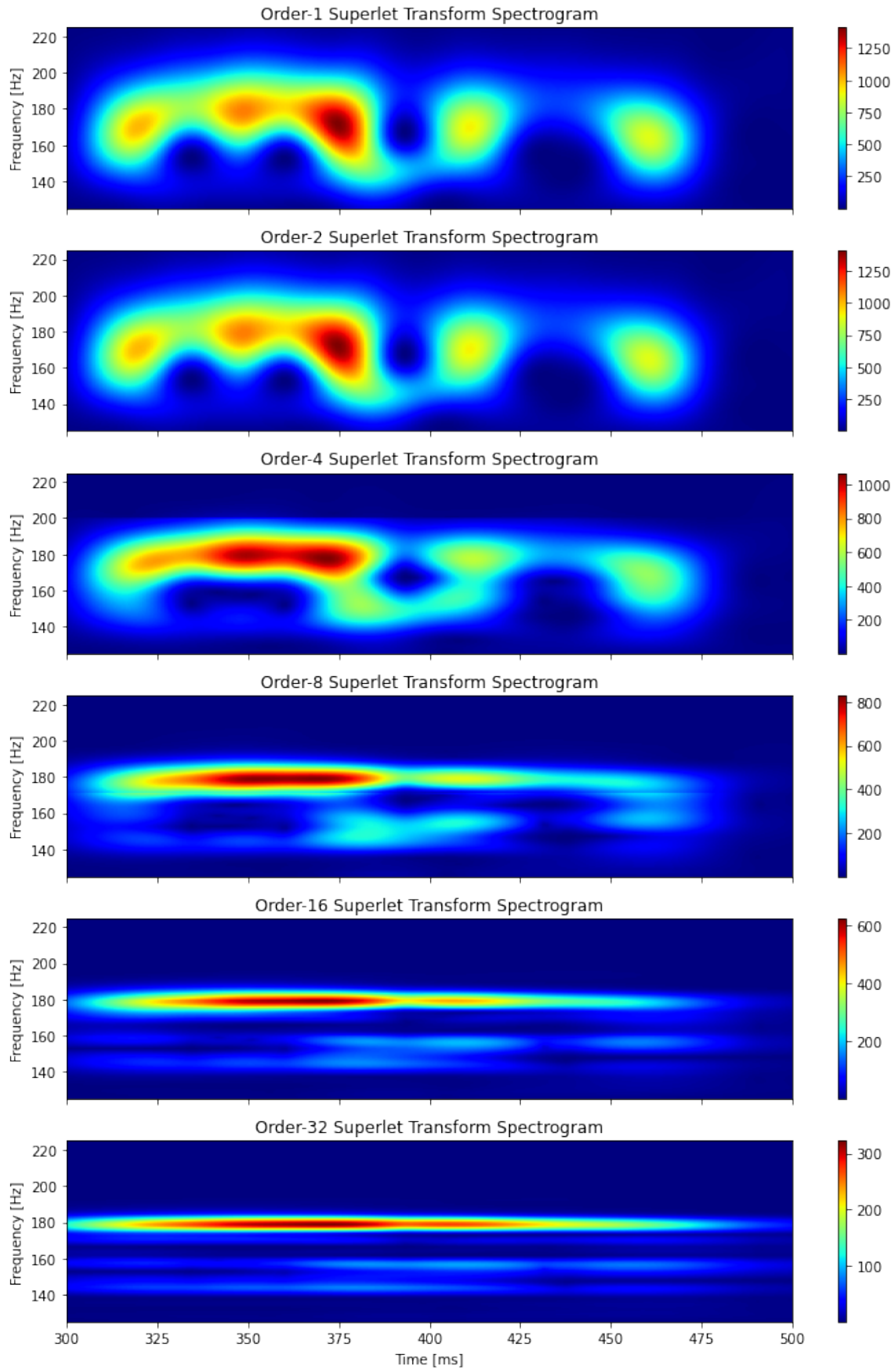


Figure 3.6: Superlet spectrum of a single AR(6) process realization (figure 3.2, $t = 300$ to 500) for increasing orders of the adaptive superlet transform.

3.3 Modeling of Neural Data

Neural data is inherently complex. Billions of connected neurons result in highly nonlinear brain dynamics, further complicated by the omnipresence of noise in neural circuits [46]. Stochastic modeling is used to represent neural data such as time series from SEEG recordings. However, the analysis of nonlinear dynamical systems is difficult if not impossible, necessitating simpler representations of neural time series data to draw meaningful conclusions from their analysis.

3.3.1 Stochastic Processes

To begin, generic macroscopic neural dynamics are represented in terms of a nonstationary, continuous-time, nonlinear stochastic process given by

$$dX_t = f(X_t) dt + g(X_t) dW_t, \quad (3.8)$$

where the above stochastic differential equation may be understood according to the Ito calculus [47]. The noise W_t is the standard Wiener process, such that W_t is continuous in t , and dW_t are the corresponding increments. (In this section, the subscript t denotes either continuous or discrete time, with the specific case being clear from context).

This analysis will focus on locally stationary steady state dynamics (e.g. segmented interictal epileptiform events). If the dynamical system is close to a steady-state, and provided stochastic fluctuations are not too large, a useful approximation is given by its first-order Taylor expansion (disregarding non-linear $O(2)$ and above terms). Assuming additive noise allows approximation as a linear stochastic process of the form

$$dX_t = \alpha(\mu - X_t)dt + \beta dW_t, \quad (3.9)$$

for $\alpha, \beta > 0$. This is the Ornstein-Uhlenbeck Process, the only non-trivial stochastic process that is simultaneously Gaussian, Markov, and stationary (temporally homogeneous, or mean-reverting in this case). For $\mu = 0$ it is a zero-mean process centered at $x = 0$. The Ornstein-Uhlenbeck process still operates in continuous time. Its discrete time analogue is the first-order autoregressive AR(1) process

$$X_t = aX_{t-1} + \varepsilon_t, \quad (3.10)$$

with regression coefficient $|a| < 1$, and zero-mean (μ) and variance (σ) Gaussian white noise term ε_t . The constant mean is set to zero so the corresponding term is omitted above.

Multivariate and higher-order versions of the above linear autoregressive models will be the main component of the parametric approach for spectral and directed connectivity analyses in this thesis. Non-parametric approaches relying on Fourier (or wavelet) transforms of the data will also be used. Although they do not require parametric model fitting, these approaches remain tightly related to linear system analyses, instead modeling the underlying signal as a linear combination of harmonic signals according to their Fourier coefficients.

3.3.2 Linear Autoregressive Models

The AR(1) equation 3.10 derived earlier is the simplest form of a linear autoregressive model, a class of discrete-time representations of stochastic processes using linear combinations of preceding terms to predict future steps of the process. The first-order model uses only the immediately preceding term to predict the next one, and expanding the model order p may lead to more accurate forecasting by accounting for longer-term history effects. Furthermore, higher-order autoregressive terms are required to capture different damped oscillatory modes of neural dynamics. Increasing order does not necessarily improve model accuracy, however, and criteria for optimal model order selection is discussed later in this chapter.

A linear AR(p) model, also known as an order- p AR process, takes the form

$$X_t = \sum_{\tau=1}^p a_\tau X_{t-\tau} + \varepsilon_t, \quad (3.11)$$

where the single coefficient a in the AR(1) model is replaced by a vector $\langle a_1, a_2, \dots, a_p \rangle$ of length p containing coefficients for each time-lag $\tau \in \{1, p\}$. For a Gaussian AR(p) process, the ε_t noise term is a Gaussian white noise random variable.

An AR(p) process of any order can be expressed as a first-order Markov process by state space augmentation

$$Z_t = \mathcal{A}Z_{t-1} + E_t, \quad (3.12)$$

where $Z_t = [Z_t, Z_{t-1}, \dots, Z_{t-p}]^T$, \mathcal{A} is the *companion matrix* representation of the process coefficients

$$\mathcal{A} = \begin{bmatrix} a_1 & a_2 & \dots & a_{p-1} & a_p \\ 1 & 0 & \dots & 0 & 0 \\ 0 & 1 & \dots & 0 & 0 \\ \dots & \dots & \ddots & \dots & \dots \\ 0 & 0 & \dots & 1 & 0 \end{bmatrix}, \quad (3.13)$$

and E_t is a noise vector with first element ε_t and other elements zero. One way to determine stability (and stationarity) of an AR(p) process is to construct the corresponding companion matrix and calculate its spectral radius. The spectral radius $\rho(A)$ is equal to the absolute magnitude of the largest eigenvalue $\maxindex(|\lambda_i|)$ of A . Geometrically, the eigenvalues represent the scale factor of each orthogonal eigenvector for the linear transformation encoded by A . If the largest eigenvalue lies within the unit circle, repeated applications of the transformation A remain bounded. (In the case of an AR(1) process, the condition is $|a| < 1$.) As long as the spectral radius condition is met, the coefficient weights in the AR(p) model will cause past terms' contribution, as well as the effects of perturbations, to decrease exponentially over time. The process is thus stable and stationary.

AR(p) model parameters can be fitted using maximum likelihood, Yule-Walker reverse solutions, or maximum-entropy estimation methods [48]. There is no closed-form solution for (unconditional) maximum likelihood estimation, so conditional MLE such as least-squares regression can be used instead. Maximum entropy approaches such as the Burg maximum entropy method are also used, and have particular benefits for spectral estimation [48, 49, 50]. Selection of optimal model order p is carried out through the use of penalized log-likelihood information criteria (e.g. Akaike information criterion or Bayesian information criterion [48]), through analysis of sample partial autocorrelation functions conditioned on a number of time lags, through cross-validation approaches, or a combination of more than one of these methods.

3.3.3 Vector Autoregressive Models

So far, only univariate linear AR(p) models have been considered, representing individual stochastic processes or time series X_t . However, neural data often includes multi-channel recordings. Extending the AR(p) framework to multivariate time series is necessary to represent higher dimensional real-world data, such as SEEG recordings with 100 or more channels. A vector autoregressive (VAR(p)) or multivariate autoregressive (MVAR(p)) model of a multivariate time series $X_t \in \mathbb{R}^M$ takes the form

$$X_t = \sum_{\tau=1}^p A(\tau) X_{t-\tau} + \varepsilon_t, \quad (3.14)$$

where $A(\tau)$ for $\tau = 1, 2, \dots, p$ are $M \times M$ coefficient matrices for each time lag. Specifically, $A(\tau)_{ij}$ corresponds to the coupling coefficient from channel $j \rightarrow i$ at time $t - \tau$. The noise term ε_t is a Gaussian white noise vector with $M \times M$ covariance matrix Σ . The ε_t of a Gaussian white noise process are independent and identically distributed in time (instantaneous noise correlations are allowed and Σ is generally non-diagonal).

A companion matrix can be constructed for state-space augmentation of a VAR(p) model in a similar way to that of a AR(p) model, using block matrices in place of individual coefficient entries. The model is then

similarly represented as a first-order Markov process. The companion matrix \mathcal{A} takes the form

$$\mathcal{A} = \begin{bmatrix} A(1) & A(2) & \dots & A(p-1) & A(p) \\ \mathbf{I} & 0 & \dots & 0 & 0 \\ 0 & \mathbf{I} & \dots & 0 & 0 \\ \dots & \dots & \ddots & \dots & \dots \\ 0 & 0 & \dots & \mathbf{I} & 0 \end{bmatrix}, \quad (3.15)$$

where $A(\tau)$ are the coefficient matrices from equation 3.14, each \mathbf{I} is an $M \times M$ identity matrix, and each 0 is an $M \times M$ null block matrix. Stability of a VAR(p) model is ensured by the spectral radius restriction $\rho(\mathcal{A}) < 1$. The most commonly used methods for parameter estimation are conditional MLE (least-squares), Yule-Walker reverse solutions, and the maximum entropy methods. The same model order selection approaches listed for the univariate case can be used.

3.3.4 Impulse Response and Transfer Function

Any stationary autoregressive process can be characterized by its impulse response function: the observed change in the process based on a one-unit increment of the noise input at a given time t . The impulse response h_τ is informally defined by $h_\tau = \frac{\partial X_{t+\tau}}{\partial \varepsilon_t}$ where $\tau = 1, 2, \dots$, as previously, X_t is a stationary stochastic time-series represented as a linear autoregressive process with Gaussian white noise input ε_t . For an AR(1) process, h_τ corresponds to $a^\tau; \tau \geq 0$. For an VAR(p) process, h_τ corresponds to $[A^\tau]_{1,1}$. Stationary processes have finite memory for input perturbations, as a result of the stability condition, so $\lim_{t \rightarrow \infty} h(t) = 0$.

An AR process can also be simulated by convolution of its impulse response $h(t)$ (single-variable case) or $H(t)$ (multi-variate case) and white noise input sequence ε_t

$$X_t = [H * \varepsilon](t). \quad (3.16)$$

By the convolution theorem, convolution in the time domain corresponds to multiplication in the frequency domain, so a spectral representation of the process, denoted by $X(f)$, is given by

$$X(f) = H(f) \times E(f), \quad (3.17)$$

where $H(f)$ and $E(f)$ are the Fourier-transformed impulse response and white noise sequence, respectively, at a given frequency f . $H(f)$ is known as the transfer function of the process, and can be used for spectral estimation. This representation is important for the computation of power spectra, spectral pairwise coherence,

and spectral Granger causality, discussed in the following sections.

3.4 Connectivity Analysis

There are two main ways of categorizing brain connectivity: structural and functional [51]. Structural connectivity arises from physical connections both within the same and between different brain regions (e.g. white-matter connectivity), and is effectively static in the short time scales considered here. Functional connectivity, on the other hand, is dynamic and changes with behavior, perception, and other impacts on brain state. Changes can occur at time scales as short as tens-to-hundreds of milliseconds [52], and often provide insight into neural function and dysfunction.

Both structural and functional connectivity are relevant to epilepsy [53]. Functional connectivity is particularly significant as seizures as they present with altered connectivity profiles involving their onset, propagation, and termination. SEEG recordings contain time series sampled from over 100 depth electrode contact points, distributed between deep medial structures and cortex. Relationships among time series sampled from distinct brain areas provide the basis for connectivity analysis.

Before getting to connectivity measures, auto- and cross-covariance functions are defined, as well as related expressions for auto- and cross-power spectra.

3.4.1 Covariance Functions and Power Spectra

For two stochastic processes $\{X_{m,t}, X_{n,t}\}$ with a joint probability density function $f_{t_1 t_2}(X_{m,t_1} = x_m, X_{n,t_2} = x_n)$, the covariance function can be defined as

$$\begin{aligned} R_{X_m X_n}(t_1, t_2) &= \mathbb{E}[(X_{m,t_1} - \mu_{m,t_1})(X_{n,t_2} - \mu_{n,t_2})] \\ &= \mathbb{E}[X_{m,t_1} X_{n,t_2}] - \mu_{m,t_1} \mu_{n,t_2} \\ &= \int_{-\infty}^{+\infty} \int_{-\infty}^{+\infty} x_m x_n f_{t_1 t_2}(X_{m,t_1} = x_m, X_{n,t_2} = x_n) dx_m dx_n - \mu_{m,t_1} \mu_{n,t_2}. \end{aligned} \tag{3.18}$$

For wide-sense (second-order) stationarity, one only requires the means to be constant functions of time and the covariance function to depend only on the time lag, i.e. $R_{X_m X_n}(t_1, t_2) = R_{X_m X_n}(\tau)$ for $\tau = t_2 - t_1$, but not on the specific time locations. Under these stationarity conditions and for $R_{X_m X_n}$ that are rapidly decreasing functions of time lag, the power spectrum can be defined as the Fourier transform of the covariance function

$$S_{X_m, X_n}(f) = \int_{-\infty}^{+\infty} R_{X_m X_n}(\tau) e^{-i2\pi f \tau} d\tau, \tag{3.19}$$

for a range of frequencies f .

For $m = n$ the above corresponds to the auto-power, a real valued quantity since $R_{X_m X_n}$ is an even function. For $m \neq n$ one obtain the cross-power, in general a complex valued quantity.

The above is mostly a definition for theoretical purposes and uses. In practice, one computes of power spectra of time series by applying the discrete Fourier transform directly to the data (periodogram) or, to address bias and variance issues of the periodogram estimator, to tapered time series (multitaper spectral estimation).

For a multivariate time series, a spectral matrix $S_{m,n}(f)$, with entries m and n indexing recorded channels, can then be estimated. It is a Hermitian operator with $S(f) = S^\dagger(f)$, that is the matrix $S(f)$ is self-adjoint, or equal to its own conjugate transpose. For instance, a periodogram-like estimator for the spectral density matrix $\hat{S}(f)$ is given by

$$\hat{S}_{m,n}(f_r) = \frac{\Delta^2}{T} \left[\sum_{t=0}^{N-1} X_{m,t} e^{-i2\pi \frac{r}{N} t} \right] \left[\sum_{t=0}^{N-1} X_{n,t} e^{-i2\pi \frac{r}{N} t} \right]^*, \quad (3.20)$$

where Δ is the sampling interval (time units in seconds for frequency in Hz), T is the time duration of the time series, and $*$ denotes the complex conjugate. The term $r = 1, 2, \dots, N$ indexes both negative and positive frequencies (two-sided spectra). (For one-sided spectra, the above is multiplied by 2, $r = 1, 2, \dots, N/2$ for even N , and $f_r = r/T$ in Hz). As stated above, because of the known bias and variance issues of the periodogram, multitaper spectral estimation is used instead [48].

These approaches of estimating power spectra from Fourier transforms (or related wavelet transforms) of the time series are commonly referred to as a non-parametric approach.

Alternatively, parametric approaches based on estimated VAR(p) models can be used. Advantages and disadvantages with respect to non-parametric approaches are discussed in [48].

For a VAR(p) process, the spectral matrix $S(f)$ can be estimated using the transfer function $H(f)$ first discussed in section 3.3.4. The transfer function of a VAR(p) process is computed as

$$H(f) = \left[\mathbf{I} - \sum_{k=1}^p A(k) e^{-i2k\pi f} \right]^{-1}, \quad (3.21)$$

resulting in the frequency representation (equation 3.17)

$$X(f) = H(f) \times E(f) = \left[\mathbf{I} - \sum_{k=1}^p A(k) e^{-i2k\pi f} \right]^{-1} E(f). \quad (3.22)$$

The spectral matrix $S(f)$ can then be derived as an expectation over realization (trials) or over time samples (given ergodicity):

$$\begin{aligned}
S(f) &= \lim_{N \rightarrow \infty} \frac{1}{N} \mathbb{E}(X(f)X^\dagger(f)) \\
&= \lim_{N \rightarrow \infty} \frac{1}{N} \mathbb{E}([H(f)E(f)][H(f)E(f)]^\dagger) \\
&= H(f) \left[\lim_{N \rightarrow \infty} \frac{1}{N} \mathbb{E}(E(f)E^\dagger(f)) \right] H^\dagger(f) \\
&= H(f)\Sigma H^\dagger(f),
\end{aligned} \tag{3.23}$$

where Σ is the zero-lag covariance matrix of the white noise process, which can be estimated from real-world data by computing residual errors of the predicted X_t from VAR(p) process coefficients.

3.4.2 Undirected Spectral Connectivity Estimates

The simplest spectral estimates of connectivity are undirected metrics such as coherence and partial coherence. They are preferred over cross-correlation functions because they differentiate between temporal correlations occurring in different frequency bands. Frequency-domain correlations in neural data are important because oscillatory activity is a proposed mechanism for communication between brain areas [54]. Coherence can be estimated using either parametric or non-parametric approaches, where frequency spectra are estimated from autoregressive models or by applying time-frequency decomposition (e.g. Fourier transforms) directly to observed data, respectively.

Spectral coherence $C(f)$ is a measure of linear dependency at specified frequencies f between pairs of time series. It is defined as a function of spectral cross-power and auto-power between two channels of a multivariate process:

$$C_{X_m X_n} = \left[\frac{|S_{X_m X_n}(f)|}{\sqrt{S_{X_m X_m}(f)} \sqrt{S_{X_n X_n}(f)}} \right]^2 = \frac{|S_{X_m X_n}(f)|^2}{S_{X_m X_m}(f) S_{X_n X_n}(f)}, \tag{3.24}$$

where $|\cdot|$ is the complex modulus. Coherence ranges from 0 to 1 and is the spectral analogue of correlation. The squared coherence is analogous to the coefficient of determination R^2 . It thus quantifies the explained variance at a given frequency f from one process to another.

When estimated from time series data, the (squared) coherence is given by

$$C_{X_m X_n} = \frac{|\langle S_{X_m X_n}(f) \rangle|^2}{\langle S_{X_m X_m}(f) \rangle \langle S_{X_n X_n}(f) \rangle}, \tag{3.25}$$

where the brackets denote averaging over K trials

$$\langle S_{X_m X_n}(f) \rangle = \frac{1}{K} \sum_{k=1}^K S_{X_m X_n, k}(f). \quad (3.26)$$

Coherence estimated from a single realization is always equal to 1. Thus, estimation requires multiple trials or, alternatively, if only a single trial is available, coherence can be estimated by averaging over spectral estimators obtained by applying multiple tapers to the data (multitaper spectral estimation). Informally, pairwise coherence depends on the distribution of the relative-phases at a give frequency between two time series across multiple realizations. A uniform distribution implies zero coherence, while a very peaked distribution implies coherence close to 1.

Beyond pairwise coherence, partial coherence (the spectral analogue of partial correlation) can be computed for multivariate system of dimensions $M > 2$. The measure of partial coherence for an M dimensional process is computed using submatrices (minors) of the spectral matrix $S(f)$ consisting of every channel:

$$C_{ij| \{1\dots M\}_{ij}} = \frac{|\mathcal{M}_{ij}(f)|}{\sqrt{|\mathcal{M}_{ii}(f)|} \sqrt{|\mathcal{M}_{jj}(f)|}}, \quad (3.27)$$

where \mathcal{M}_{ij} is the submatrix formed by removing row i and column j of the spectral matrix $S(f)$. In this case, $|\cdot|$ represents the determinant of a submatrix.

No known sampling distribution exists for spectral coherence or partial coherence, so significance testing and estimation of confidence intervals is commonly done through bootstrapping and random resampling methods.

The partial coherence of a multivariate stochastic process or collection of real-world time-series recordings can begin to reconstruct network structure. However, it cannot infer direction of interactions (i.e. the resulting graph of the neural circuit is undirected) and cannot resolve indirect interactions, such as chains of successive connections.

For example, in the trivariate system $\{X_t, Y_t, Z_t\}$ with three directed edges — $X_t \rightarrow Y_t$, $Y_t \rightarrow Z_t$, and $Z_t \rightarrow Y_t$ — shown in figure 3.7, the partial coherence network may fail to resolve the indirect connection between X_t and Z_t .

3.5 Directed Interactions

The primary drawback of coherence-based approaches to functional connectivity is their lack of directionality. Understanding the path of information flow between nodes in a neural network, which need not be bi-

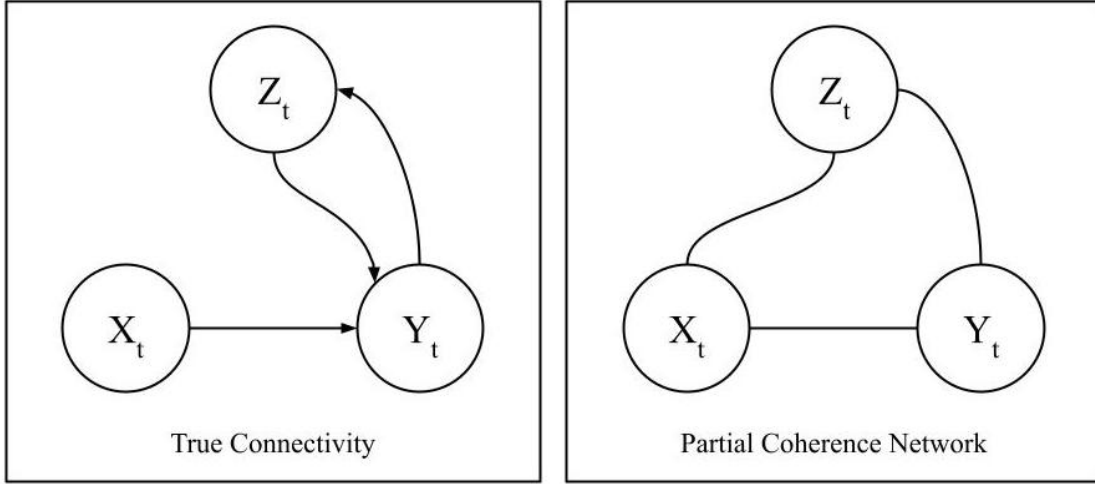


Figure 3.7: True connectivity of example trivariate process(left) and predicted connectivity from partial coherence (right). Note the lack of directionality, as well as the spurious connection from the indirect effect from $X_t \rightarrow Z_t$.

directional, is critical for this project as direction of seizure spread is tightly related to the hypothetical role of different brain areas (such as the CMN) in focal seizure generalization.

True causality is a longstanding and difficult philosophical question; for this thesis, the metaphysical debate is avoided by operationalizing causality in terms of time precedence and forecasting ability between different time-series, as Granger or Geweke-Granger causality. First applied by Clive Granger in 1969 using the language of stationary autoregressive processes.

3.5.1 Granger Causality

Informally, a stochastic process X Granger-causes (“G-causes”) or *drives* a stochastic process Y if the history of X improves the prediction of Y beyond what can be already predicted by the history of Y itself [55]. John Geweke extended Granger’s formulation of G-Causality in 1982 and 1984 papers by breaking down rigorous statistical tests for pairwise and conditional G-causality, respectively [56, 57], along with his first formulation of G-causality in the spectral domain.

Pairwise Geweke-Granger causality measures relationships between pairs of time-series without conditioning for other (causal) influences. Conditional causality, much like partial coherence, conditions for influences of all channels or time-series in a multivariate system. For this project, conditional G-causality is preferred for its ability to discern indirect effects in complex multi-node networks.

Conditional Geweke-Granger causality has long been used to infer directed relationships in neural systems [49, 58, 59, 50]. An important consideration to be kept in mind is that, because current SEEG recordings provide only a small subsampling of the full brain networks, spurious directed interactions are possible given

the unmeasured (hidden) network nodes. As a result, G-causality cannot definitively recover the *complete* network structure as data sampling methods restrict access to information about the entire network. To alleviate these issues, G-causal analyses can be complemented by incorporating connectome or structural connectivity information (e.g. white-matter tractography [60]) as well as perturbation of network activity with electrical stimulation at target nodes or areas [61]. For the purpose of this thesis, G-causality may be sufficient to suggest initial conclusions about relationships between different brain areas and structures. G-causal analysis is also useful for finding biomarkers of clinical activity such as seizure generalization.

Under my hypothesis, a G-causal network inferred from interictal epileptiform recordings would be correlated with the true seizure network. If the spread of interictal epileptiform events according to the inferred interictal network shows similar dynamics as the spread of seizure activity — e.g. from seizure onset zones, to CMN, to general cortex — corresponding with neurologist-determined CMN involvement, it would provide evidence that interictal connectivity is a biomarker for true seizure-spread dynamics. An illustration of such a hypothetical network is shown in figure 3.8.

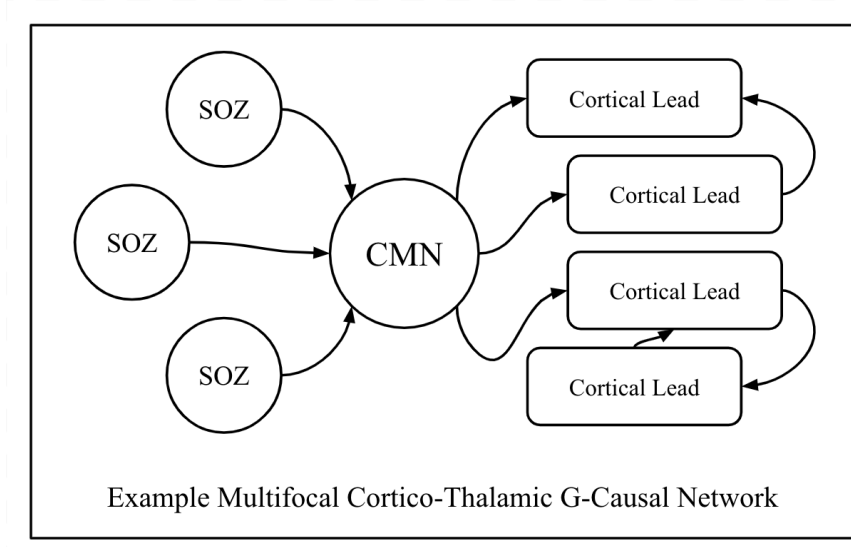


Figure 3.8: Possible interictal epileptiform network derived from conditional G-causality metrics. In this imaginary example, the CMN serves as a “hub” that spreads seizure activity from onset zones to cortical areas, which themselves have interacting dynamics. Note that there may be more than one seizure onset zone, and the CMN not-necessarily connect to *all* cortical regions.

To define conditional G-causality, consider a system of three jointly-distributed stochastic processes $\{X_t, Y_t, Z_t\}$ that are second-order stationary. X_t is said to G-cause or *drive* Y_t if the history of X_t significantly improves the prediction of Y_t compared to prediction relying only on the past of Y_t and Z_t . The conditional Granger causality from X_t to Y_t given Z_t is denoted as $\mathcal{F}_{X \rightarrow Y|Z}$, i.e. ‘conditioned’ by removing influence of Z_t . The above three-channel definition is easily generalized to higher dimensional multivariate AR(p) by

including conditioning for the additional time series.

Estimates of G-causality can be calculated both in time and frequency domains. The latter is beneficial because interactions between network nodes may occur at specific frequencies of interest. In the following sections, three approaches for G-causal estimation are described: the parametric VAR(p), a semi-parametric spline VAR(p), and non-parametric approaches. Each has benefits and drawbacks, which are compared and illustrated using simulated examples of multi-node neural networks. Several issues and concerns of G-causal estimation are brought up and characterized in the context of this project and the chosen approaches.

3.5.2 Parametric Approach

The original approach for parametric estimation of G-causality involves fitting 'full' and 'reduced' vector autoregressive models to determine conditional G-causality between all possible channel pairs [49, 50]. This approach is intuitive, but turns out to be naive due to several statistical and representation issues discussed later. For the example $\{X_t, Y_t, Z_t\}$ system, a full-model would use all three time series for prediction of Y_t . To determine if X_t drives Y_t , a reduced model without the history of X_t would be fitted and its residual errors compared with the full model's residuals using hypothesis testing

Full model:

$$\begin{aligned}
 Y_t &= a_1 Y_{t-1} + \dots + a_p Y_{t-p} + \\
 &\quad b_1 Z_{t-1} + \dots + b_p Z_{t-p} + \\
 &\quad c_1 X_{t-1} + \dots + c_p X_{t-p} + \\
 &\quad \varepsilon_t^{full} \\
 &= \sum_{\tau=1}^p A_\tau Y_{t-\tau} + \sum_{\tau=1}^p B_\tau Z_{t-\tau} + \sum_{\tau=1}^p C_\tau X_{t-\tau} + \varepsilon_t^{full},
 \end{aligned} \tag{3.28}$$

Reduced model:

$$\begin{aligned}
 Y_t &= a_1 Y_{t-1} + \dots + a_p Y_{t-p} + \\
 &\quad b_1 Z_{t-1} + \dots + b_p Z_{t-p} + \\
 &\quad \varepsilon_t^{red} \\
 &= \sum_{\tau=1}^p A_\tau Y_{t-\tau} + \sum_{\tau=1}^p B_\tau Z_{t-\tau} + \varepsilon_t^{red}.
 \end{aligned} \tag{3.29}$$

The residual errors for the full and reduced models are $\varepsilon_t^{\text{full}}$ and $\varepsilon_t^{\text{red}}$. Causality is assessed by comparing the variance of the residual errors, or the unexplained variance in Y_t from each model. The condition for G-causality is $\text{Var}(\varepsilon_t^{\text{full}}) < \text{Var}(\varepsilon_t^{\text{red}})$ and can be written as

$$\ln \left[\frac{\sigma_{\text{red}}^2}{\sigma_{\text{full}}^2} \right] > 0, \quad (3.30)$$

for $\sigma_{\text{red}}^2 = \text{Var}(\varepsilon_t^{\text{red}})$ and $\sigma_{\text{full}}^2 = \text{Var}(\varepsilon_t^{\text{full}})$. If the log-ratio is greater than zero, it means the variance of the reduced-model residuals is greater than that of the full-model. This suggests that the inclusion of the history of X_t accounts for some of the variance of Y_t (i.e. the history of X_t does add predictability), even after accounting for the contribution of other channels such as Z_t that may influence Y_t , as well as the history of Y_t itself. The test-statistic is formulated as

$$\mathcal{F}_{X \rightarrow Y|Z} \equiv \ln \frac{\text{Likelihood reduced model}}{\text{Likelihood full model}} \propto \ln \left[\frac{\sigma_{\text{red}}^2}{\sigma_{\text{full}}^2} \right]. \quad (3.31)$$

Analytical distributions for the null hypothesis (that the two residual variances are equal) of estimated time-domain conditional GC $\mathcal{F}_{X \rightarrow Y|Z}$ are known [50]. Briefly, in the case of univariate target Y , $\exp(\mathcal{F}_{X \rightarrow Y|Z}) - 1$ has an asymptotic Fisher distribution and F-tests can be used to determine statistical significance at a given significance level, typically $\alpha = 0.05$. In the case of multivariate target Y , $\mathcal{F}_{X \rightarrow Y|Z}$ scaled by the sample size has a χ^2 distribution. See [50] for details on the degrees of freedom in both cases. The estimated $\mathcal{F}_{X \rightarrow Y|Z}$ is non-negative and thus positively biased. To address bias and small sample issues, alternative tests and random permutation approaches can be used [50]. Appropriate corrections for multiple testing, using false discovery rate [62] and related approaches, are applied.

The above time domain G-causality has a corresponding spectral formulation, which allows to discern frequency-dependent directed interactions between two network nodes. The spectral representation is addressed in section 3.5, after resolving the problems introduced by the naive full vs reduced models approach, which is discussed next.

A major shortcoming of the above approach to parametric G-causality is its expensive model-fitting requirements. For an M -dimensional multivariate time series, all possible channel pairs must be fitted as reduced-models for total of $2(M^2 - M)$ regressions. For a 30-channel network, that corresponds to 1740 VAR(p) coefficient regressions, quickly growing to 19800 regressions for a 100-channel network! In addition to being computationally expensive, there are associated numerical issues. Fitting separate full and reduced models may introduce significant bias and variance into the G-causality estimates [59, 63] due to independent full and reduced model regressions. As pointed out in [59, 64] — just because a full VAR model well-approximates a multivariate time-series, does not necessarily mean that the reduced system can be well-represented by

another autoregressive model. A known order p of a full model is unlikely to be the optimal model order of the reduced model, which may theoretically require infinite model order. (Without the contribution of the removed component being included in the reduced model, a latent infinite moving average is left unexplained in the time series, biasing towards large order p for the reduced model.) In practice, a common model order is chosen for both full and reduced models. However, this can still lead to incorrect causality estimates and must be carefully considered for each G-causal analysis.

Both of these issues have been addressed by slightly different implementations involving matrix factorizations [59, 50, 65]. In particular, a parametric G-causality by Lionel Barnett and Anil K. Seth [50] fits just one full VAR model and uses spectral matrix factorizations to obtain reduced models for each channel. Both parametric and non-parametric approaches based on spectral matrix factorization are addressed in detail in section 3.5.4.

Finally, another potential concern for the parametric approach relates to model order selection and the (often) high sampling frequency of neural recordings. For example, the Nationwide Children’s SEEG recordings are sampled at 1000 Hz, and may require fitting of parametric VAR(p) models with a large number of time lags to capture history dependence. This drastically increases computation time and the required sample size to fit reasonable models. This issue has traditionally been addressed by filtering and downsampling input data [66]. However, filtering and downsampling might introduce artifacts in GC estimation. Furthermore, epileptiform recordings often contain clinically relevant high-frequency activity that would be lost through downsampling. The next-described spline AR(p) models and non-parametric approaches to G-causality help rectify this issue through other, more appropriate means.

3.5.3 G-Causality based on Spline AR(p)

An alternative solution to address the estimation of AR(p) models from data with high sampling frequency is to reduce the number of parameters to be fitted. An approach proposed by Elizabeth Spencer et al. in 2018 reduces the number of parameters while maintaining the same model order by approximating history dependencies as smooth functions [66]. Their underlying assumption is that AR coefficients change gradually between time lags, or that the temporal filters are smooth functions of time lag. In this case, approximating the AR coefficients using smooth basis functions reduces the number of parameters that must be fitted without sacrificing data. It also allows for AR model regression on smaller sample-size neural data by increasing the observed-values:parameter ratio for a fitted AR model. More observed values for each fitted parameter result in improved AR model estimation and accuracy.

Construction of a spline AR(p) model proceeds similarly to the parametric approach, except that AR

coefficients are expressed in terms of Cardinal spline basis functions. Third-degree polynomials are estimated between l control points, selected such that $l < p$. For ease of implementation, control points are evenly spaced q time-lags apart, so $l \times q = p$. A spline AR model with $l = p$ is equivalent to the parametric model. The polynomials are required to be smooth between each control point with slope regulated by a tension parameter $\tau = 0.5$, such that for control point $u_i, i \in \{1, 2, \dots, l\}$, the slope of the tangent line at u_i is given by $f'(u_i) = \tau(f(u_{i+1}) - f(u_{i-1}))$.

To derive G-causality from $X_t \rightarrow Y_y$ in the three-node system $\{X_t, Y_t, Z_t\}$, full and reduced spline AR(p) models are generated (equations 3.28, 3.29) by transforming AR coefficients for Y, Z, X from the column vectors A, B, C to $M\alpha, M\beta, M\gamma$ where M is a $p \times l$ matrix with columns corresponding to spline basis vectors:

Full model:

$$X_t = \sum_{k=1}^l M\alpha_k Y_{\{t-1-kq+q:t-1-kq\}} + \sum_{k=1}^l M\beta_k Z_{\{t-1-kq+q:t-1-kq\}} + \sum_{k=1}^l M\gamma_k X_{\{t-1-kq+q:t-1-kq\}} + \varepsilon_t^{full}, \quad (3.32)$$

Reduced model:

$$X_t = \sum_{k=1}^l M\alpha_k Y_{\{t-1-kq+q:t-1-kq\}} + \sum_{k=1}^l M\beta_k Z_{\{t-1-kq+q:t-1-kq\}} + \varepsilon_t^{red}, \quad (3.33)$$

where the time-series sub-indexing denotes a vector interval of time lags from $t - 1 - kq + q$ to $t - 1 - kq$. This notation follows the convention for full and reduced models in the parametric approach (section 3.5.2). Spencer et al.'s simpler and cleaner notation, specific to the spline-AR(p) approach, can be read in [66].

The authors chose to distribute control points evenly spaced every 5 time lags. It is possible to set unevenly spaced control points, but the model notation would change so the basis vectors would match control point increments of the original time series. The authors imposed two additional conditions: an (invisible) control point was included at $-40q$ before the zero-index point of each sample, and the slope of the basis function at the final control point $f'(u_l)$ was fixed at 0.

The benefit of the G-causality based on spline AR(p) models is its effective reduction in AR(p) model

order and parameter dimensionality. Fewer fitted parameters increases model-fitting speed and allows better fitting of data with smooth history dependence. For example, with sampling rates as high as 1000 Hz, more granular AR(p) models may overfit 'edges' due to sample noise or inter-sample variance, even if the true history dependence is smooth.

However, the spline AR(p) approach suffers from several drawbacks. Because it requires independently fitted full and reduced models to determine G-causality, it is vulnerable to the same bias-variance issues as the naive parametric approach. Furthermore, Spencer et al.'s published implementation of spline AR(p) Granger causality only allows single-trial estimates of G-causality, and I had to adapt their code to generate multi-trial estimates. Compared to the 2014 Barnett and Seth implementation of single-model parametric G-causality, the Spline approach takes much longer to compute on identical networks, as the efficiency of (effectively) reduced model order does not make up for the multitude of AR models that have to be fitted to calculate causality for all pairs of nodes in a network.

3.5.4 Parametric and Non-Parametric Approaches Based on Spectral Matrix Factorization

This section presents a solution to the problems induced by the naive GC approach based on separately fitted full and reduced parametric models. Slightly different implementations exist [59, 65, 67, 50]. Here, [67, 65, 68] are followed. Briefly, instead of fitting sets of full and reduced models, Wilson's algorithm for spectral matrix factorization [69] is used to obtain the transfer function and noise covariance matrices from the spectral matrix itself. The spectral matrix is estimated from either: a single full VAR(p) model fitted to the time series, or via non-parametric approaches based on Fourier or wavelet transforms of the time series, for example.

Below, I closely follow Dhamala et al. ([65]) and their introduction to the Wilson's spectral factorization. Depending on context, frequency is given in radians/s (ω) or in Hz (f). Matrices and block matrices are indicated by boldface symbols.

According to Wilson's method, every spectral matrix fulfilling the conditions outlined in section 3.4.2, can be factored uniquely into a set of minimum-phase functions

$$\mathbf{S} = \psi\psi^\dagger, \quad (3.34)$$

where $\psi(e^{i\theta})$ is first defined on the unit circle $|z| = 1$ as

$$\psi(e^{i\theta}) = \sum_{k=0}^{\infty} \mathbf{A}_k e^{ik\theta}, \quad (3.35)$$

with

$$\mathbf{A}_k = \frac{1}{2\pi} \int_{-\pi}^{\pi} \psi(e^{i\theta}) e^{-ik\theta} d\theta. \quad (3.36)$$

It can then be holomorphically extended to the inner unit disk ($|z| < 1$) as

$$\psi(z) = \sum_{k=0}^{\infty} \mathbf{A}_k z^k, \quad (3.37)$$

where $\psi(0) = \mathbf{A}_0$, a real, upper-triangular matrix with positive diagonal elements. Similarly, $\mathbf{S}(z)$ can be evaluated at $z = 0$. In that case, $\mathbf{H}(0) = \mathbf{I}$. Then, equations 3.23 and 3.34 imply that the (instantaneous) noise covariance matrix is

$$\Sigma = \mathbf{A}_0 \mathbf{A}_0^T. \quad (3.38)$$

Using the solution for the noise covariance matrix, and inserting $\mathbf{A}_0^{-1} \mathbf{A}_0 \mathbf{A}_0^T \mathbf{A}_0^{-T} = \mathbf{I}$ in 3.34 allows Equation 3.23 to be rewritten as

$$\begin{aligned} \mathbf{S} &= \psi \psi^\dagger \\ &= \psi \mathbf{A}_0^{-1} \mathbf{A}_0 \mathbf{A}_0^T \mathbf{A}_0^{-T} \psi^\dagger \\ &= \psi \mathbf{A}_0^{-1} \times \mathbf{A}_0 \mathbf{A}_0^T \times \mathbf{A}_0^{-T} \psi^\dagger \\ &= \mathbf{H} \times \Sigma \times \mathbf{H}^\dagger. \end{aligned} \quad (3.39)$$

Using the solution for the noise covariance matrix allows the identification of the corresponding terms for the transfer function: $\mathbf{H}(\omega) = \psi \mathbf{A}_0^{-1}$ and $\mathbf{H}^\dagger(\omega) = \mathbf{A}_0^{-T} \psi^\dagger$.

The actual computation of spectral conditional Granger causality based on factorizations of the spectral matrix, obtained either via parametric or non-parametric methods, is described here, following the exposition by Wen et al. in [67].

Consider $\mathcal{F}_{i \rightarrow j|k}(\omega)$, the spectral Granger causality from channel j to i , conditioned on a single or multiple channels denoted by k (i.e. k indicates a set with a single or multiple channels), given the corresponding spectral matrix estimated from data either via parametric AR(p) models or via non-parametric methods,

$$\mathbf{S}(\omega) = \begin{bmatrix} S_{ii}(\omega) & S_{ij}(\omega) & \mathbf{S}_{ik}(\omega) \\ S_{ji}(\omega) & S_{jj}(\omega) & \mathbf{S}_{jk}(\omega) \\ \mathbf{S}_{ki}(\omega) & \mathbf{S}_{kj}(\omega) & \mathbf{S}_{kk}(\omega) \end{bmatrix}, \quad (3.40)$$

The entries of \mathbf{S} related to k may be either a single element (single channel) or a matrix block (multiple channels).

If the above was estimated based on a parametric AR(p), then the transfer function and noise covariance matrix for the full model are already available (since \mathbf{S} was built from them in this case.) If \mathbf{S} was obtained via a non-parametric approach, apply the spectral matrix factorization as described above to obtain the transfer function and covariance matrix that satisfy

$$\mathbf{S}(\omega) = \mathbf{H}(\omega) \boldsymbol{\Sigma} \mathbf{H}(\omega)^\dagger. \quad (3.41)$$

Next, consider another spectral matrix, this time related to the reduced model, i.e. without the entries related to channel j

$$\bar{\mathbf{S}}(\omega) = \begin{bmatrix} S_{ii}(\omega) & \mathbf{S}_{ik}(\omega) \\ \mathbf{S}_{ki}(\omega) & \mathbf{S}_{kk}(\omega) \end{bmatrix}. \quad (3.42)$$

The corresponding transfer function and noise covariance matrix of this reduced model can be obtained by applying the spectral matrix factorization

$$\bar{\mathbf{S}}(\omega) = \mathbf{G}(\omega) \boldsymbol{\Omega} \mathbf{G}(\omega)^\dagger, \quad (3.43)$$

such that $\mathbf{G}(\omega)$ is the transfer function

$$\mathbf{G}(\omega) = \begin{bmatrix} G_{ii}(\omega) & \mathbf{G}_{ik}(\omega) \\ \mathbf{G}_{ki}(\omega) & \mathbf{G}_{kk}(\omega) \end{bmatrix}, \quad (3.44)$$

and $\boldsymbol{\Omega}$ is the noise covariance matrix of the reduced model.

An additional step is required to remove from $\mathcal{F}_{i \rightarrow j|k}$ the contribution of instantaneous correlations induced by common noise inputs (for details see [57].) This is achieved by the following matrix transformations of the full and reduced model quantities, respectively,

$$\begin{aligned}\tilde{\mathbf{H}}(\omega) &= \mathbf{H}(\omega) \cdot \mathbf{P}_1^{-1} \\ \tilde{\boldsymbol{\Sigma}} &= \mathbf{P}_1 \cdot \boldsymbol{\Sigma} \cdot \mathbf{P}_1^T,\end{aligned}\tag{3.45}$$

and

$$\begin{aligned}\tilde{\mathbf{G}}(\omega) &= \mathbf{G}(\omega) \cdot \mathbf{P}_2^{-1} \\ \tilde{\boldsymbol{\Omega}} &= \mathbf{P}_2 \cdot \boldsymbol{\Omega} \cdot \mathbf{P}_2^T.\end{aligned}\tag{3.46}$$

The transformation matrices are given by

$$\mathbf{P}_1 = \begin{bmatrix} 1 & 0 & \mathbf{0} \\ -\Sigma_{ji}/\Sigma_{ii} & 1 & \mathbf{0} \\ -\boldsymbol{\Sigma}_{ki}/\Sigma_{ii} & \mathbf{0} & \mathbf{I} \end{bmatrix} \begin{bmatrix} 1 & 0 & \mathbf{0} \\ 0 & 1 & \mathbf{0} \\ \mathbf{0} & \mathbf{C} & \mathbf{I} \end{bmatrix},\tag{3.47}$$

where

$$\mathbf{C} = -(\boldsymbol{\Sigma}_{kj} - \boldsymbol{\Sigma}_{ki}\boldsymbol{\Sigma}_{ij}/\Sigma_{ii})/(\Sigma_{ij} - \Sigma_{ji}\Sigma_{ij}/\Sigma_{ii}),$$

and

$$\mathbf{P}_2 = \begin{bmatrix} 1 & \mathbf{0} \\ -\boldsymbol{\Omega}_{ki}/\Omega_{ii} & \mathbf{I} \end{bmatrix}.\tag{3.48}$$

Finally, the spectral conditional Granger causality is given by

$$\mathcal{F}_{j \rightarrow i|k}(\omega) = \ln \frac{\Omega_{ii}}{Q_{ii}(\omega) \Sigma_{ii} Q_{ii}^\dagger(\omega)},\tag{3.49}$$

where the matrix $\mathbf{Q}(\omega)$ is defined as

$$\mathbf{Q}(\omega) = \begin{bmatrix} Q_{ii}(\omega) & Q_{ij}(\omega) & \mathbf{Q}_{ik}(\omega) \\ Q_{ji}(\omega) & Q_{jj}(\omega) & \mathbf{Q}_{jk}(\omega) \\ \mathbf{Q}_{ki}(\omega) & \mathbf{Q}_{kj}(\omega) & \mathbf{Q}_{kk}(\omega) \end{bmatrix} = \begin{bmatrix} \tilde{G}_{ii}(\omega) & 0 & \mathbf{Q}_{ik}(\omega) \\ 0 & 1 & \mathbf{0} \\ \tilde{\mathbf{G}}_{ki}(\omega) & \mathbf{0} & \tilde{\mathbf{G}}_{kk}(\omega) \end{bmatrix}^{-1} \begin{bmatrix} \tilde{H}_{ii}(\omega) & \tilde{H}_{ij}(\omega) & \tilde{\mathbf{H}}_{ik}(\omega) \\ \tilde{H}_{ji}(\omega) & \tilde{H}_{jj}(\omega) & \tilde{\mathbf{H}}_{jk}(\omega) \\ \tilde{\mathbf{H}}_{ki}(\omega) & \tilde{\mathbf{H}}_{kj}(\omega) & \tilde{\mathbf{H}}_{kk}(\omega) \end{bmatrix}.\tag{3.50}$$

As stated earlier, the above defined spectral Granger causality is nonnegative. Furthermore, no known analytical forms are known for the sample distribution of $\mathcal{F}_{j \rightarrow i|k}(\omega)$ under the null hypothesis. Random resampling methods are commonly used to assess whether $\mathcal{F}_{j \rightarrow i|k}(\omega) > 0$ with appropriate corrections for

multiple testing. The corresponding time-domain pairwise and conditional G-causality (\mathcal{F}_{TD}) can be obtained from the estimated spectral domain (\mathcal{F}_{FD}) quantities by the following transformation (frequency in Hz):

$$\mathcal{F}_{\text{TD}} = \frac{2}{f_s} \int_0^{f_s/2} \mathcal{F}_{\text{FD}}(f) df, \quad (3.51)$$

where $\frac{f_s}{2}$ is half the time-series sampling frequency or *Nyquist* frequency, the highest frequency that can be reconstructed from spectral estimators according to the Nyquist-Shannon sampling theorem [70]. The above equation is also used in other approaches, e.g. [50]) to check the consistency of estimated time and spectral domain Granger causality.

The great advantage of the non-parametric approach to G-causality is that it avoids all issues of AR(p) model based approaches, including coefficient estimation, model-order selection, and high sampling frequency. However, although Dhamala's method is 'non-parametric' through its non-dependence on AR models, it still requires some important choices and parameter setting related to initial time-frequency decomposition of time-series, whether with the multitaper or wavelet approach.

3.5.5 Comparison of Approaches

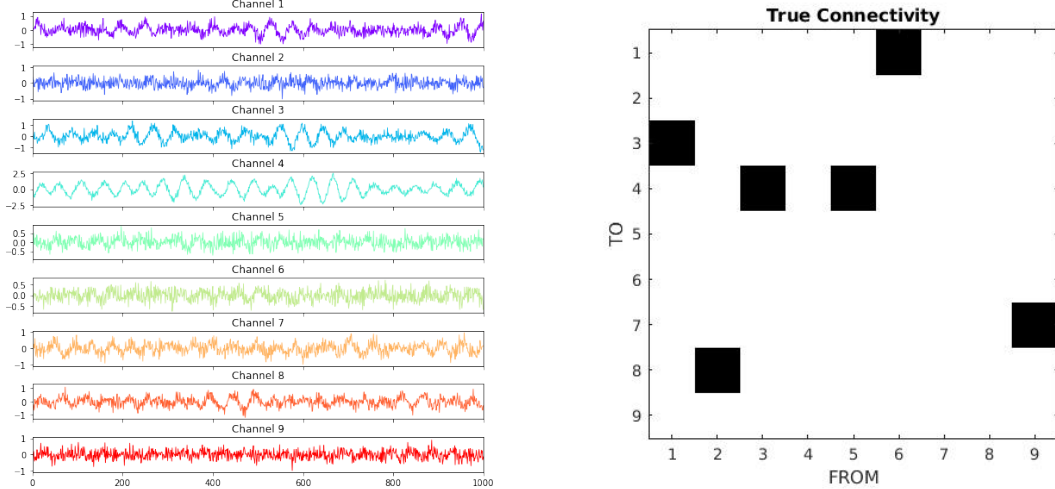


Figure 3.9: Realization of AR(30) process (left; arbitrary units for amplitudes; time in seconds) and true connectivity (right; black indicates a directed connection).

A nine-node interacting system implemented by Spencer et al. [66] is used to demonstrate the three methods for Granger Causality estimation shown here. The model is configured as a VAR(30) process with white noise term ε_t a vector of independent Gaussian random variables having zero-mean and variance = 0.0625. An example realization for each node, as well as true network connectivity, are shown in Figure 3.9. The mesh grid of incoming-outgoing (from column to row) node relationships is a standard visualization

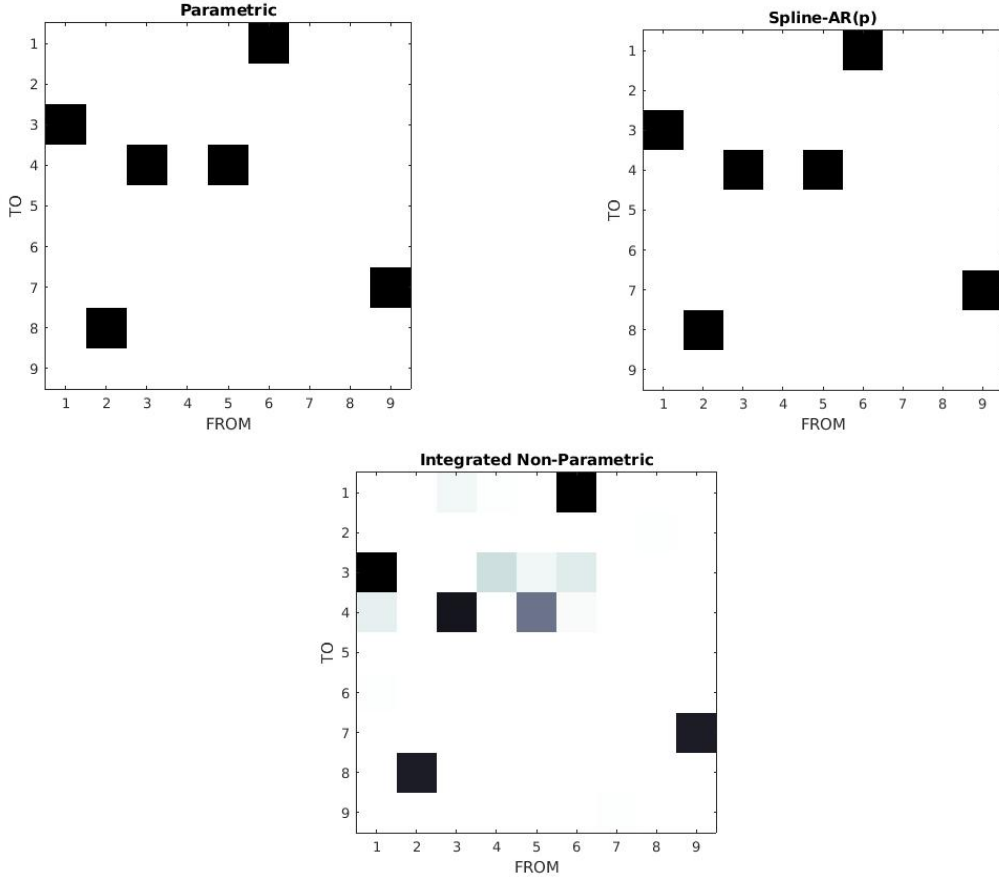


Figure 3.10: Estimated of 9-node network connectivity via the parametric (top left), spline VAR(p) (top right), and non-parametric (bottom) implementations. The parametric and spline AR(p) GC grids show statistically significant G-Causality values (via F-test at $\alpha = 0.05$). Black indicates a directed connection. The non-parametric grid shows the absolute values of integrated spectral-domain causality → time-domain G-causality. (In the non-parametric case, darker color indicates stronger GC; statistical assessment is done via random permutation approaches; not shown.)

of Granger-causal networks. Each of the three approaches — spline AR(p) using the naive full vs reduced model comparisons, parametric AR(p) and non-parametric using spectral matrix factorizations — recovered the true connectivity from $R = 200$ trials of the nine-node simulation at $f_s = 1000\text{Hz}$ and $T = 1\text{s}$ sample length. The sampling rate was the same as the real-world SEEG data used in Chapter 4 and time-length was comparable to that of observed interictal epileptiform events. Realizations were sampled by generating a noise realizations of length $T * f_s + \text{burning}$ and generating terms from $t_0 = p = 30$ by matrix multiplication of the history values and AR coefficient matrix. The 1000-sample *burnin* was included to discard the initial transients (allowing for the VAR process to “settle” into stationary dynamics). The remaining samples were kept, producing realizations of length $T * f_s = 1000$ samples.

The parametric model was fitted using code adapted from Barnett and Seth’s 2014 Multivariate Granger Causality toolbox [50]. The true model order $p = 30$ was used for this example, while the AIC and BIC

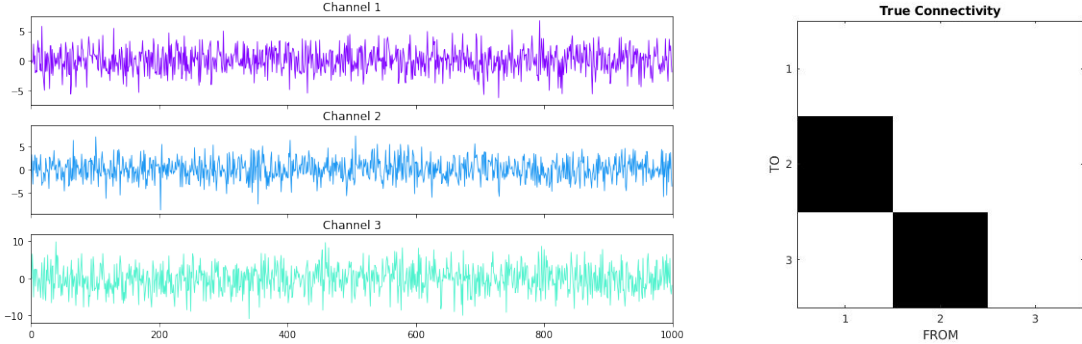


Figure 3.11: A realization from Stokes and Purdon’s 3-node AR(3) dynamical system (left; amplitudes in arbitrary units) and the corresponding true node connectivity (right; black indicates a directed connection).

estimates suggested $p = 26$ as the optimal model order. Setting model order to the predicted optimal value had no effect on the G-causal network estimate: likely, due to the shallow-tailed history dependence of in the AR(30) process, the final four lags did not significantly contribute to process dynamics. The spline AR(p) model was fitted using Spencer et al.’s code modified to accept multiple signal trials, by concatenating realizations into a common history matrix that was then used to fit a VAR model. The control points were spaced every 5 time-lags, for a total of 6 control points capturing $5 \times 6 = 30$ ms of history dependence, and the (invisible) preceding control point at -100 ms. The non-parametric model was generated using code from the non-parametric GGC toolbox by Dhamala and Pagnotta [65, 71]. The multitaper spectral estimator was used for estimating the spectral matrix and the corresponding conditional G-Causality estimates, with $F_{\max} = \frac{f_s}{2} = 500$ Hz, $F_{\text{res}} = \frac{f_s}{T*f_s} = 1$ Hz, and 4 tapers. All three approaches successfully estimated the true network connectivity given by the nine-node VAR(30) coefficient matrix. The results are summarized in Figure 3.10.

As discussed earlier in this chapter, a known issue with G-Causality estimation is the weakness of the naive parametric implementation that requires separately fitted full and reduced models [59, 50]. Patrick A. Stokes and Patrick L. Purdon describe in a 2017 study how certain model-order assumptions can spuriously affect G-causal estimation by increasing either bias or variance [63]. They implement an example 3-node AR(3) dynamical system that may evoke spurious connections when G-causality is estimated using the naive parametric implementation. This provides another example to illustrate the application of the three G-causal approaches trialed in this project. An example realization of the 3-node AR(3) and true network connectivity are provided in figure 3.11.

Barnett and Seth’s parametric and Dhamala and Pagnotta’s non-parametric approaches avoid fitting full and reduced models and are thus robust to concerns of model-order and individual model-fitting as previously discussed. Spencer et al.’s spline VAR(p) approach fits independent full and reduced models for each channel

pair using the same (spline basis) model order, so may be vulnerable to the model-fitting issues. However, the spline VAR(p) GC performs well on Stokes and Purdon's 3-node example system and recovers the true network without predicting spurious connections. It is important to note that this is far from conclusive evidence that the spline VAR(p) approach to G-causality is robust to the previously described bias and variance issues, and it is recommended that results of spline VAR(p) GC connectivity be compared with other methods, or an alternative implementation relying on single-model fitting be introduced. The time-domain results of the three G-causality approaches are displayed in Figure 3.12. The corresponding spectral domain G-causality for the parametric and non-parametric implementations are shown in Figure 3.13.

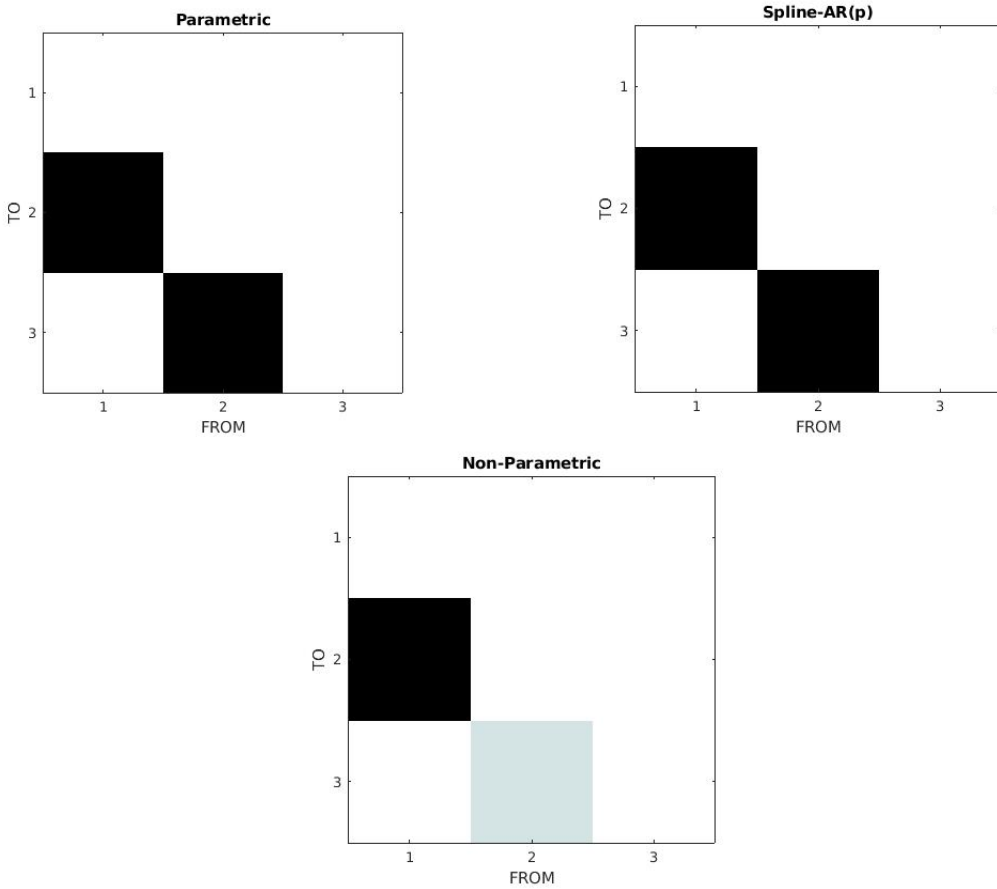


Figure 3.12: Estimated network connectivity from Stokes and Purdon's 3-node AR(3) example, via the parametric (top left), spline VAR(p) (top right), and non-parametric (bottom) implementations. The parametric and spline VAR(p) Granger networks show statistically significant G-Causality values ($\alpha = 0.05$ based on F-tests, corrected for multiple testing). The non-parametric grid shows integrated spectral-domain causality → time-domain G-causality. Statistical assessment for the non-parametric case requires bootstrapping via random permutations and is not shown.

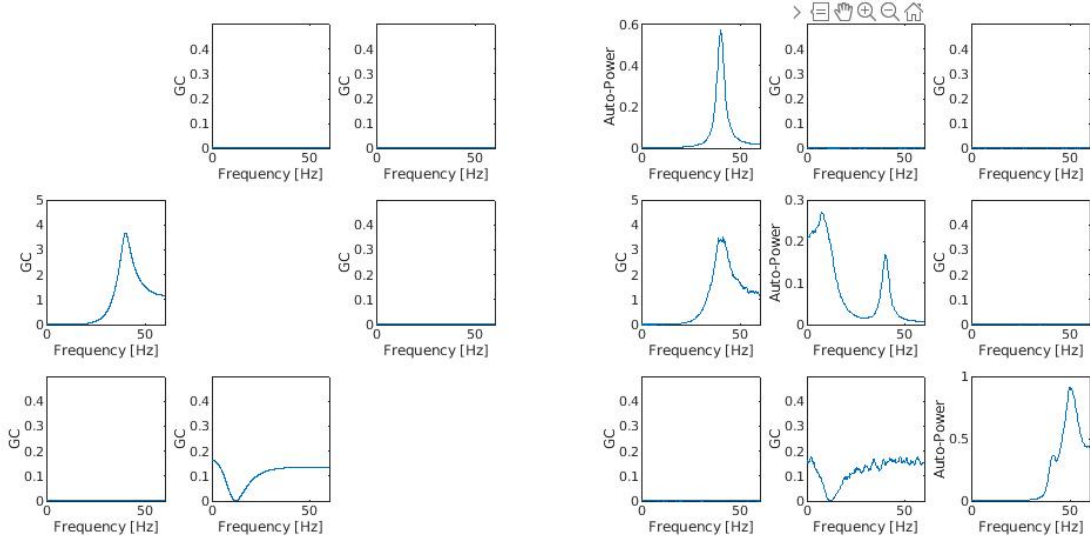


Figure 3.13: Estimated spectral domain G-causality from Stokes and Purdon’s 3-node AR(3) example, using parametric (left) and non-parametric (right) implementations. The diagonal values in the non-parametric plot are auto-power values within each channel.

3.5.6 Summary and Implementation Notes

The three variations of G-causality estimation presented here all have benefits and drawbacks. The original full- and reduced-model fitting implementation has largely been supplanted by other methods, as it is responsible for the most significant known statistical issues with G-causal time series analysis. The only method above that retains such an implementation is G-causality based on spline AR(p), and as a result great caution should be maintained if applying it for estimation of unknown directed interactions. For the SEEG dataset used in chapter 4 of this thesis, both the parametric and non-parametric approaches were applied. The parametric approach suffers from the necessity of model order selection, complicated by the high sampling rate of the SEEG data recordings. Setting parameters for the non-parametric direct spectral matrix estimator (in this case, a multi-taper short-time Fourier transform) presents difficulty considering the high sampling rate of the signal as well. Comparing connectivity estimates between more than one approach may provide improved context from which to draw conclusions. The implementations for each of the three approaches were sourced from publicly available code, and modified by either myself or members of the Truccolo Lab. The parametric implementation (using spectral factorization) is from the 2014 Matlab Toolbox “The Multivariate Granger Causality (MVGC) Toolbox” by Barnett and Seth [50], modified and compiled by the Truccolo Lab. Code for visualization of time- and spectra-domain G-Causal connectivity was modified from the MVGC Toolbox as well. The Spline AR(p) G-Causality implementation by Spencer et al. is available on github “Eden-Kramer Lab”) [66]. Their code was modified by Wilson Truccolo and

myself to allow multiple-trial G-Causality estimation. Additional code from Spencer et al. was modified for visualization of G-Causal networks. The non-parametric G-Causality implementation by Dhamala, Pagnotta et al. is available on github (“mattiapagnotta”) under the nonparametricGGC_toolbox repository [65, 71].

Chapter 4

RESULTS

4.1 Analysis of Interictal Activity

Two members of the SEEG cohort, subject 1 and subject 7, were selected for network analysis and demonstration of the proposed framework. Neurologists classified subject 1 as having rapid/synchronous CMN involvement during seizures while subject 7 lacked CMN involvement in seizures. These two subjects represent a comparison group between neurologist-determined CMN involved and non-involved seizure patterns. I aimed to study differences between these two subjects in CMN and non-CMN directed interaction networks. Eventually, larger samples for each group may be correlated with functional connectivity estimates using G-Causality metrics, for potential application to clinical decision-making. As stated earlier, the research data analyzed in this thesis was collected under an IRB approved protocol at Nationwide Children’s Hospital. A data sharing agreement between Nationwide Children’s Hospital (Shaikhouni Lab) and Brown University (Truccolo Lab) supports the research in this thesis and related ongoing research in the Truccolo Lab.

Both subjects were monitored with implanted SEEG electrodes as described in section 2.3. Depth electrode trajectories were interspersed throughout the bilateral CMN, sub-thalamic structures, as well as bilateral cortex. Neurologist and epilepsy unit staff compiled Long Term Monitoring (LTM) reports for each subject, including onset electrodes and timing of seizures as well as background and interictal epileptiform EEG activity. A thorough description of each subject and observed abnormal EEG activity is provided in section 4.2, along with notes on the SEEG recordings as well as challenges encountered during data pre-processing.

Long (multi-hour) interictal recordings were obtained for both subjects. Segmentation of interictal epileptiform events was carried out manually using a programmed graphical user interface containing both time- and frequency-domain data, generated using spectral decomposition methods described in section 3.3. The process is described in section 4.3. Datasets of comparable interictal epileptiform events, specifically 5-10 Hz transient oscillations, identified from both subjects were compiled for use in estimation of functional

connectivity.

The parametric and non-parametric implementations of G-causality (section 3.5) was used to detect statistical time-causal relationships and elucidate interictal network structure from the compiled datasets. For preliminary analysis, a subset of electrodes corresponding to CMN, subcortex, cortex, and any neurologist-determined SOZ regions were selected. Time and spectral domain directed interactions between selected areas, particularly from SOZ → CMN and CMN → cortex were noted and compared with each subject’s clinical designation. Section 4.4 concerns the network analysis, including issues with implementation and execution.

4.2 Subject Selection and Data Pre-Processing

I selected subjects 1 and 7 for preliminary interictal network analysis because of their opposite CMN involvement classification, and hypothesized they would exhibit distinct interictal connectivity patterns. Specifically, subject 1 is expected to exhibit significant CMN involvement during propagation of interictal epileptiform activity, while subject 7 is not. This analysis is only preliminary so any supporting or opposing evidence found may not be used to make a conclusion about CMN-seizure dynamics without significantly expanded analysis. LTM reports of both subjects were used to identify prospective regions of interictal activity as well as the expected variant of interictal epileptiform events present in each subject’s SEEG recordings. Although the two subjects’ were implanted with different electrode schemes, both included a many named sub-cortical targets as well as the left and right CMNs. Subject-specific SOZ electrodes were identified from the LTM reports for inclusion in the analysis. Clinician descriptions of subjects 1 and 7 are provided at the end of section 2.3. Relevant information from their LTM reports is summarized below.

Each of the 12 (subject 1) or 14 (subject 7) electrode trajectories had multiple recording contacts across different depths in addition to the designated electrode targets (listed below for each subject). These additional contacts may have been in gray- or white-matter tissue. Contacts in white-matter (myelinated axonal fibers) were manually identified by their characteristic EEG trances (massive amplitude, lack of correlation with grey-matter electrodes) and not included in the analysis.

4.2.1 Subject 1

Subject 1 is a 19 year old male without prior surgery who suffered from bilateral onset seizures of unknown etiology. He was monitored for 10 days following SEEG implantation, and suffered one habitual and one stimulated seizure during monitoring. The habitual seizure involved near-synchronous CMN involvement and difficult-to-lateralize onset from bursts of epileptiform activity in the right anterior insula, left anterior middle

singulate, as well as the right CMN. Following SEEG monitoring, neurologists recommended treatment by DBS of the CMN. Insurance denied the request for DBS, so the subject received RNS of the CMN instead.

Background EEG activity for subject 1 involved transients of 3 Hz delta and 4-6 Hz theta activity with maximum amplitudes ranging in 200-500 μ V, as well as lower-amplitude gamma activity. Abnormal interictal epileptiform activity was observed during each day of monitoring. The most common observation was of isolated 500-800 μ V spikes and spike-wave complexes lasting between 0.5 and 1 seconds. Spikes, poly-spikes, and spike-wave complexes were observed in a number of electrodes including cortical, sub-cortical, and CMN contacts. The left and right CMN contacts also developed transients of 5-6 Hz sharp waves associated with evolving epileptiform activity. The observed epileptiform activity was noted to not lateralize consistently.

Subject 1 was implanted with a total of 12 depth electrodes, with targets in the following brain structures:

- Left Centromedian Thalamic Nucleus (LCMN)
- Right Centromedian Thalamic Nucleus (RCMN)
- Left Hippocampal Head (LHH)
- Right Hippocampal Head (RHH)
- Left Anterior Middle Cingulate (LAMC)
- Right Anterior Middle Cingulate (RAMC)
- Left Posterior Middle Cingulate (LPMC)
- Right Posterior Middle Cingulate (RPMC)
- Left Anterior Insula (LAI)
- Right Anterior Insula (RAI)
- Right Pars Triangularis (RPT)
- Right Supplementary Motor Area (SMA)

4.2.2 Subject 7

Subject 7 is a 7 year old female without prior surgery who has a KCNT1 potassium channel mutation. She experienced frequent, multifocal seizures with bilateral onset. She was monitored for 7 days, during which she experienced a total of 19 habitual electroclinical seizures, most of which were brief gestural motor seizures out of sleep. 11 seizures began in the left medial frontal region and spread rapidly to right medial frontal

contacts, but other onset zones included left medial temporal, right medial temporal, right part triangularis, left temporal pole, and bilateral medial temporal electrodes. One hemiclonic of diffuse onset was observed, evolving from left temporal pole contacts with rapid spread to left hemisphere electrodes.

The KCNT1 gene is involved in the synthesis of potassium ion channels [72]. Potassium channels are highly present in neurons and serve to regulate membrane potential by transporting positively charged K⁺ ions into and out of neurons [73]. As membrane potential is directly related to neuronal excitation and firing, ion channel mutations frequently result in severe, difficult-to-treat epilepsy syndromes that arise in infancy or childhood [14]. Clinical manifestations of KCNT1 epilepsy include frequent migrating multifocal seizures refractory to medication, as well as diffuse multifocal bilateral migrating epileptiform activity such as interictal discharges [74]. For this subject, the KCNT1 mutation likely contributed to the diversity of interictal activity observed in their SEEG recordings as well as the relative frequency of seizures compared to subject 1 and others in the SEEG cohort.

Background EEG activity included 50-250 μ V theta (6-7 Hz) and alpha (8-11 Hz) transient oscillations with superimposed beta activity, while the subject was awake. Higher frequency coordinate activity was observed in the left medial temporal gyrus/amygdala (LAM) and left superior temporal gyrus/temporal pole (LTPL) contacts. Increased delta and theta frequency activity was observed during drowsiness, and delta sleep-spindles during sleep. Focal slowing of background EEG activity consistent with regional cerebral dysfunction was observed in LAM and LTPL electrodes. Interictal transient epileptiform activity was present during all 7 days of monitoring, and primarily included multifocal spike populations with predominance in the LAM and LSTG contacts, with additional bilateral discharges observed in both hemispheres. Spike and poly-spike and wave complex events of 200-600 μ V amplitude were frequently present in the left temporal pole electrode with polymorphic 1-2 Hz delta and 7-9 Hz alpha slowing transients in deeper LTPL contacts. High amplitude diffuse bilateral spike and wave bursts at 4 Hz occurred in both hemispheres with shifting lateral predominance. The left CMN exhibited lower amplitude (100-200 μ V) spikes and spike-wave complexes. High amplitude (up to 1 mV) spikes were observed in left medial temporal gyrus/hippocampal (LMTG) body contacts and were frequently involved in a network consisting of LTPL, LAM, and LMTG electrodes.

Subject 7 was implanted with a total of 14 depth electrodes, with targets in the following brain structures:

- Left Centromedian Thalamic Nucleus (LCMN)
- Right Centromedian Thalamic Nucleus (RCMN)
- Left Pars Triangularis (RPT)
- Right Pars Triangularis (RPT)

- Left Pars Orbitalis-Mes Orbitofrontal Cortex (LOF)
- Right Part Orbitalis-Mes Orbitofrontal Cortex (ROF)
- Left Medial Frontal Gyrus-Anterior Cingulate (LMFG)
- Right Medial Frontal Gyrus-Anterior Cingulate (RMFG)
- Left Superior Frontal Gyrus-Dorsal Anterior Cingulate (LSFG)
- Left Superior Marginal Gyrus-Posterior Insula (LSMG)
- Left Superior Temporal Gyrus-Temporal Pole (LTPL)
- Left Medial Temporal Gyrus-Amygdala (LAM)
- Left Medial Temporal Gyrus-Hippocampal Body (LMTG)
- Right Medial Temporal Gyrus-Hippocampal Head (RMTG)

4.2.3 Electrode Selection

Electrode selection for inclusion in G-Causal analysis of interictal events is complicated by differences in subjects' electrode implantation schemes. No two subjects are alike, nor their brain or skull shape and size. The surgical robot software aligns intra-operative CT scans with prior MRI images to accurately guide electrodes to desired anatomical targets. However, it is up to attending physicians to revolve any issues raised by the average-brain normalization process. Identical electrode implantation schemes are unlikely to be compatible between two subjects. For example, if an electrode trajectory is deemed (by the attending neurologist or neurosurgeon) to pass too close to a vital or eloquent brain structure, its path must be re-routed to avoid the structure. As a result, electrodes with deep contacts in the same brain structure may be implanted along unique trajectories in two different subjects.

Subjects 1 and 7 share several common contacts and similar electrode targets. Since their SEEG studies' primary aim was to determine CMN involvement, both subjects were implanted with left and right CMN electrodes. For the purposes of this project, these electrodes are included by default in the G-causal network analysis. All other sub-cortical EEG leads (the deepest contacts in all electrodes) are included in the analysis for each subject as well. Since sub-cortical structures possess incredibly specific roles in neural organization and the brain hierarchy, they remain important hypothetical network nodes.

Additional contacts for each subject were selected according to neurologist and epilepsy unit observations in the LTM reports. Besides sub-cortical structures, several bilateral cortical electrodes were included in the

analysis to serve as indicators of seizure generalization or spread to the cortex. For each subject, I selected at least 5 cortical electrodes which were specifically mentioned in the LTM report as participating in epileptiform activity, either as a seizure onset zone, an area with observed interictal epileptiform activity, or an area to which a seizure generalized. Tables (4.1, 4.2) of the selected electrodes for each subject, with brief notes on inclusion criteria, are provided below.

Table 4.1: Selected Electrodes for Subject 1

| Electrode Contact | Organization Level | Rationale |
|-------------------|--------------------|--------------------------------------|
| LCMN2-1 | CMN | Potential DBS/RNS target |
| RCMN2-1 | CMN | Potential DBS/RNS target |
| RAMC3-2 | Sub-Cortex | LTM implicated epileptiform activity |
| RPT2-1 | Sub-Cortex | LTM implicated epileptiform activity |
| LAI2-1 | Sub-Cortex | LTM implicated epileptiform activity |
| RAI2-1 | Sub-Cortex | LTM implicated epileptiform activity |
| RSMA2-1 | Sub-Cortex | LTM implicated epileptiform activity |
| RPMC2-1 | Sub-Cortex | Other sub-cortical channel |
| LPMC2-1 | Sub-Cortex | Other sub-cortical channel |
| LAMC2-1 | Sub-Cortex | Other sub-cortical channel |
| RHH3-2 | Sub-Cortex | Other sub-cortical channel |
| LHH3-2 | Sub-Cortex | Other sub-cortical channel |
| RAI12-11 | Cortex | LTM implicated epileptiform activity |
| LAMC15-14 | Cortex | LTM implicated epileptiform activity |
| LHH13-12 | Cortex | LTM implicated epileptiform activity |
| LAI12-11 | Cortex | LTM implicated epileptiform activity |
| RAMC11-10 | Cortex | LTM implicated epileptiform activity |
| LCMN13-12 | Cortex | LTM implicated epileptiform activity |
| RCMN12-11 | Cortex | LTM implicated epileptiform activity |

4.2.4 Referencing Scheme

Depth electrodes measure differences in extracellular electric potentials (on the order of microvolts). The potential difference is calculated by comparison with a reference contact selected from the implanted electrodes; the signal measured by the other contacts is the difference in electric potential across the two electrodes. Consequentially, every channel's signal is linearly dependent upon the varying electric charge of the reference electrode. This leads to spurious correlations and false connectivity estimated between time series with no direct time-causal relationship. Analysis of G-causal interactions during interictal activity using commonly-referenced electrodes generated spurious bi-directional G-causality between *every* channel pair.

To address this issue, a bipolar (nearest-neighbor) referencing scheme was used for signal analysis, in both the segmentation and network analysis steps. A bipolar montage is generated by subtracting the values of one electrode contact from an adjacent contact's recording. As a result, the common reference artifact is no longer present in the bipolar re-referenced signal. Furthermore, power-line noise from the recording

Table 4.2: Selected Electrodes for Subject 7

| Electrode Contact | Organization Level | Rationale |
|-------------------|--------------------|--------------------------------------|
| LCMN2-1 | CMN | Potential DBS/RNS target |
| RCMN2-1 | CMN | Potential DBS/RNS target |
| LTPL2-1 | Sub-Cortex | LTM implicated epileptiform activity |
| LAM2-1 | Sub-Cortex | LTM implicated epileptiform activity |
| LMFG-1 | Sub-Cortex | LTM implicated epileptiform activity |
| LSFG2-1 | Sub-Cortex | Other sub-cortical channel |
| LOF2-1 | Sub-Cortex | Other sub-cortical channel |
| LPT2-1 | Sub-Cortex | Other sub-cortical channel |
| LSMG2-1 | Sub-Cortex | Other sub-cortical channel |
| LMTG2-1 | Sub-Cortex | Other sub-cortical channel |
| RMFG2-1 | Sub-Cortex | Other sub-cortical channel |
| ROF2-1 | Sub-Cortex | Other sub-cortical channel |
| RPT2-1 | Sub-Cortex | Other sub-cortical channel |
| RMTG2-1 | Sub-Cortex | Other sub-cortical channel |
| RPT9-8 | Cortex | LTM implicated epileptiform activity |
| LCMN14-13 | Cortex | LTM implicated epileptiform activity |
| RMTG11-10 | Cortex | LTM implicated epileptiform activity |
| LTPL10-9 | Cortex | LTM implicated epileptiform activity |
| LMFG14-13 | Cortex | LTM implicated epileptiform activity |

equipment (constant signal or hum at integer multiples of the AC power-line frequency — 60 Hz) is removed by the bipolar montage. The bipolar scheme was used due to ease of implementation and to conform with the clinical observation and LTM reports, where neurologists and epilepsy unit staff monitored each patient using bipolar montages of electrode pairs. There are other suitable referencing schemes available for multi-channel EEG data, discussed further in chapter 5.

4.2.5 Other Data Considerations

SEEG recordings were de-identified and transferred in European Data Format (EDF) from Nationwide Children’s Hospital to the Truccolo Lab pursuant to the previously mentioned IRB protocol and data-use agreement. EDFBrowser and PyEDFlib were used for preliminary visualization of the EDF files and their import to Python for analysis, respectively. At each step, data was adjusted to have zero-mean by subtracting the mean value across all time steps from corresponding channels. Several recording channels contained high amplitude deviating electric potentials with increased noise compared to the majority of contacts. These were contacts with electrode trajectories passing through white matter and, as stated earlier, they were removed from consideration.

4.3 Segmentation Process

Following the required pre-processing steps, data were loaded into Python using pyEDFlib and annotated to compile a dataset of comparable interictal events for each subject. A review of the LTM report for each subject allowed me to identify electrodes when interictal abnormal epileptiform activity occurred, as described in the previous section. Visual analysis in the time and frequency domains revealed frequent 5-10 Hz transient oscillations, or bursts of wave like activity with definite frequency signature, ranging from approximately 0.5-second to about 5-second duration for the longest individual events. I chose these interictal events for the preliminary analysis carried out in this thesis.

I developed a graphical user interface for visualization and annotation of interictal events, shown in Figure 4.1. It includes both time and frequency domain signals, with buttons for navigation and addition/deletion of new annotations. The time domain signal was a bipolar montage of a selected electrode pair. The frequency domain signal (from 1-40 Hz at 0.5 Hz resolution) was generated using a superlet transform of order 15 with 7 cycles per wavelet and appropriate zero-padding to remove edge effects. Spectrum color intensity (with red corresponding to more power and blue corresponding to less power in a given frequency band) was standardized for a given SEEG montage. That is, spectrum intensity was comparable within the same electrode set, but not between subjects.

The identification and segmentation of 5-10 Hz oscillatory transient events proceeded similarly for both subjects. First, an EDF file containing SEEG recordings during non-seizure (interictal) and non-sleep periods was chosen as the source dataset for each subject. Depth electrode contacts corresponding to interictal activity were selected as “segmentation electrodes” to be the source of timestamp annotations: RAI12-11 was selected for subject 1 and LAM2-1 selected for subject 7. Signals from both electrode contacts were processed into a bipolar montage (i.e. RAI12-11 signifies that the EEG signal amplitude of RAI11 was subtracted from the amplitude of RAI12 for each time t in the EDF file) and global signal mean subtracted. Using the annotation GUI, I navigated through the signal montage, visually identifying individual epileptiform events matching the oscillatory time signature and 5-10 Hz frequency signature. Each event was annotated using the interface, whereupon a row entry was added to a matrix of annotations with columns corresponding to event length (L), event start point t_{start} (relative to the start of the EDF file), and event end point t_{end} . Examples of various 5-10 Hz oscillatory transients identified during this process, in both the time and frequency domains, are shown in Figure 4.2.

After a matrix of annotated events was compiled for the given signal montage, a python script was used to segment out the SEEG signal for each channel to be included in the analysis. Although an ideal connectivity

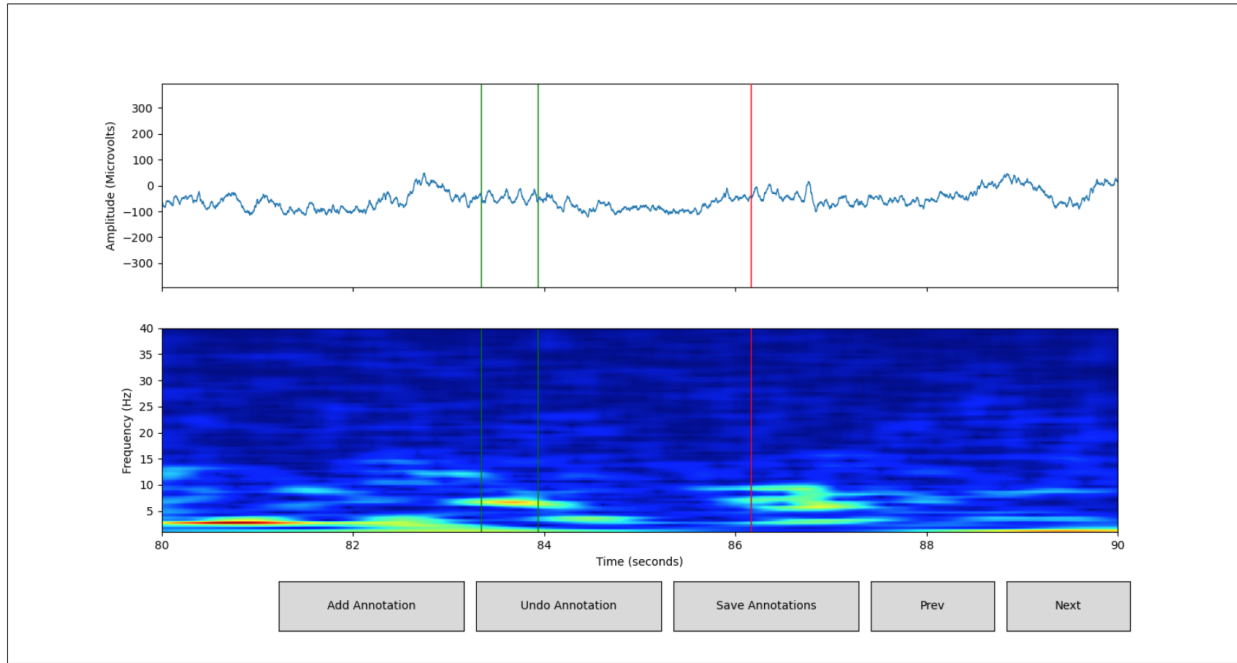


Figure 4.1: Annotation GUI showing (Subject 7) EEG data from a bipolar montage of a selected electrode contact (LTPL2-1). Data is displayed in both time (top) and frequency (bottom) domains. The vertical red line indicates current cursor position, while the green lines denote the start and end of the most recent annotation. The x-scale is time relative to EDF file start in seconds, with 10 seconds shown per window. The y-scales are in μ V and Hz for the time and frequency domain signals, respectively. The buttons allow addition, removal, and saving of annotations. The next and previous buttons shift the time window by 5 seconds forward or backward. This was chosen in anticipation of some events of interest becoming split between 10 second signal increments.

analysis would allow for size (time length) differences between multiple trials of interictal epileptiform events, current G-causality algorithm implementations require a standardized trial length. As a result, all annotations corresponding to events lasting less than 1 second ($L < 1$) were discarded. A 1-second signal sample for a bipolar montage of each electrode contact included in the analysis was then segmented, from the starting time $t = t_{\text{start}}$ in the “segmentation electrode” until $t = t_{\text{start}} + 1$. Each segmented epileptiform event, consisting of a 1-second recording across 19 channels for subject 1 and 19 channels for subject 7, was then “zero-mean’d” (mean-subtracted) in each channel. It is important to note that the “segmentation electrode” determined both the start and end time for *every* channel segment included in the analysis. The absolute time within the SEEG recording was constant for all 19 channels in each segmented event, and events were not shifted or otherwise aligned according to any visible delay between different channels. It was critical that segmented events remained on an absolute time scale to ensure robust analysis of time-causal interactions among all 19 channels for each subject. To clarify the procedure, a graphic outlining the process of identification, segmentation, and data processing is provided in Figure 4.3. The final datasets of 5-10 Hz oscillatory transient events used for preliminary analysis consisted of 181 and 157 1-second segments across the 19 selected channels for subject 1

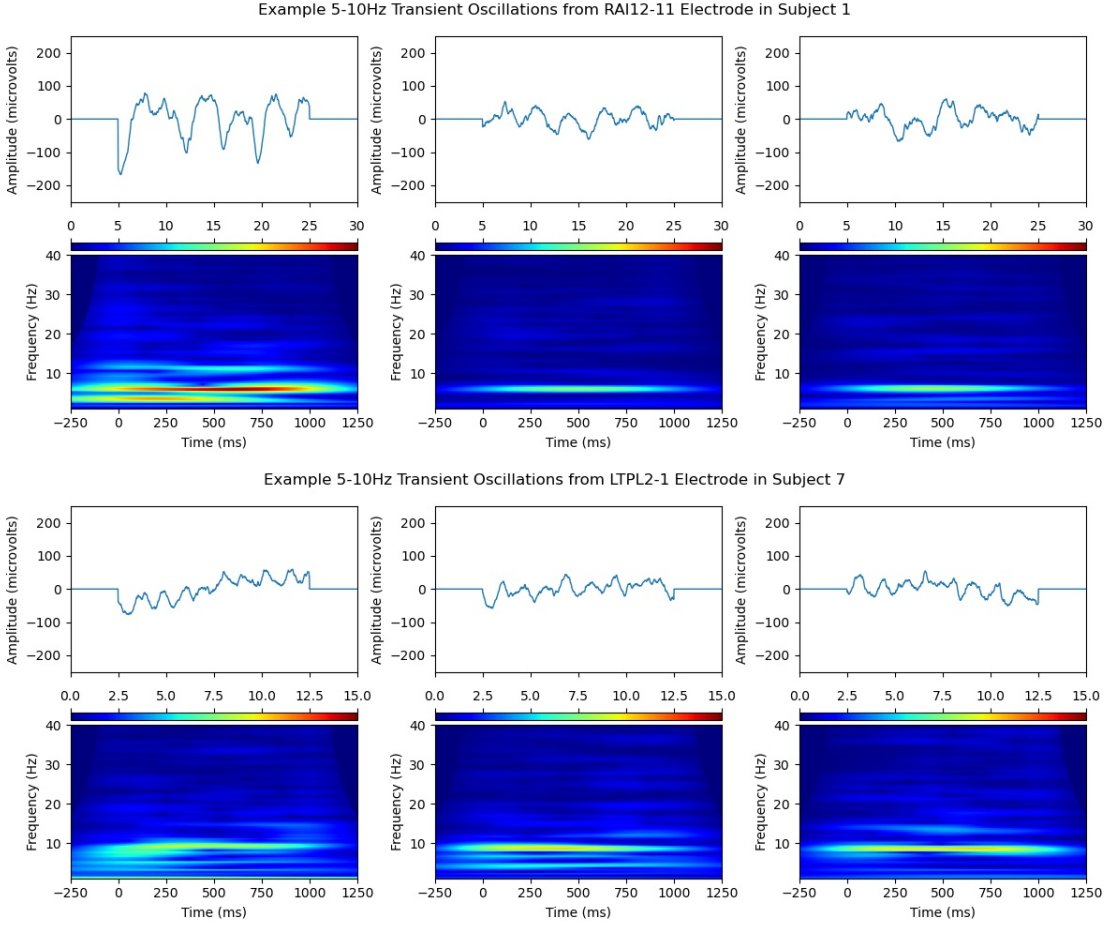


Figure 4.2: Example 5-10Hz oscillatory transient events segmented from subject 1 and 7 in time (top) and frequency (bottom) domains. The segmented event is between 0 and 1000ms (1 second), zero-padded by 250ms before and after for clarity. The spectrum is generated using an order-15 multiplicative superlet with identical parameters to the annotation process.

and 7, respectively. They were exported into a “.mat” file in preparation of the G-causal network analysis, which is described in the next section.

4.4 Network Analysis

Network analysis of the two 5-10 Hz oscillatory transient datasets from subjects 1 and 7 was carried out using both Barnett and Seth’ [50] parametric and Dhamala and Pagnotta’s non-parametric [68] G-causality implementations. The goals of this preliminary analysis were to demonstrate the framework and its potential for analysis of real-world neural data. I hoped to observe some statistically significant interactions within the compiled datasets, and to describe any apparent differences between subject 1 (CMN-involved) and subject 7 (CMN-uninvolved). Analyses were performed in Matlab[®][75].

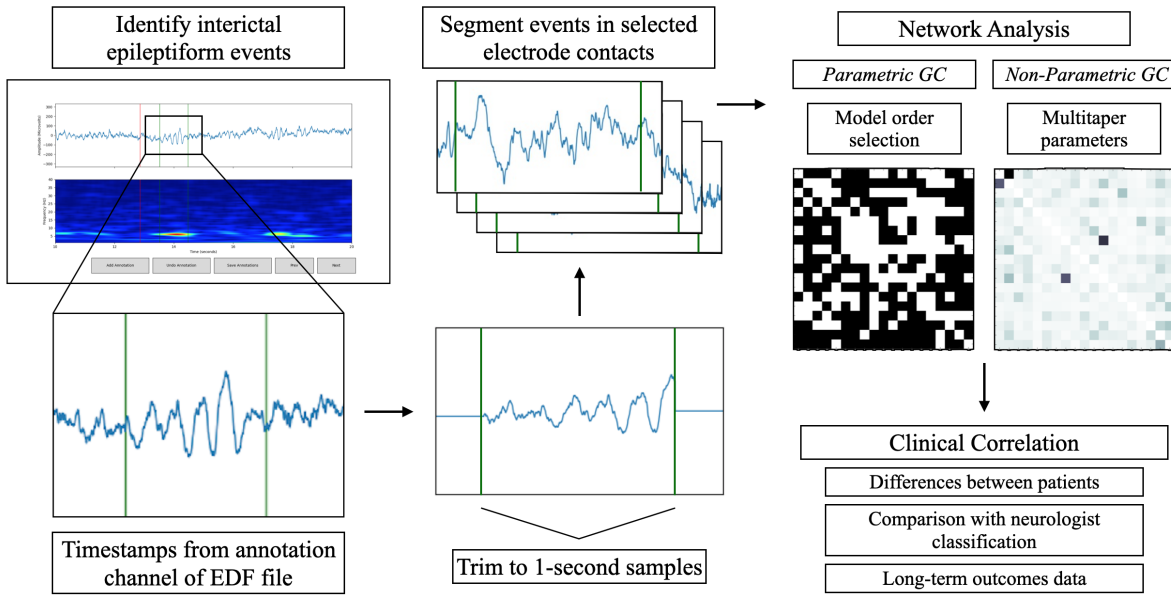


Figure 4.3: Outline of procedure for identification and analysis of interictal epileptiform events. Future work should expand to clinical correlation and treatment recommendation as appropriate.

Visualizations of estimated directed network structure are given by grid-plots where x-axis labels corresponds to source (or *driver*) brain areas and y-axis labels correspond to destination (or *driven*) areas. The bilateral CMN contacts (red) and “segmentation source” (blue) contacts are outlined in each figure. Electrode labels are arranged in the following order: (1) left CMN contact, (2) right CMN contact, (3) left sub-cortical contacts, (4) right sub-cortical contacts, (5) left cortical contacts, (6) right cortical contacts. Electrodes within the same group are displayed in alphabetical order, and within-group arrangements are independent of any structural or functional relationships between electrode positions.

The parametric G-causal network analysis was executed twice using different model orders. The first analysis used the Akaike Information Criterion (AIC) and Bayesian Information Criterion (BIC) for model order selection; both AIC and BIC agreed on an optimal model order $p = 5$. For exploratory purposes, the second analysis used a much higher model order of $p = 30$. Hypothesis testing for the time domain G-causality was carried out using F-tests at $\alpha = 0.05$ significance level, with correction for multiple testing. Spectral domain G-causality was also estimated. A resampling-based null distribution for spectral domain causality was not generated for this preliminary analysis. G-causality values and directed connectivity matrices for both subjects are plotted in Figures 4.5 and 4.4.

The non-parametric G-causal network analysis required no model order selection. Multitaper spectral estimator parameters were set as follows: bandwidth 4 Hz (7 DPSS tapers), frequency resolution 1 Hz

determined by 1-second long time segments, and a frequency range between 1-100 Hz. Spectral causality values were integrated over the frequency range for comparison with time-domain G-causality from the parametric approach. Integrated non-parametric G-causality values are plotted in Figure 4.6.

Overall, the parametric analysis revealed time-domain directed interactions during segmented 5-10 Hz transient oscillations for both subject 1 and subject 7. The non-parametric analysis showed notable G-causality values for both subjects as well. Although initial visual inspection indicates many of the time-domain integrated non-parametric causality values appeared similar to the estimated parametric case, there were also some dissimilarities. A systematic comparison is planned for future work. In addition, no spectral-domain G-causality results are presented here, but a more thorough review of frequency-domain G-causality should be conducted in subsequent analyses aiming to derive significant conclusions related to the hypothesis. Assessment of statistical significance based on random resampling, specifically random shuffling of trials

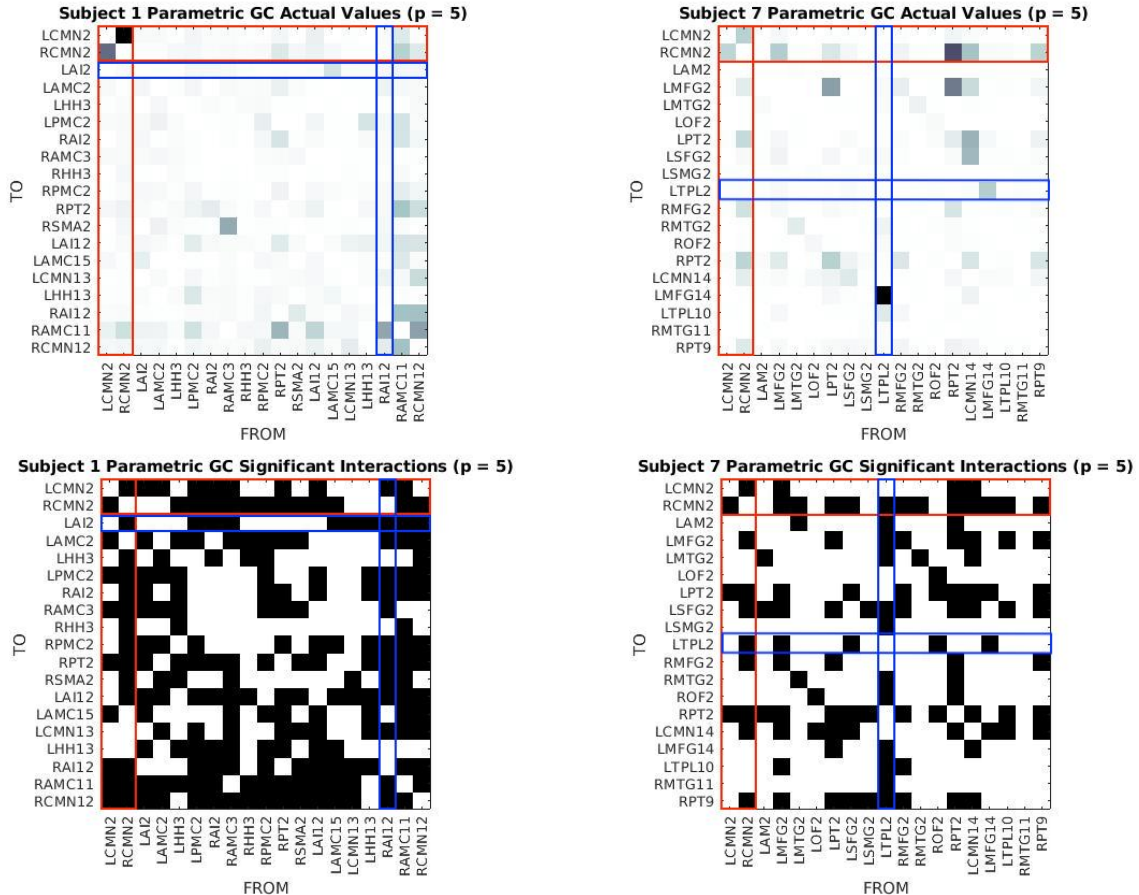


Figure 4.4: Results of parametric G-causality analysis for subject 1 (left) and subject 7 (right) using AIC/BIC selected order-5 AR(p) model. The top plots show computed values of G-causality (darker means higher causality). In the bottom plots, black indicates statistically significant directed interactions (F-tests, $\alpha = 0.05$; corrected for multiple testing). Red and blue bars denote CMN electrode contacts and “segmentation electrode” contact, respectively.

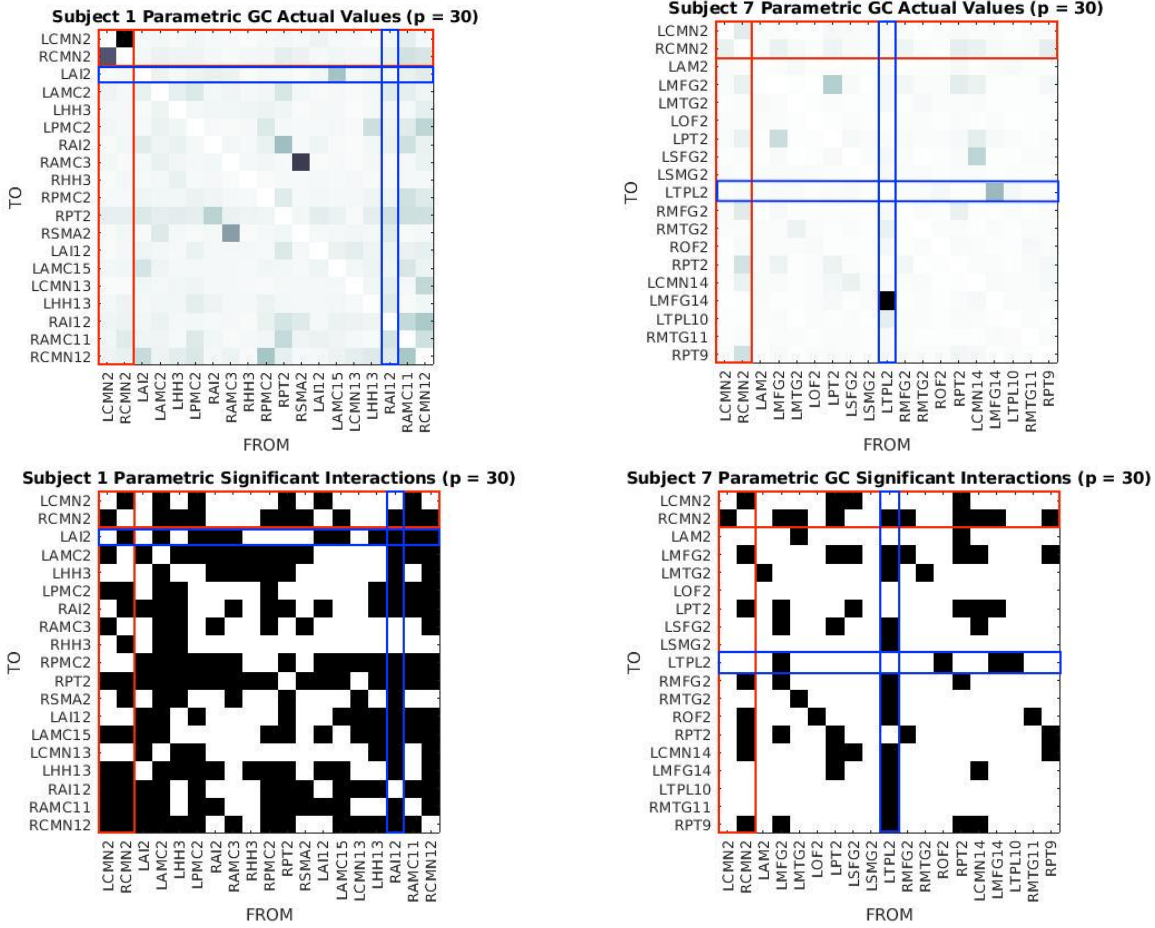


Figure 4.5: Results of parametric G-causality analysis for subject 1 (left) and subject 7 (right) using $\text{VAR}(p)$ models, order $p = 30$. The top plots show computed values of G-causality (darker means higher causality). In the bottom plots, black indicates statistically significant directed interactions (F-tests, $\alpha = 0.05$; corrected for multiple testing). Red and blue bars denote CMN electrode contacts and “segmentation electrode” contact, respectively.

combined with phase randomization of time series, is also a topic for future exploration.

Subject 1 exhibited significant directed interactions between multiple pairs of electrodes for both model orders. The interactions did not have any clear relationship between levels of cortical organization, and subcortex-cortex connectivity was frequently observed in both directions. Connections from the “segmentation electrode” (RAI12-11) to bilateral CMN contacts were observed in the VAR order-5 case, and a connection from RAI12-11 to the left CMN was observed in the VAR order-30 case. Subject 7 exhibited considerably fewer directed interactions, but still showed statistically significant connections between electrode contacts at all levels of organization. The “segmentation electrode” (LTPL2-1) was the contact that exhibited the most outgoing interactions in both VAR order-5 and VAR order-30 parametric analyses. However, it was only connected to the right CMN, bidirectionally for VAR order-5 and only an outgoing connection for VAR

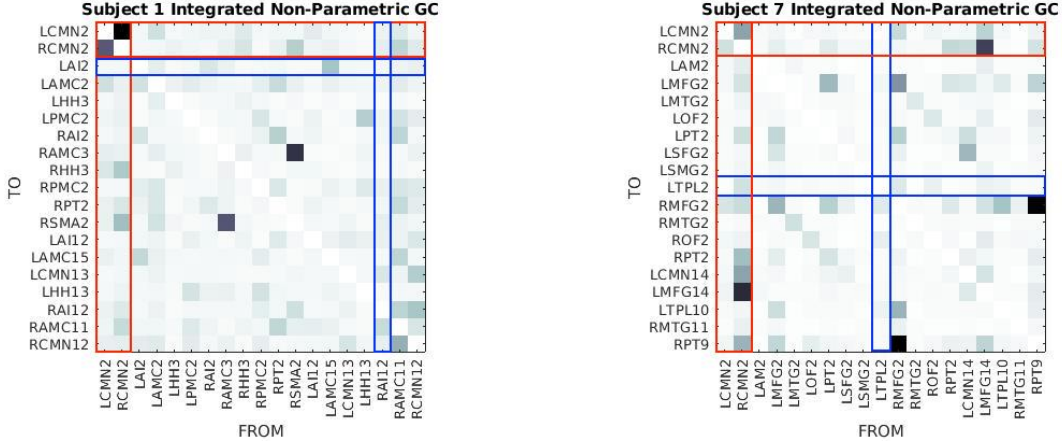


Figure 4.6: Time-domain G-causality obtained via the integration on non-parametric spectral G-causality for subject 1 (left) and subject 7 (right). Red and blue bars denote CMN electrode contacts and “segmentation electrode” contact, respectively.

order-30.

In both subjects, the two CMN contacts showed bidirectional connectivity between one another, with some of the highest absolute causality values (corresponding to lowest p-values) in subject 1, whose seizures were deemed CMN-involved previously by neurologists. Although G-causality is not a metric for “strength” of interactions, it is worth noting the relatively low p-value for inter-CMN connectivity in the CMN-involved subject. Subject 1 also exhibited more connections to and from the CMN contacts compared to subject 7 (who had CMN-uninvolved seizures). The most striking comparison between the two subjects was their overall connectivity density: subject 1 exhibited a far denser connectivity matrix than subject 7, suggesting the global density of neural connections may be a biomarker related to thalamic involvement in epilepsy, and is worth examining in future analyses.

Chapter 5

DISCUSSION

5.1 Significance

The results from chapter 4 demonstrate the applicability of my proposed analytic framework to real-world neural data. Preliminary network analysis provided supporting evidence for the hypothetical correlation between interictal and ictal (seizure) networks, although considerably more analysis is necessary to begin discussion of the hypothesis' validity. My work aims to operationalize rigorous statistical analysis of SEEG data in a way that may eventually assist clinicians in caring for epilepsy patients. Computational approaches allow neural data analysis on a never-before-seen scale: as computers become faster and datasets become larger, it is more important than ever to lay the foundations for objective, rigorous analysis of data that may be used for clinical purposes.

SEEG studies are complex, noisy, real-time recordings of up to hundreds of interacting brain regions. The utility of SEEG data in epilepsy network analysis must be carefully weighed against the complexities of the dataset as well as the invasiveness of depth electrode implantation. Currently, a large subset of pediatric epilepsy patients, including members of the Nationwide CMN cohort, suffer from multiple daily seizures that significantly impair quality of life. Their seizures may lead to intellectual disability, difficult home life, and long-term dependence on others for care. In complex epilepsy cases, treatment planning based on patient-specific seizure network derivation has the potential to revolutionize the care of patients for whom drugs, prior surgery, and other interventions have all failed.

Going back to the described shortcoming of the current clinical approach to SEEG data analysis, this framework attempts to address sample size limitations of seizure observation and include criteria for objective, repeatable statistical testing of results. Not every patient in the cohort received a treatment recommendation based on their SEEG study. One patient, who suffered no seizures during monitoring, was not treated at all, and gained no benefit from the procedure. My framework has the potential to close the gap between patients

and ensure optimal treatment recommendation for all, while expanding access to thorough analysis of SEEG data beyond highly specialized epilepsy centers. Finally, although the SEEG dataset used in this project primarily focuses on CMN involvement, this framework is general. It can be easily applied to investigate other potential targets for neuromodulation or surgery, as well as relationships between brain areas for purely scientific purposes.

5.2 Limitations

Several limitations of the framework, computational approaches, and preliminary analyses are discussed in this section.

5.2.1 Electrode Implantation

An important limitation of the preliminary analysis and the analysis of SEEG data in general is the influence of electrode implantation schemes on available information about neural networks. A known drawback of G-causal analysis is its inability to compensate for hidden network nodes. Depth electrode implantation and trajectory planning is highly patient specific, and even two SEEG implantation schemes involving the same exact electrode targets are unlikely to follow the same trajectories nor reach identical final positions. Far more common are electrode maps that differ significantly between patients. For example, subjects 1 and 7 only shared the bilateral CM nuclei as *identical* depth electrode targets, while few other electrodes overlapped somewhat. Subject 1 was implanted with 12 electrodes compared to subject 7's 14 electrodes. To benefit future analyses of SEEG data, it may be worthwhile to consider developing a common pattern of depth electrode implantation, whereby all subjects included in a common research study share at least some electrode targets to allow for their direct comparison.

5.2.2 Depth Electrode Referencing

Electrode referencing is one of the biggest concerns when it comes to working with EEG data. Referencing is necessary because EEG recordings (including SEEG) measure potential differences, not absolute values of charge or another physical quantity. In this thesis, I used a bipolar montage or “nearest-neighbor” reference for segmentation and network analysis. Since the original reference set by the SEEG recording platform was a common electrode, the resulting common signal component led to spurious significant G-causal estimates between almost all channel pairs!

Bipolar referencing is not the only approach possible for EEG referencing. Alternatives include median referencing (an electrode contact from the entire dataset is dynamically selected as the reference), expanded

“nearest-neighbor” references that take an ensemble average of more than 2 neighboring electrodes, or global averaging across all included electrodes [76]. More complex referencing approaches using machine learning or statistical formulations, such as independent component analysis, have been implemented to detect and remove influence of reference electrodes from EEG recordings [77].

5.2.3 Electrode Selection

Related to electrode implantation schemes, the most significant limitation of my preliminary analysis (aside from the small sample of only two subjects) is the somewhat arbitrary selection of electrode for both segmentation and analysis. I relied on neurologist-compiled monitoring reports to determine relevant electrodes to include in network estimation. “Segmentation electrodes” for annotation of interictal events were chosen from the LTM reports as well. However, because the subjects did not share similar implantation schemes nor had common source electrodes for comparable interictal events, the resulting electrode choices make direct comparison difficult. The chosen electrode contact for segmentation in patient 1 was a cortical-level contact along the Right Anterior Insula trajectory, while subject 7 segmentation was carried out from a sub-cortical lead in the Left Amygdala. The segmentation process, which does not shift annotated interictal events in time regardless of electrode contact, somewhat mitigates this concern. However, more rigorous approaches to electrode selection or trials of multiple electrode contacts should be implemented in the future, before definitive conclusions from the data may be reached.

5.2.4 Segmentation

For this project, I manually identified and annotated time-locations of one type of interictal epileptiform event for segmentation. I used only a small subset of the available SEEG data to find between 100 and 200 examples of 5-10Hz oscillatory events for preliminary analysis. The volume of SEEG data renders continued manual annotation impractical, and automated segmentation techniques will become even more relevant as the dataset expands to include additional patients, or future work relies on much larger datasets to inform more drastic conclusions about the nature of epileptiform activity. Approaches for automated identification involving dimensionality reduction and artificial intelligence models are being developed by the Truccolo lab and others.

5.2.5 Model Order Selection

In section 4.4, the use of AIC and BIC for model order selection in parametric G-causality analysis resulted in a relatively small ($p = 5$) model order recommendation compared to the sampling rate of the dataset. A model

order of 5 results in an AR model incorporating history effects of only 5ms or fewer. It is difficult to imagine that no deeper history effects are involved in such complex, multi-channel neural systems. Alternate criteria for model-order selection, including trial analyses of simulated data mimicking observed interictal activity, should be considered for further application of parametric G-causal analysis to high-frequency sampled SEEG recordings.

5.2.6 Sampling Rate

The small model order and high sample:time ratio of the segmented epileptiform events causes further problems with parametric estimation. The parametric approach to G-causal analysis uses the $\text{VAR}(p)$ coefficient matrix to estimate the spectral matrix of the VAR process (see chapter 3 for a detailed treatment of spectral estimation from AR coefficients). The high sampling rate of the SEEG signal may lead to very high VAR model orders and corresponding large number of parameters, making estimation difficult given current sample sizes. As a result, time and spectral domain causality might both be significantly affected. Although not-ideal, lowpass filtering followed by downsampling of the SEEG data may be required for proper analysis using parametric G-causality. The spline $\text{VAR}(p)$ approach (section 3.5.3) is an alternative in this sense, but it brings its own drawbacks due bias and variance issues originating from the fitting of many multiple reduced models.

5.2.7 Statistical Analysis

The parametric approach to G-causal analysis allows straightforward significance testing, as the sampling distribution for time-domain causality is known. The Fisher and (when appropriate) χ^2 distributions, along with a false discovery rate correction for multiple testing, readily allow generation of connectivity matrices that discriminate statistically insignificant directed interactions.

As discussed previously, spectral domain G-causality has no known sampling distribution. Results from the non-parametric approach and spectral-domain results from the parametric approach must be tested for significance using resampling methods or alternative means of cross-validation. However, resampling is not straightforward in the context of epileptiform events as segmented here. The purpose of resampling analysis is to construct a distribution under the null hypothesis that no significant directed interactions occur within the data. An intuitive way of generating such a distribution (for the non-parametric approach) is to randomly permute trial and channel labels in a dataset of segmented interictal epileptiform events. The goal of this random permutation is to nullify the channel-channel interactions while preserving other variables of the dataset. However, since not all channels may manifest identical neural activity during an epileptiform event,

the intuitive resampling approach may further affect the dataset. For example, if recording channels possesses distinct power spectra, then shuffling segments independently of channel label may flatten or otherwise mutate the power spectrum.

Additionally, induced phase-locking by the segmentation of oscillatory interictal events may result in false correlations in resampled null distributions where trial numbers are permuted. In other words, if the class of epileptiform event involves frequency-specific oscillatory activity, the annotation process may artificially lead to phase correlation between unrelated trials.

Members of the Truccolo lab, including myself, are currently working on alternative solutions for random resampling approaches for statistical testing specific to this project. As stated earlier, trial shuffling (while preserving channel label) combined with phase randomization of individual segmented time series is a promising alternative approach.

Finally, a systematic analysis of the potential complementarity of the three different approaches for conditional GC, namely parametric $\text{VAR}(p)$, spline $\text{VAR}(p)$, and non-parametric approach based on spectral matrix factorization, is warranted.

5.3 Continuation

I plan to continue working on this project, with the goal of refining the proposed analytic framework and performing analysis on a greater sample size of patients to draw conclusions about the role of the CMN in their interictal and ictal networks.

Future work should focus on addressing the current limitations of the approach, including those discussed in the previous section. For example, I have already begun investigating potential methods for generation of a null-hypothesis distribution for non-parametric G-causality analyses. However, another important consideration of work related to this project is the relative recency of SEEG data collection. The last subject was implanted with depth electrodes and monitored just last year. Long term outcomes data based on neurologist and neurosurgeon treatment recommendation is necessary to understand the connection between treatment success, the CMN, and observed seizure and interictal dynamics.

A critical part of any statistical analysis is sample size. As more patients at Nationwide Children's Hospital and other epilepsy centers undergo SEEG monitoring, more conclusive analyses will become possible, and may eventually even result in clinical trials using objective frameworks similar to the one described in this thesis for treatment recommendation, bridging the gap from basic research to translational applications.

BIBLIOGRAPHY

- [1] K. M. Aaberg, N. Gunnes, I. J. Bakken, C. Lund Søraas, A. Berntsen, P. Magnus, M. I. Lossius, C. Stoltenberg, R. Chin, and P. Surén, “Incidence and Prevalence of Childhood Epilepsy: A Nationwide Cohort Study,” *Pediatrics*, vol. 139, no. 5, 05 2017, e20163908. [Online]. Available: <https://doi.org/10.1542/peds.2016-3908>
- [2] M. Zack and R. Kobau, “National and state estimates of the numbers of adults and children with active epilepsy — united states, 2015,” *Morb Mortal Wkly Re*, vol. 66, pp. 821–825, 2017. [Online]. Available: <http://dx.doi.org/10.15585/mmwr.mm6631a1>
- [3] G. L. Holmes and Y. Ben-Ari, “The neurobiology and consequences of epilepsy in the developing brain,” *Pediatric research*, vol. 49, no. 3, pp. 320–325, 2001.
- [4] P. Kwan, A. Arzimanoglou, A. T. Berg, M. J. Brodie, W. Allen Hauser, G. Mathern, S. L. Moshé, E. Perucca, S. Wiebe, and J. French, “Definition of drug resistant epilepsy: consensus proposal by the ad hoc task force of the ilae commission on therapeutic strategies,” *Epilepsia*, 2010. [Online]. Available: <https://doi.org/10.1111/j.1528-1167.2009.02397.x>
- [5] K. M. Aaberg, N. Gunnes, I. J. Bakken, C. Lund Søraas, A. Berntsen, P. Magnus, M. I. Lossius, C. Stoltenberg, R. Chin, and P. Surén, “Incidence and Prevalence of Childhood Epilepsy: A Nationwide Cohort Study,” *Pediatrics*, vol. 139, no. 5, 05 2017, e20163908. [Online]. Available: <https://doi.org/10.1542/peds.2016-3908>
- [6] R. Dwivedi, B. Ramanujam, P. S. Chandra, S. Sapra, S. Gulati, M. Kalaivani, A. Garg, C. S. Bal, M. Tripathi, S. N. Dwivedi *et al.*, “Surgery for drug-resistant epilepsy in children,” *New England Journal of Medicine*, vol. 377, no. 17, pp. 1639–1647, 2017.
- [7] N. D. Sisterson and V. Kokkinos, “Neuromodulation of epilepsy networks,” *Neurosurgery Clinics*, vol. 31, no. 3, pp. 459–470, 2020.

- [8] H. Yan, E. Toyota, M. Anderson, T. J. Abel, E. Donner, S. K. Kalia, J. Drake, J. T. Rutka, and G. M. Ibrahim, “A systematic review of deep brain stimulation for the treatment of drug-resistant epilepsy in childhood,” *Journal of Neurosurgery: Pediatrics*, vol. 23, no. 3, pp. 274–284, 2018.
- [9] T. L. Skarpaas, B. Jarosiewicz, and M. J. Morrell, “Brain-responsive neurostimulation for epilepsy (rns® system),” *Epilepsy Research*, vol. 153, pp. 68–70, 2019. [Online]. Available: <https://www.sciencedirect.com/science/article/pii/S0920121118305758>
- [10] S. Wong, R. Mani, and S. Danish, “Comparison and selection of current implantable anti-epileptic devices,” *Neurotherapeutics*, vol. 16, no. 2, pp. 369–380, 2019.
- [11] S. C. Schachter and C. B. Saper, “Vagus nerve stimulation,” *Epilepsia*, vol. 39, no. 7, pp. 677–686, 1998.
- [12] T. R. Henry, “Therapeutic mechanisms of vagus nerve stimulation,” *Neurology*, vol. 59, no. 6 suppl 4, pp. S3–S14, 2002.
- [13] B. Fisher, J. A. DesMarteau, E. H. Koontz, S. J. Wilks, and S. E. Melamed, “Responsive vagus nerve stimulation for drug resistant epilepsy: a review of new features and practical guidance for advanced practice providers,” *Frontiers in neurology*, p. 1863, 2021.
- [14] C. E. Stafstrom and L. Carmant, “Seizures and epilepsy: an overview for neuroscientists,” *Cold Spring Harbor perspectives in medicine*, vol. 5, no. 6, p. a022426, 2015.
- [15] E. Beghi, “The epidemiology of epilepsy,” *Neuroepidemiology*, vol. 54, no. 2, pp. 185–191, 2020.
- [16] R. M. Richardson, “Decision making in epilepsy surgery,” *Neurosurgery Clinics*, vol. 31, no. 3, pp. 471–479, 2020.
- [17] M. A. Kramer and S. S. Cash, “Epilepsy as a disorder of cortical network organization,” *The Neuroscientist*, vol. 18, no. 4, pp. 360–372, 2012.
- [18] V. Krishna, F. Sammartino, N. K. K. King, R. Q. Y. So, and R. Wennberg, “Neuromodulation for epilepsy,” *Neurosurgery Clinics*, vol. 27, no. 1, pp. 123–131, 2016.
- [19] C. N. Heck, D. King-Stephens, A. D. Massey, D. R. Nair, B. C. Jobst, G. L. Barkley, V. Salanova, A. J. Cole, M. C. Smith, R. P. Gwinn *et al.*, “Two-year seizure reduction in adults with medically intractable partial onset epilepsy treated with responsive neurostimulation: Final results of the rns system pivotal trial,” *Epilepsia*, vol. 55, no. 3, pp. 432–441, 2014.
- [20] A. Ilyas, D. Pizarro, A. K. Romeo, K. O. Riley, and S. Pati, “The centromedian nucleus: Anatomy, physiology, and clinical implications,” *Journal of Clinical Neuroscience*, vol. 63, pp. 1–7, 2019.

- [21] L. Yu and H. Blumenfeld, “Theories of impaired consciousness in epilepsy,” *Annals of the New York Academy of Sciences*, vol. 1157, no. 1, pp. 48–60, 2009.
- [22] S. S. Spencer, “The relative contributions of mri, spect, and pet imaging in epilepsy,” *Epilepsia*, vol. 35, pp. S72–S89, 1994.
- [23] F. Velasco, P. E. Saucedo-Alvarado, A. Reichrath, H. Valdés-Quiroz, G. Aguado-Carrillo, and A. L. Velasco, “Centromedian nucleus and epilepsy,” *Journal of Clinical Neurophysiology*, vol. 38, no. 6, pp. 485–493, 2021.
- [24] H. J. Jo, D. L. Kenny-Jung, I. Balzekas, E. E. Benarroch, D. T. Jones, B. H. Brinkmann, S. M. Stead, J. J. Van Gompel, K. M. Welker, and G. A. Worrell, “Nuclei-specific thalamic connectivity predicts seizure frequency in drug-resistant medial temporal lobe epilepsy,” *NeuroImage: Clinical*, vol. 21, p. 101671, 2019.
- [25] M. Velasco, F. Velasco, H. Alcalá, G. Dávila, and A. E. Díaz-de León, “Epileptiform eeg activity of the centromedian thalamic nuclei in children with intractable generalized seizures of the lennox-gastaut syndrome,” *Epilepsia*, vol. 32, no. 3, pp. 310–321, 1991.
- [26] L. J. Dalic, A. E. Warren, J. C. Young, W. Thevathasan, A. Roten, K. J. Bulluss, and J. S. Archer, “Cortex leads the thalamic centromedian nucleus in generalized epileptic discharges in lennox-gastaut syndrome,” *Epilepsia*, vol. 61, no. 10, pp. 2214–2223, 2020.
- [27] V. Chiosa, S. A. Groppa, D. Ciolac, N. Koirala, L. Mišina, Y. Winter, M. Moldovanu, M. Muthuraman, and S. Groppa, “Breakdown of thalamo-cortical connectivity precedes spike generation in focal epilepsies,” *Brain connectivity*, vol. 7, no. 5, pp. 309–320, 2017.
- [28] F. Pizzo, N. Roehri, B. Giusiano, S. Lagarde, R. Carron, D. Scavarda, A. McGonigal, C. Filipescu, I. Lambert, F. Bonini, A. Trebuchon, C.-G. Bénar, and F. Bartolomei, “The ictal signature of thalamus and basal ganglia in focal epilepsy,” *Neurology*, vol. 96, no. 2, pp. e280–e293, 2021. [Online]. Available: <https://n.neurology.org/content/96/2/e280>
- [29] J. P. Szaflarski, “Thalamus and seizures—here we come again . . . ,” *Epilepsy Currents*, vol. 21, no. 3, pp. 154–156, 2021.
- [30] M. Velasco, F. Velasco, A. L. Velasco, M. Luján, and J. V. del Mercado, “Epileptiform eeg activities of the centromedian thalamic nuclei in patients with intractable partial motor, complex partial, and generalized seizures,” *Epilepsia*, vol. 30, no. 3, pp. 295–306, 1989.

- [31] W. P. Welch, J. L. Hect, and T. J. Abel, “Case report: responsive neurostimulation of the centromedian thalamic nucleus for the detection and treatment of seizures in pediatric primary generalized epilepsy,” *Frontiers in neurology*, vol. 12, p. 554, 2021.
- [32] J. L. Alcala-Zermenio, N. M. Gregg, E. C. Wirrell, M. Stead, G. A. Worrell, J. J. Van Gompel, and B. N. Lundstrom, “Centromedian thalamic nucleus with or without anterior thalamic nucleus deep brain stimulation for epilepsy in children and adults: A retrospective case series,” *Seizure*, vol. 84, pp. 101–107, 2021.
- [33] D. E. Burdette, M. A. Haykal, B. Jarosiewicz, R. R. Fabris, G. Heredia, K. Elisevich, and S. E. Patra, “Brain-responsive corticothalamic stimulation in the centromedian nucleus for the treatment of regional neocortical epilepsy,” *Epilepsy & Behavior*, vol. 112, p. 107354, 2020.
- [34] B. C. Jobst, F. Bartolomei, B. Diehl, B. Frauscher, P. Kahane, L. Minotti, A. Sharan, N. Tardy, G. Worrell, and J. Gotman, “Intracranial eeg in the 21st century,” *Epilepsy currents*, vol. 20, no. 4, pp. 180–188, 2020.
- [35] J. P. Andrews, A. Gummadavelli, P. Farooque, J. Bonito, C. Arencibia, H. Blumenfeld, and D. D. Spencer, “Association of Seizure Spread With Surgical Failure in Epilepsy,” *JAMA Neurology*, vol. 76, no. 4, pp. 462–469, 04 2019. [Online]. Available: <https://doi.org/10.1001/jamaneurol.2018.4316>
- [36] K. J. Staley and F. E. Dudek, “Interictal spikes and epileptogenesis,” *Epilepsy Currents*, vol. 6, no. 6, pp. 199–202, 2006, pMID: 17260059. [Online]. Available: <https://doi.org/10.1111/j.1535-7511.2006.00145.x>
- [37] N. Kane, J. Acharya, S. Beniczky, L. Caboclo, S. Finnigan, P. W. Kaplan, H. Shibasaki, R. Pressler, and M. J. van Putten, “A revised glossary of terms most commonly used by clinical electroencephalographers and updated proposal for the report format of the eeg findings. revision 2017,” *Clinical neurophysiology practice*, vol. 2, p. 170, 2017.
- [38] E. H. Smith, J.-y. Liou, E. M. Merricks, T. Davis, K. Thomson, B. Greger, P. House, R. G. Emerson, R. Goodman, G. M. McKhann *et al.*, “Human interictal epileptiform discharges are bidirectional traveling waves echoing ictal discharges,” *Elife*, vol. 11, p. e73541, 2022.
- [39] R. Coben and I. Mohammad-Rezazadeh, “Neural connectivity in epilepsy as measured by granger causality,” *Frontiers in human neuroscience*, vol. 9, p. 194, 2015.
- [40] C. M. Epstein, B. M. Adhikari, R. Gross, J. Willie, and M. Dhamala, “Application of high-frequency granger causality to analysis of epileptic seizures and surgical decision making,” *Epilepsia*, vol. 55, no. 12, pp. 2038–2047, 2014.

- [41] G. Buzsáki and A. Draguhn, “Neuronal oscillations in cortical networks,” *Science*, vol. 304, no. 5679, pp. 1926–1929, 2004. [Online]. Available: <https://www.science.org/doi/abs/10.1126/science.1099745>
- [42] J. Rapela, T. Proix, D. Todorov, and W. Truccolo, “Uncovering low-dimensional structure in high-dimensional representations of long-term recordings in people with epilepsy,” in *2019 41st Annual International Conference of the IEEE Engineering in Medicine and Biology Society (EMBC)*. IEEE, 2019, pp. 2246–2251.
- [43] A. Bruns, “Fourier-, hilbert-and wavelet-based signal analysis: are they really different approaches?” *Journal of neuroscience methods*, vol. 137, no. 2, pp. 321–332, 2004.
- [44] A. Grossmann and J. Morlet, “Decomposition of hardy functions into square integrable wavelets of constant shape,” *SIAM journal on mathematical analysis*, vol. 15, no. 4, pp. 723–736, 1984.
- [45] V. V. Moca, H. Bárzan, A. Nagy-Dăbâcan, and R. C. Mureşan, “Time-frequency super-resolution with superlets,” *Nature communications*, vol. 12, no. 1, pp. 1–18, 2021.
- [46] A. A. Faisal, L. P. Selen, and D. M. Wolpert, “Noise in the nervous system,” *Nature reviews neuroscience*, vol. 9, no. 4, pp. 292–303, 2008.
- [47] B. Øksendal, “Stochastic differential equations,” in *Stochastic differential equations*. Springer, 2003, pp. 65–84.
- [48] D. B. Percival, A. T. Walden *et al.*, *Spectral analysis for physical applications*. cambridge university press, 1993.
- [49] M. Kamiński, M. Ding, W. Truccolo, and S. Bressler, “Evaluating causal relations in neural systems: granger causality, directed transfer function and statistical assessment of significance.” *Biological Cybernetics*, vol. 85, no. 2, pp. 145–157, aug 2001.
- [50] L. Barnett and A. K. Seth, “The mvgc multivariate granger causality toolbox: a new approach to granger-causal inference,” *Journal of neuroscience methods*, vol. 223, pp. 50–68, 2014.
- [51] P. Babaeighazvini, L. M. Rueda-Delgado, J. Gooijers, S. P. Swinnen, and A. Daffertshofer, “Brain structural and functional connectivity: A review of combined works of diffusion magnetic resonance imaging and electro-encephalography,” *Frontiers in human neuroscience*, p. 585, 2021.
- [52] K. J. Friston, “Functional and effective connectivity: a review,” *Brain connectivity*, vol. 1, no. 1, pp. 13–36, 2011.

- [53] W. Stacey, M. Kramer, K. Gunnarsdottir, J. Gonzalez-Martinez, K. Zaghloul, S. Inati, S. Sarma, J. Stiso, A. N. Khambhati, D. S. Bassett *et al.*, “Emerging roles of network analysis for epilepsy,” *Epilepsy research*, vol. 159, p. 106255, 2020.
- [54] A. M. Bastos and J.-M. Schoffelen, “A tutorial review of functional connectivity analysis methods and their interpretational pitfalls,” *Frontiers in systems neuroscience*, vol. 9, p. 175, 2016.
- [55] C. W. Granger, “Investigating causal relations by econometric models and cross-spectral methods,” *Econometrica: journal of the Econometric Society*, pp. 424–438, 1969.
- [56] J. Geweke, “Measurement of linear dependence and feedback between multiple time series,” *Journal of the American statistical association*, vol. 77, no. 378, pp. 304–313, 1982.
- [57] J. F. Geweke, “Measures of conditional linear dependence and feedback between time series,” *Journal of the American Statistical Association*, vol. 79, no. 388, pp. 907–915, 1984.
- [58] A. Brovelli, M. Ding, A. Ledberg, Y. Chen, R. Nakamura, and S. L. Bressler, “Beta oscillations in a large-scale sensorimotor cortical network: directional influences revealed by granger causality,” *Proceedings of the National Academy of Sciences*, vol. 101, no. 26, pp. 9849–9854, 2004.
- [59] Y. Chen, S. L. Bressler, and M. Ding, “Frequency decomposition of conditional granger causality and application to multivariate neural field potential data,” *Journal of neuroscience methods*, vol. 150, no. 2, pp. 228–237, 2006.
- [60] T. Proix, V. K. Jirsa, F. Bartolomei, M. Guye, and W. Truccolo, “Predicting the spatiotemporal diversity of seizure propagation and termination in human focal epilepsy,” *Nature communications*, vol. 9, no. 1, pp. 1–15, 2018.
- [61] R. Zelmann, A. C. Paulk, I. Basu, A. Sarma, A. Yousefi, B. Crocker, E. Eskandar, Z. Williams, G. R. Cosgrove, D. S. Weisholtz *et al.*, “Closes: A platform for closed-loop intracranial stimulation in humans,” *NeuroImage*, vol. 223, p. 117314, 2020.
- [62] Y. Benjamini and Y. Hochberg, “Controlling the false discovery rate: a practical and powerful approach to multiple testing,” *Journal of the Royal statistical society: series B (Methodological)*, vol. 57, no. 1, pp. 289–300, 1995.
- [63] P. A. Stokes and P. L. Purdon, “A study of problems encountered in granger causality analysis from a neuroscience perspective,” *Proceedings of the National Academy of Sciences*, vol. 114, no. 34, pp. E7063–E7072, 2017.

- [64] L. Barnett, A. B. Barrett, and A. K. Seth, “Solved problems for granger causality in neuroscience: A response to stokes and purdon,” *NeuroImage*, vol. 178, pp. 744–748, 2018.
- [65] M. Dhamala, G. Rangarajan, and M. Ding, “Estimating granger causality from fourier and wavelet transforms of time series data,” *Physical review letters*, vol. 100, no. 1, p. 018701, 2008.
- [66] E. Spencer, L.-E. Martinet, E. Eskandar, C. Chu, E. Kolaczyk, S. Cash, U. Eden, and M. Kramer, “A procedure to increase the power of granger-causal analysis through temporal smoothing,” *Journal of neuroscience methods*, vol. 308, pp. 48–61, 2018.
- [67] X. Wen, G. Rangarajan, and M. Ding, “Multivariate granger causality: an estimation framework based on factorization of the spectral density matrix,” *Philosophical Transactions of the Royal Society A: Mathematical, Physical and Engineering Sciences*, vol. 371, no. 1997, p. 20110610, 2013.
- [68] M. Dhamala, H. Liang, S. L. Bressler, and M. Ding, “granger-geweke causality: Estimation and interpretation,” *NeuroImage*, vol. 175, pp. 460–463, 2018.
- [69] G. T. Wilson, “The factorization of matricial spectral densities,” *SIAM Journal on Applied Mathematics*, vol. 23, no. 4, pp. 420–426, 1972.
- [70] C. E. Shannon, “Communication in the presence of noise,” *Proceedings of the IRE*, vol. 37, no. 1, pp. 10–21, 1949.
- [71] M. F. Pagnotta, M. Dhamala, and G. Plomp, “Benchmarking nonparametric granger causality: Robustness against downsampling and influence of spectral decomposition parameters,” *NeuroImage*, vol. 183, pp. 478–494, 2018.
- [72] C. X. Lim, M. G. Ricos, L. M. Dibbens, and S. E. Heron, “Kcnt1 mutations in seizure disorders: the phenotypic spectrum and functional effects,” *Journal of medical genetics*, vol. 53, no. 4, pp. 217–225, 2016.
- [73] R. MacKinnon, “Potassium channels,” *FEBS letters*, vol. 555, no. 1, pp. 62–65, 2003.
- [74] T. Gertler, D. Bearden, A. Bhattacharjee, and G. Carvill, *KCNT1-related epilepsy*. University of Washington, 2018.
- [75] MATLAB, *version 9.9.0 (R2020b)*. Natick, Massachusetts: The MathWorks Inc., 2020.
- [76] W. A. Ríos-Herrera, P. V. Olguín-Rodríguez, J. D. Arzate-Mena, M. Corsi-Cabrera, J. Escalona, A. Marín-García, J. Ramos-Loyo, A. L. Rivera, D. Rivera-López, J. F. Zapata-Berruecos *et al.*, “The influence of

eeg references on the analysis of spatio-temporal interrelation patterns,” *Frontiers in neuroscience*, p. 941, 2019.

- [77] S. Hu, M. Stead, and G. A. Worrell, “Automatic identification and removal of scalp reference signal for intracranial eegs based on independent component analysis,” *IEEE Transactions on Biomedical Engineering*, vol. 54, no. 9, pp. 1560–1572, 2007.